Numerical simulations of convection and gravity currents near the temperature of maximum density

by

Andrew Grace

A thesis
presented to the University of Waterloo
in fulfillment of the
thesis requirement for the degree of
Doctor of Philosophy
in
Applied Mathematics (Water)

Waterloo, Ontario, Canada, 2022

Examining Committee Membership

The following served on the Examining Committee for this thesis. The decision of the Examining Committee is by majority vote.

External Examiner:
Bertram Boehrer
Senior Scientist and Work Group Leader,
Limnophysics and Lake Modelling
Helmholtz Centre for Environmental Research - UFZ

Supervisor(s):
Marek Stastna
Professor,
Department of Applied Mathematics,
University of Waterloo

Kevin G. Lamb
Professor,
Department of Applied Mathematics,
University of Waterloo

K. Andrea Scott
Associate Professor,
Department of Systems Design Engineering,
University of Waterloo

Internal Member:
Mike Waite
Associate Professor,
Department of Applied Mathematics,
University of Waterloo

Internal Member:	Christopher Fletcher Associate Professor, Department of Geography and Environmental Management, University of Waterloo
Internal-External Member:	Jean-Pierre Hickey Associate Professor, Department of Engineering, University of Waterloo

Author's Declaration

I hereby declare that I am the sole author of this thesis. This is a true copy of the thesis, including any required final revisions, as accepted by my examiners.

I understand that my thesis may be made electronically available to the public.

Abstract

Recently, the dynamics of flows in cold freshwater (temperatures around the temperature of maximum density, 3.98 °C) has garnered much interest in the environmental fluid dynamics community. From a dynamical perspective, fluid flow in cold freshwater is interesting due to the non-linear relationship between temperature and density, as well as the relatively slow current speeds. In this thesis, we have presented a series of numerical process studies with the goal of capturing, understanding, and describing characteristic dynamics of different temperature intervals of the freshwater non-linear equation of state (NLEOS), quantified by a parameter called the NLEOS parameter Θ. We use two canonical examples of density driven phenomena to describe the dynamics of cold water; convection and gravity currents. This thesis begins by providing some general background and context on studies in cold freshwater, and provide some discussion on some technical background and the numerical model.

An important interval of the NLEOS is the region between the freshwater freezing point and the temperature maximum density. Over this interval, adding heat to the system increases the water density. In chapter 3, we present a series of numerical process studies of a freshwater system where a volumetric heating source (representing incident solar radiation) preferentially adds heat near the surface of a body of cold freshwater in the presence of a stable background shear current. The heating source induces small and nearly linear temperature and density changes within the flow, leading to an unstable density profile, resulting in convective plumes. The results of this chapter show that for a sufficiently strong shear current, the growth phase of the thermally induced instabilities is nearly two dimensional and that the transition to more vigorous three dimensional motion is initialized by baroclinic production of vorticity by convective instabilities followed by a rapid increase in streamwise vorticity generated by vortex tilting and stretching. We describe how this process is modified by differences in shear strength and thermal forcing attenuation length.

In chapter 4, we present a series of simulations of gravity currents designed to isolate the effects of a monotonically increasing but non-linear interval of the NLEOS. In this chapter, we compare the evolution of gravity currents that are lighter than the ambient to those that are heavier than the ambient (while holding the magnitude of the density and temperature differences equal across all cases). The results of this chapter show that for intrusions initially cooler than the ambient, the density difference between the intrusion and the ambient decreases rapidly, while for intrusions initially warmer than the ambient, the density difference decreases at a slower rate. The differing rates at which the density difference decreases lead to asymmetries in head location, and vertical extent of intruding

fluid, and may have implications for larger scale flows in this temperature regime. These results are robust across Grashof numbers studied.

In chapter 5 we present a series of simulations of gravity currents where ambient and intruding temperatures are on opposite sides of the temperature of maximum density. We use these simulations to describe how cabbeling (mixing of parcels of fluid that lead to a parcel of fluid that is denser) affects the evolution of gravity currents. We show that initially buoyant currents undergo mixing in the body and tail region of the gravity current, which generates dense water from cabbeling. The dense water sinks and forms a secondary current along the bottom of the domain that is much larger in scale than the original buoyant current. In this chapter, we show that the maximum distance that the initial current progresses is a non-linear function of Θ and the depth of the domain. Lastly, we discuss some general characteristics of the emergent current that forms along the bottom. We highlight that once the bottom current forms, larger values of Θ lead to a larger spatial extent of the current but narrower distributions of density and temperature about their mean values.

Finally, chapter 6 provides a brief summary and a look towards potential future work related to the contents of this thesis.

Acknowledgements

These years have flown by, and there are so many people I would like to acknowledge. Firstly, I would like to thank my parents for so many things. In fact, so many that listing them all would probably extend the length of this thesis by a few more pages, so I will instead thank them for one specific thing. Thanks for never making me feel wrong for a decision I was making for myself. That has allowed me to forge my own path and become the best person I can be.

I would like to thank my supervisors; Marek Stastna, Kevin Lamb, and Andrea Scott. Without you and your guidance, this thesis would be very different (and probably worse is every way). I have become a much better scientist and researcher because of your efforts.

I would also like to give a huge thanks to my committee: Mike Waite, Chris Fletcher, Jean-Pierre Hickey and my external examiner Bertram Boehrer. Thank you for spending the time to read my work and give invaluable feedback.

I would like to thank all the grad students I have overlapped with throughout the years. A special shout-out goes to Justin Shaw, Donovan Allum, David Deepwell, Ben Storer and Will Xu. Your friendship and informal guidance really helped shape the kind of grad student I became. I want to thank all the friends I have made along the way. I want to specifically mention Andrew Cameron, Bryce Hosking, Matt Slavin, Matt Angus, Bradley Noonan, Jon Horrocks, and Carl Tutton. Being able to interact with you guys and to allow me to be a part of your life made this whole journey both memorable and a lot easier.

Most of all, I want to thank by wife-to-be Jenn Gilmour. These last few years would have been nearly impossible without you. You always were my cheerleader, and you were excited every time I hit a milestone or one of my goals, and that really helped. I love you so much.

Dedication

This thesis is dedicated to those who strive to be better today than they were yesterday.

Table of Contents

List of Tables

List of Figures

List of Symbols

x, y, z	Spatial coordinates
N_x, N_y, N_z	Number of grid points in the x, y, and z directions respectively
Δx, Δy, Δz	Grid spacing in the x, y, and z directions respectively
$\tilde{k}$, $\tilde{l}$	Wave numbers in the x, and y directions respectively
$\hat{\boldsymbol{i}}$, $\hat{\boldsymbol{j}}$, $\hat{\boldsymbol{k}}$	Unit vectors in the x, y, and z directions respectively
$\boldsymbol{u}$	Velocity vector with components (u, v, w)
$\boldsymbol{\omega}$	Vorticity vector with components $(\omega_x, \omega_y, \omega_z)$
p	Dynamic pressure
p'	Perturbation pressure
p^H, p_v	Hydrostatic pressure
P_0	Reference Pressure
K	Isothermal compressibility
t	Time
$\mathcal{T}$, τ, t_b	Time scales
T	Temperature
$\tilde{T}_p$	Perturbation temperature
θ, ΔT, ΔT_1, ΔT_2	Temperature scales
$\bar{T}$	Domain averaged temperature
T_{md}	Temperature of maximum density
T_0, T_1, T_2, T_3, T^{inf}	Reference temperatures
T_c	Critical temperature
T_a, T_i	Ambient and intruding temperatures
S	Salinity
e_{ij}	Rate of strain tensor
τ_{ij}, $\boldsymbol{\tau}$	Stress tensor in index notation and vector notation
δ_{ij}	Kronecker Delta
ϵ_{ijk}	Permutation tensor

$\boldsymbol{q}$, $\boldsymbol{q}_{in}$, $\boldsymbol{q}_{ext}$	Total, internal, and external heat heat fluxes
ε	Kinetic energy dissipation rate
ϵ	Non-dimensional temperature of maximum density
ρ	Full density
ρ'	Perturbation density
ρ_{nl}, ρ_q, ρ_c	Equations of state in (1.4), (1.5), (1.6) respectively.
ρ_0, ρ_1, ρ_2	Reference densities
ρ_{md}	Maximum density
$\Delta\rho$	Characteristic density difference
g	Acceleration due to gravity
C_p	Heat capacity at constant pressure
μ, λ	Dynamic and bulk viscosities
k	Thermal conductivity
ν, κ	Kinematic viscosity and thermal diffusivity
e	Internal energy per unit mass
C	Proportionality constant for (1.5), (3.5), and (5.1)
c_0, c_1, c_2, c_3	Parameters for the non-linear equation of state from Brydon et al. (1999).
L	Dimensional domain length
H	Dimensional domain depth
l	Dimensionless domain length
h	Dimensionless domain depth
$U(z)$	Background current velocity profile
U_0	Maximum background current velocity
$\tilde{U}_z$	Local shear
$\mathcal{U}$, $\mathscr{U}$, U_b	Characteristic velocity scales
c	The speed of sound in water
v_C, v_B, v_T	Gravity current head speeds
δ, δ_x, δ_z	Transition widths
ℓ	Attenuation length of solar radiation
Q_0	Intensity of solar radiation
$\tilde{\sigma}_i$	Complex instability growth rate
μ_1, μ_2, μ_3	Non-dimensional length scales
S_i, B_i	Magnitudes of components of vortex tilting/stretching and buoyant production
h_s, h_l	Upper and lower layer depths
$\Delta\rho_f$, ΔT_f	Emergent density and temperature differences
χ	Indicator function
A,γ	Dimensionless constants

z_0	Initial height of intrusion
$\mathcal{B}(z)$, β	Function and parameter
α	Thermal expansion coefficient (at constant pressure)
ke	Domain averaged kinetic energy
$\mathcal{L}$	Maximum extent of hypopycnal current
x_ℓ	Gravity current lock length
A, $\mathcal{A}$	Computed area of current and theoretical area of current
R_1, R_2, R_3	Dimensionless coefficients for non-linear equation of state in (4.4)
Θ, Θ_1, Θ_2	Non-linear equation of state parameters
Re	Non-dimensional parameter: Reynolds number
Gr	Non-dimensional parameter: Grashof number
Pr	Non-dimensional parameter: Prandtl number
Ri	Non-dimensional parameter: Richardson number
At	Non-dimensional parameter: Atwood number
Ri_b	Non-dimensional parameter: Bulk Richardson number

Chapter 1

Introduction

1.1 Background

Environmental and geophysical fluid dynamics (EGFD) is the study of fluid dynamic processes relevant to rivers, oceans, the atmosphere, and lakes. The study of each is typically driven by different practical interests. For rivers, it might be understanding where erosion occurs and how to mitigate it. For oceans it might be understanding large scale circulation patterns and deep water renewal. For the atmosphere, one might be interested in understanding the interactions with different canopy types (forest mosaics versus urban centres for example). The work presented in this thesis focuses on idealized physical processes most relevant to the last item in this list: lakes. Lakes are an interesting and unique class of geophysical body due to the strong variations in their characteristics. Variations in parameters such as depth, bathymetry, concentration of organic and inorganic compounds, surface area, and stratification all indicate that they are relatively complicated bodies to study. There have been a variety of scientific reviews over the years that focus on lakes from different perspectives. Imberger and Hamblin (1982) provides a comprehensive list of scaling laws for a variety of processes such as responses to external forcing, surface mixed layer processes, and interior mixing. Wüest and Lorke (2003) provides an updated review of surface boundary layer processes (surface gravity waves, and turbulent mixing due to momentum and heat fluxes at the surface), stratified interior processes (basin scale seiches, internal waves, and interior mixing), and bottom boundary fluxes (bottom boundary layer structure, and bottom turbulence). Boehrer and Schultze (2008) provides a comprehensive overview of stratifying processes in lacustrine bodies of water. Bouffard and Wüest (2019) provides a modern review and discussion specifically on convective processes that occur

in lakes from buoyancy forcing, bioconvection, or penetration by solar radiation. These resources above are clearly not exhaustive but indicate that interest in lakes has been long standing and consequently there is a large library of literature.

It has not been until recently that the role of wintertime fluid dynamics in ice covered lakes has gained more prominence in the limnological literature. For example, of the reviews listed above, only Boehrer and Schultze (2008) and Bouffard and Wüest (2019) mention anything regarding wintertime dynamics. From a dynamic perspective, the winter is an incredibly interesting time. Perhaps the most obvious difference between the summer and the winter is the presence of surface ice. The review article written by Kirillin et al. (2012) highlights the key differences that separate winter fluid physics from that in open water seasons. In their article, they remark that physical processes of seasonally ice-covered lakes can be divided into three connected categories; 1) processes related to the timing and duration of ice cover (called ice phenology); 2) ice mechanics, structure, optical properties and heat transfer (called ice physics); and 3) internal thermodynamics and hydrodynamics of ice covered bodies of water. In short, a combination of ice and snow cover creates a physical cap on the lake that limits heat and momentum fluxes from the atmosphere. Beneath the ice, a weakly stratified environment forms in the early winter, and this leads to different dominant physical processes beneath the ice like seiching, flow modification by the Coriolis force (due to the Earth's rotation), thermobaric effects (stratification by hydrostatic pressure variations (Boehrer and Schultze, 2008; Boehrer et al., 2008)) and heat flow from sediments. In late winter, the surface snow melts and heat is added to the near surface regions of the water column by penetrative solar radiation, which is destabilizing (more on this below) thereby inducing vertical currents. As climate change continues to affect ice cover, Kirillin et al. (2012) remarks that there may be yet-undiscovered feedbacks that could lead to acceleration of ice cover loss. This review only scratches the surface of the interesting mechanisms one must consider when studying ice cover and the dynamics below.

There are several historical reasons why winter limnology was generally avoided. One such example was the difficulty in acquiring data in order to verify numerical models. For example, the review by Ozersky et al. (2021) defines logistical winter as "the period when the lakes become difficult to access due to dangerous weather conditions, insurance rules or the presence of ice cover that presents a 'hard stop' to most Great Lakes research vessels". There is simply an inherent danger associated with going out onto an ice pack to collect data. This danger warrants extra training and specialized equipment, both of which may come at an increased cost potentially deterring the study of lakes in the winter.

Another example is that the winter season was traditionally deemed ecological insignificant when compared to the summer. On the contrary, the article by Powers and Hampton

(2016) provides a resource (born out of a June 2016 ASLO meeting) that highlights recent advances in studies of the under-ice microbiome, ice phenology, under-ice physical limnology, and under-ice primary production. This article exists to guide researchers of summer limnological processes to a library spanning the lesser known wintertime literature. This paper restricts reviews to those found only in the journal *Limnology and Oceanography*. A more recent review article by Jansen et al. (2021) provides key interdisciplinary research questions for the emerging field of winter limnology, some proposed methods to answer these questions, and the level of field-specific expertise required to answer them. The main thrust of this article is to urge specialists in hydrodynamics, biogeochemistry, and ecology to work together in the emerging field of winter limnology.

The importance of wintertime limnology in Canada can be understood with the use of an example; Lake Erie of the Laurentian Great Lakes. The Laurentian Great Lakes are composed of Lake Superior, Lake Michigan, Lake Huron, Lake Ontario, and Lake Erie. They form an environment that many residents of Ontario and the Northern United States rely upon (e.g. for drinking water) and to which their lives are intimately linked (e.g. through tourism). These bodies of water are also one of the main drivers for the local and regional economies. Lake Erie is the shallowest of the Laurentian Great Lakes, with an average depth of about 19 metres. It is about 388 km long and 92 km wide. A unique characteristic of Lake Erie among the Laurentian Great Lakes is that it has three distinct basins. The shallowest is the western basin, averaging 7.5 metres in depth, where the Detroit River acts as a major inflow. The deepest is the eastern basin, with an average depth of 27 metres, where the Niagara river acts as an outflow. In between is the central basin, with an average depth of 18 metres. Though each basin is distinct, water between each often mixes, and this can affect the overall health of the lake.

Lake Erie was deemed ecologically dead due to problematic eutrophication in the 1970s, but a substantial collaborative effort between Canada and the United States brought it back to life (Bruce and Higgins, 2012; Alwin et al., 2015). At the time, modelling showed that the optimal approach to manage widespread eutrophication was to control phosphorous loading. Water quality goals were established and were largely met by 1980 through phosphate detergent bans and municipal point source controls. In recent years, the health of the lake has once again been in decline though. While the input of total phosphorus has remained relatively steady, the re-eutrophication is thought to be due to the introduction of increased amounts of dissolved reactive phosphorous (DRP), a compound that is readily bioavailable and can be used by algae for growth (Alwin et al., 2015). For example, a striking image of Lake Erie taken in March 2012 (the end of a particularly mild winter), shown in figure 1.1, highlights the clear and obvious blue-green colour present throughout the lake indicating the presence of high concentrations of algae. The figure shows that the

concentration was clearly highest in the western basin, near the Detroit River plume. The plume outflow of the Detroit River is known to introduce nutrients and other material into the western basin of Lake Erie. What is not obvious here is how the outflow from the Maumee river affects concentrations of algae. A report from Alwin et al. (2015) indicated that the Maumee and the Detroit rivers were responsible for about 88% of the phosphorus by mass introduced into the western basin and about 53% for the entire lake.

A three year long study of the health of Lake Erie was performed by Twiss et al. (2012) and provided a working hypothesis that "algal production [in Lake Erie] in the winter may help fuel summer hypoxia" (hypoxia occurs when the dissolved oxygen concentration falls below 2 mg O_2/L, while anoxia occurs when it falls below 0.1 mg O_2/L). Indeed they found that *chl-a* concentrations were higher in many parts of the lake in the winter than in the spring. Sustained high concentrations of *chl-a* are usually indicators of poor water quality and high phytoplankton biomass. That being said, their study did not make solid conclusions that these higher concentrations would lead to hypoxia. To supplement this hypothesis, Reavie et al. (2016) found that in the winter, the phosphorus needs of *A.islandica* were readily satisfied while increased levels of silica that came from Lake Huron were found to correlate with intense winter-spring blooms that in turn lead to hypoxia in the central basin. They argue that winter–spring diatoms are a critical piece of the hypoxia story that must be included in predictive models.

The impacts of climate change will exacerbate the role that the winter plays on the dynamical aspects of under-ice environments. For example, as the climate continues to warm, the prevalence of mild winters will only increase, potentially leading to devastating feedbacks. For example, Fujisaki et al. (2013) performed simulations of the interannual variability of ice cover on Lake Erie from 2003-2012 to model the lake circulation beneath, and they found that in the anomalously mild winters, there was a more energetic coastal flow from added wind stress due to the lack of ice cover. They claimed that this could have an impact on pollutant dispersion, wave activity, and lake ecology. Beall et al. (2016) commented that suppressed diatom growth due to lesser ice coverage may have impacts for late summer events. The examples they brought up were the late summer hypoxic events that occurred in the summers after 2002 and 2012. Both of these summer seasons followed uncharacteristically low ice seasons (Zhou et al., 2015).

Many dynamical studies of Lake Erie in the winter are concerned with the transport of pollutants and its water quality in general, and the evidence presented above clearly shows that it is a noble pursuit. However, models that focus on accurately representing water quality at the scales relevant to Lake Erie often misrepresent important aspects of the fluid physics. As an example, consider the work of Oveisy et al. (2014), who used a coupled hydrodynamic-water quality model (Leon et al., 2011) to simulate ice cover dynamics, win-

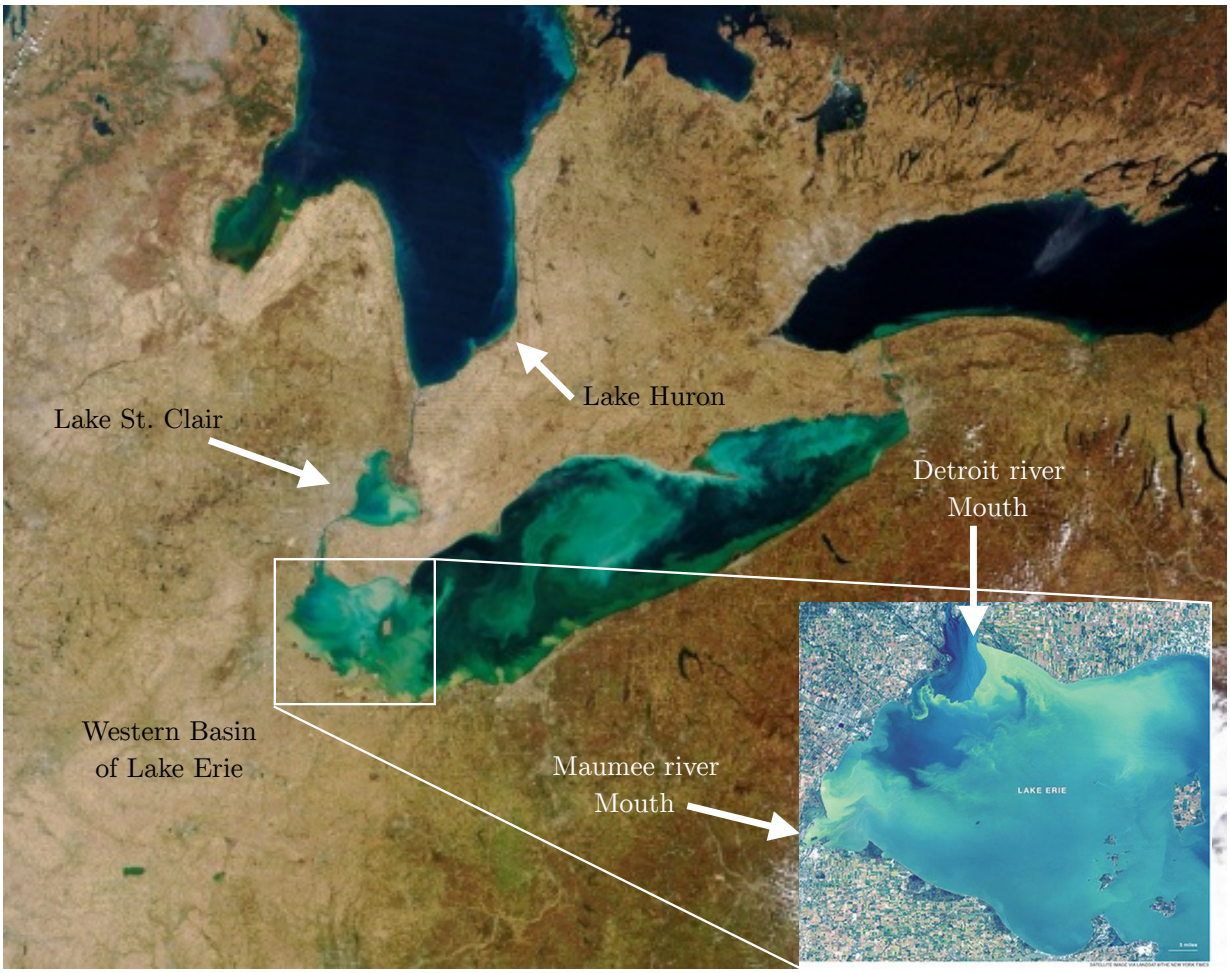

Figure 1.1: MODIS imagery of an algal bloom in March 23, 2012. The blue-green colour indicates a high concentration of algae. Notice that the western basin is completely blue-green (credit NASA)

ter thermal structure and water quality in Lake Erie from October 2004 to April 2005. In this study, the horizontal resolution was 2 km and the minimum vertical resolution was 0.5 m, and consequently their model made the hydrostatic assumption (the gravitational force is balanced by a vertical pressure gradient). For their purposes, these choices were probably adequate because small-scale non-hydrostatic motion would have not been represented on the coarse grid. However, there is a larger issues with properly representing the vertical mixing in these models, especially in the late winter. Accurately accounting for the vertical mixing is of utmost importance for predicting the heat distribution within the lake, however, under the hydrostatic assumption, the vertical mixing must be parameterized. Properly representing the seasonal thermocline is a common issue in the study of Lake Erie, and misrepresenting the summertime stratification can have serious implications for predicting ice cover fractions in the following winter. Leon et al. (2011) (the model upon which the study of Oveisy et al. (2014) is built) commented that the seasonal thermocline depth in their model was much more diffuse than in observations, indicating that the mixing parameterization and potentially numerical viscosity may be mixing the water column too much. Djoumna et al. (2014) compared two hydrodynamic models (the MITgcm (Campin et al., 2019) and GETM (Burchard, Hans and Bolding, Karsten and Umlauf, 2011)) and several turbulent mixing parameterizations and compared the ability of each to reproduced the seasonal thermocline for 2002 and 2008. They noted that all of the parameterizations reproduced the stratification reasonably well in shallow regions, but average temperatures and thermocline depths varied between each turbulence model. Djoumna et al. (2014) suggested that a new parameterization specifically designed for large shallow lakes should be implemented to accurately represent the seasonal thermocline. Difficulties like this motivate a smaller scale approach to studying the dynamical processes relevant to large lakes in the winter. With increases in computing power, small scale simulations can be used to develop better and more comprehensive parameterizations that can improve existing models of large scale processes of the whole lake. However, identifying the small scale processes presents a challenge because of limited field data, but as discussed in Powers and Hampton (2016), there has been a shift in how wintertime processes are considered by the limnological community.

Pursuant to this, we choose to focus on small scale examples of a class of fluid flow known as a "density driven flow". Spatial variations of a fluid's density drive motion as the system attempts to achieve the most stable state with minimum potential energy. In this thesis, we will focus on flows that are primarily density driven in cold water temperatures (wintertime temperatures characteristic of those in lakes in Canada). An important thread between many of the physical research questions mentioned in Powers and Hampton (2016) and Jansen et al. (2021) involves understanding and predicting the temporal and

spatial variability of heat and energy within the water column. Energy in the form of heat that enters the system often drives horizontal and vertical motion which in turn modifies flows beneath ice, and density driven flow can move this heat around the body of water. Within this thesis, two canonical density driven flows are considered. They are penetrative convection by solar radiation, and gravity currents. A more detailed introduction for each will take place in the respective chapters, so here we will only give a broad introduction.

Convective instabilities occur when denser fluid lies over lighter fluid. This setup is gravitationally unstable and the dense fluid sinks, causing the lighter fluid below to flow upwards. This process is called convection which generates convective plumes. The vertical currents generated are an important mechanism for the vertical transport of dissolved oxygen, organic and inorganic material, and pollutants. Convection occurs in many different circumstances but we will contain the discussion to EGFD related contexts. Convection is a very important mechanism in the ocean; Vreugdenhil and Gayen (2021) reviews recent research directed towards nocturnal convection, convection due to evaporative cooling, winter convection, open-ocean convection, and polynya convection. Additionally, a host of process related to convection can occur in the atmosphere (take moist convection for example, a review of which can be found Stevens (2005)).

In terms of convective processes in lakes, a modern resource can be found in Bouffard and Wüest (2019). They highlight the most widely relevant forms of convection that occur in lakes, but here we will highlight only one. A primary discussion point of Bouffard and Wüest (2019) is that convection beneath ice is responsible for a host of processes that have wide ranging implications for both the present and future states of the water column. For example, Yang et al. (2017, 2020) showed that overturning generated by vertical convection in the winter may have serious implications for dissolved oxygen (DO) concentrations observed during the subsequent spring in Lake Simcoe, Canada. Their data shows vigorous convection beneath ice shortly after the surface snow melted. This resulted in a burst of vertical transport of DO leading to supersaturation across much of the water column. Prolonged supersaturation of DO can lead to gas bubble disease in fish resulting in significant mortality.

The second variety of density driven flow that is discussed in this thesis is that of a gravity current. A gravity current is a current that flows horizontally along a surface, and is driven by the density difference between it and the fluid it is immersed in. Gravity currents can be positively buoyant (they flow along the upper surface of whatever they are flowing into), they can be negatively buoyant (they sink and flow along the bottom surface), or they can even flow at some mid-depth if the medium is stratified. Gravity currents provide a canonical example of density driven flow and have often been used in numerical and laboratory scale studies to represent much larger scale phenomena. Gravity currents in the

atmosphere can manifest themselves as thunderstorm outflows or sea-breeze fronts; both of which are a result of cold and dense air penetrating into a warmer and lighter mass (Simpson, 1982, 1999). Wells and Dorrell (2021) review a special type of gravity current called a sediment-laden gravity current, or turbidity current. These kinds of currents can occur in both oceans and lakes. Turbidity currents can be initiated by sediment-laden river plumes flowing into larger bodies of water, underwater landslides, or even resuspension by intense storms. These kind of currents can travel large distances and are responsible for deposition of sediments along the ocean or lake floor.

Gravity currents can also originate from shallow near-shore regions of lakes, called sidearms. Since shallow regions have a smaller mass of fluid to store heat, they often change temperature much faster than deeper regions. In this case, a horizontal temperature gradient (and therefore density gradient) is formed between shallow and deeper regions, and this leads to a gravity current and subsequent horizontal transport (Bouffard and Wüest, 2019). For example, Ulloa et al. (2019) shows numerical simulations of winter convection in a small lake and highlights the formation of a gravity current that originates in the shallower regions of the lake. The authors found that the emergent currents generated in the near shore regions of the lake increase the rate of warming of mixed layers near the middle of the lake in the late winter. Finally, gravity currents also represent an environment that exhibits the coexistence of coherent structures and turbulence and have been extensively studied in a numerical setting (Härtel et al., 2000a,b; Ouillon et al., 2019).

Lastly, the type of studies discussed within this thesis are known as "process studies". It is important to identify the utility of a process study and this can be understood through the use of a comparison to what it is not. If one wishes to study a full system, the approach is to include every factor that might have a role to play in the dynamics. The goal is to maximize realism within the context of the problem to make broad conclusions about the system. At the largest spatial and temporal scales relevant to humans, a common kind of system model is called an Earth System model (ESM) (these can be considered successors to Regional Climate Models, or RCMs (Tapiador et al., 2020)). For an ESM, the goal is to model the most complete form of the Earth system. This typically includes the interactions between the physical climate (the atmosphere, oceans, land surfaces, and sea-ice) and biogeochemical processes (the carbon cycle, or even human interactions with the climate) (Flato, 2011). An in depth discussion of ESMs is beyond the scope of this thesis, but a success story of ESMs (from a scientific standpoint and not a political one) is their use in the IPCC 2021 Report (Szopa et al., 2021). This report uses comparisons of data from different ESMs to make predictions about the future of Earth's climate at different levels of confidence. RCMs have been used with success before, but require information about the boundaries of the region that is being simulated.

A drawback to full system studies is that they must make some strong assumptions about the flows they are modelling. A traditional example is that the boundaries of ESM components (ocean, land, ice sheets, and atmosphere) do not evolve over the course of a simulation. However, a more realistic ice sheet model must include the horizontal and vertical variation of these ice sheets which are capable of covering and uncovering land and ocean, as well as displacing sea ice. For an ESM that does not already include such mechanisms it could require massive model reconfiguration (Fyke et al., 2018) to do so. An example of a drawback for a RCM is the significant simplification of the influence of lakes (in fact, sometimes they are ignored altogether). For instance, in their study of the impact of the Laurentian Great Lakes on the regional climate, Notaro et al. (2013) commented that the horizontal circulation and movement of ice in their lake model component was ignored, and the lack of simulated lake circulation and horizontal heat transport resulted in biases in the spatial distribution of both water temperature and ice cover. Furthermore, they commented that the ice cover in deep regions of Lakes Superior and Michigan were underestimated because overturning in the lake was ignored. Reduced ice cover can lead to an increase in the heat absorbed by the lakes (less reflection of shortwave radiation), but in contrast to this, ignoring overturning also underestimates the lake's capacity for heat absorption as deep mixing can no longer occur, especially in the late winter. Generally, the increased heat absorption due to the lack of ice cover does not balance the reduced heat absorption by ignoring overturning.

Flato (2011) provides a discussion about the necessity of parameterization, currently the only means of including vitally important small and micro-scale processes like cloud nucleation in an ESM, or overturning in a RCM. Flato (2011) also mentions that kilometre scale processes like atmospheric convection should be explicitly resolved, but are often parameterized due to computational resource limitation. All parameterizations come with modelling assumptions, not all of which are satisfied generally. This can lead to misrepresentations of the small scale physics. Since the larger scale Earth systems are very sensitive to the small scale unresolved processes, the misrepresentation of these processes can lead to unrealistic feedbacks within the system.

In contrast to a system model is the idea of the process study. In a process study, a reductionist approach is taken, in a sense sacrificing context for idealism and control. Process studies are the building blocks of fluid mechanics, and by taking a reductionist approach to modelling a single physical process, its role can be studied and identified in its most true sense with the fewest uncertainties possible. Therefore, a process study is the best representation of a truly isolated physical process. In the most idealized and simple form of a problem, a solution to the system can typically be written down by hand. For instance see any undergraduate or graduate text on fluid mechanics like Kundu (1990)

for a host of toy problems. Toy problems, while very idealized, often provide a basis for which the results of more complex numerical models can be compared to. Numerical models and laboratory experiments provide a balance between analytical solutions to toy problems and meaningful results to more complicated ones. Numerical experiments involve simulations of complicated equations at the small scale, leading to the need for far fewer parameterizations when compared to something like an ESM. A numerical example of a process study relevant to this thesis is the study by Lepot et al. (2018). In this experiment, they simulated a homogeneous box of fluid heated from below and looked at the efficacy of convective instabilities at moving heat around the domain. In their experiment the length scales were on the order of a metre and timescales on the order of hours; both of these far smaller than comparable systems found in the natural environment. The heating drove convective instabilities that efficiently mixed the water column. A more detailed description of this reference and the meaning of "efficiently" is saved for chapter 3. An experimental example of a process study is the followup to this work by Bouillaut et al. (2019) who showed small scale laboratory experiments of convection driven by upward focused internal heating. They reported their scaled results so as to be able to compare to literature concerned with larger scale examples of this process, even though their system was at a small scale that is impossible to resolve in something like an ESM. These references are just a few examples of the utility of process studies.

1.2 The Non-linear Equation of State

In many geophysical flows, accurately representing the water density is a crucial precondition to making predictions about the future state of the water column. To calculate the water's density based on other properties (temperature, pressure, concentration of dissolved solids), a mathematical function called an "equation of state" is required. An equation of state (EOS) is a mathematical expression that relates the various thermodynamic variables (also known as state variables) of a solid, liquid, or gas under certain conditions. Equations of state can also exist as tables of data and empirical fits to that data (Lemons, 2009). The work in this thesis concerns itself with the equation of state for freshwater (water with no dissolved solids).

In studies of geophysical fluid dynamics, a common use for the equation of state is to calculate the density (mass per unit volume). The density is an important quantity to know because spatial variations in the density generate variations in other quantities within the flow. As a simple example, consider a vertically stable stratification. If a parcel of fluid of a certain density is instantaneously brought to a region where it is surrounded by less dense

fluid, it will sink and until it reaches its point of neutral buoyancy and then it will oscillate about this point. This happens due to a conversion between gravitational potential energy and kinetic energy. The oscillation radiates energy away in the form of waves, thereby inducing motion far away from the original parcel. Thus, accurate representation of the density of a parcel of water relative to its surrounding is important for understanding resultant motion. Once the density of a region of water is known, then the buoyancy force can be calculated; the force responsible for density driven motion. Below is a discussion some of the key characteristics of the equation of state for water and how those key features are implemented in a simple and useful way.

The equation of state for water composed of a single constituent (no dissolved solids or gases) is generally written as

$$\rho = \rho(p, T), \tag{1.1}$$

where p represents the thermodynamic pressure, measured in Pascals, and T represents the temperature, measured in Kelvin or °C See references for several difference examples of the equation of state in McDougall et al. (2003) and Kantha and Clayson (2000). For the purposes of this thesis, dimensional temperatures are measured in °C.

Assuming an isobaric system (the temperature of the system is independent of its pressure), empirical evidence has shown that the density of fresh water is an increasing function of temperature between its freezing point 0°C, and its temperature of maximum density T_{md} (about 3.98°C) (Kantha and Clayson, 2000). The fact that the water density increases with temperature for temperatures below T_{md} is key to a host of physical processes, and is remarkably important for life as we know it. It is because of this fact the inverse stratification occurs in the winter meaning that the entire water column does not need to reach 0°C before surface ice can form; surface ice that provides thermal insulation for the water below (Bouffard and Wüest, 2019).

After this point, the water density decreases as the temperature is increased. As the mass of water cannot change in the closed system, the volume of the water must expand or shrink in order to accommodate the density change. Adding heat to a system with temperatures greater than T_{md} increases its volume while removing heat decreases its volume. Often, the density $\rho(T)$ of fresh water in this regime is approximated as a sum of a constant reference density $\rho_0 = \rho(T_0)$ plus an anomaly about that reference due to the expansion and contraction of the water. Mathematically, this is written as

$$\rho = \rho_0(1 - \alpha(T - T_0)), \tag{1.2}$$

where

$$\alpha = \frac{1}{\rho_0} \left. \frac{\partial \rho}{\partial T} \right|_{T_0} \tag{1.3}$$

is the constant thermal expansion coefficient, calculated by evaluating the temperature derivative of ρ at the reference temperature, T_0. The negative in front of the anomaly term indicates that $\alpha > 0$. The above is only valid for small $\Delta T = T - T_0$. If ΔT becomes too large, then the assumption of constant α becomes incorrect. Thus, when the linear equation of state is used we maintain the first order effects discussed above. The linear equation of state is ubiquitous in the study of geophysical bodies of water. In these studies, α is typically a prescribed quantity, and its value is chosen to best represent the slope of the freshwater equation of state at T_0.

For characteristic temperature ranges where the non-linear equation of state (NLEOS) cannot be approximated by a linear function, more complex expressions must be used, A common equation of state for seawater is provided in McDougall et al. (2003). This equation of state is written as a ratio of two polynomials, P_1 and P_2, each functions of the salinity (a measure of the concentration of dissolved solids), the potential temperature (the temperature a parcel would attain if brought to a standard pressure state), and the pressure:

$$\rho_{nl}(S, T, p) = \frac{P_1(S, T, p)}{P_2(S, T, p)}. \tag{1.4}$$

This NLEOS is cumbersome to include in a model as it has 25 independent parameters, which creates a massive parameter-space to analyze. When the water is fresh ($S = 0$), both P_1 and P_2 have 8 coefficients each. Furthermore, McDougall et al. (2003) optimized their fitting procedure for deep saline bodies of water, thus their EOS is only accurate for freshwater when the pressure is equivalent to the surface pressure ($p = 0$). This further reduces the total number of parameters to 9. Their specific values are given in McDougall et al. (2003). Some cold water focused studies will further simplify the full freshwater NLEOS so that it includes only 3 parameters: T_{md}, a fitting constant, C, and the maximum density ρ_{md}. Olsthoorn et al. (2019) recently used a simple equation of state in this form:

$$\rho_q = \rho_{md} - C(T - T_{md})^2. \tag{1.5}$$

To determine the parameter C, a quadratic function of the form (1.5) is fit to the freshwater version of the McDougall et al. (2003) NLEOS ensuring that T_{md} and ρ_{md} are the same for the quadratic and the full NLEOS. More discussion on the quadratic equation of state will take place later in chapters 3 and 5.

Other freshwater studies such as Hanson et al. (2021) use the equation of state from Brydon et al. (1999). This NLEOS includes salinity and pressure effects, but when those effects are ignored, this EOS becomes cubic in temperature, but near T_{md} the behaviour is

predominantly quadratic. It is written as

$$\rho_c = \rho_0 + c_1 T + c_2 T^2 + c_3 T^3, \tag{1.6}$$

where the constants c_0, c_1, c_2, and c_3 are given in Brydon et al. (1999). In this equation of state, T_{md} is not an explicit parameter but can be calculated as

$$T_{md} = \frac{-2c_2 - \sqrt{4c_2^2 - 12c_1 c_3}}{6c_3}. \tag{1.7}$$

More discussion on the cubic equation of state will take place later in chapter 4.

Figure 1.2 provides a comparison of the three NLEOSs described above. Panel (a) shows the density anomaly in the range 0°C to 10°C, and panel (b) shows the normalized thermal expansion coefficient. In this range, the three NLEOSs are all essentially quadratic, however there is a systematic vertical shift for the cubic form. This is probably a symptom of the optimization procedure used to calculate the coefficients in Brydon et al. (1999) (they assumed that it would only be used for salty water). This shift in the NLEOS from Brydon et al. (1999) is ultimately inconsequential as the density differences are the driver of motion, and not the magnitudes themselves. The density differences are better quantified by the variable thermal expansion coefficient. The expansion coefficients are all nearly linear in this temperature range, and we can see that the spread in the values of the three NLEOS's is about 10%, so the differences are not substantial for the purposes of the processes studies presented in this thesis. If instead we were trying to speak about a specific body of water and match results to data from that body of water, the difference could potentially be meaningful, so choosing a simplified NLEOS would not be advisable.

1.2.1 Cabbeling

In freshwater, the non-monotonic nature of the NLEOS near T_{md} leads to a phenomenon known as cabbeling. A basic example of cabbeling in freshwater can be understood by considering two parcels of equal density but different temperatures and what happens when they mix. If the two parent parcels have temperatures T_1 and T_2, to a good approximation, the child parcel will have a temperature $T_3 = \frac{1}{2}(T_1 + T_2)$, assuming that the parents are of equal mass. However, the density of the child parcel will be greater than the average density of the parent parcels. Cabbeling also occurs in the ocean because the density of seawater is a function of both the salinity and temperature, and there is a whole separate literature concerned with saltwater/freshwater cabbeling. Parcels of fluid along the same isopycnal can mix, and this generates denser water that sinks. An example of a study

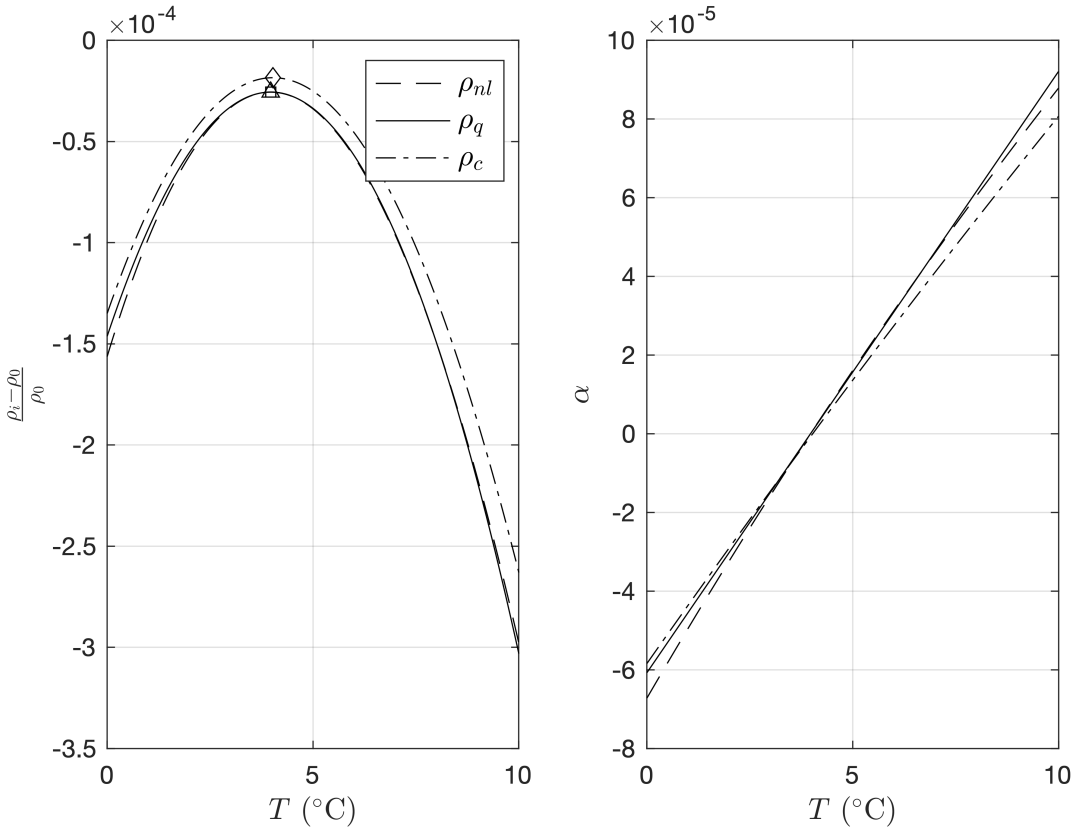

Figure 1.2: The non-dimensional density anomaly about 1000 kg/m^3 for freshwater between $0 - 10$°C is shown in panel (a), while the thermal expansion coefficient in the same temperature range is shown in panel (b). Each curve corresponds to the NLEOS of Jackett and McDougall (1995) (dashed), Olsthoorn et al. (2019) (solid), and Hanson et al. (2021) (dot-dashed). The maximum density of each curve is highlighted on each curve by a marker. The maximums of the full NLEOS and the quadratic EOS are coincident.

of salt/fresh cabbeling is found in Shakespeare and Thomas (2017). Since this thesis is only concerned with freshwater dynamics, the study of saltwater/freshwater cabbeling is intentionally ignored.

We now allow the parent parcels to have different densities, allowing us to discuss two categories of cabbeling in this thesis. The first is weak cabbeling which occurs when the density of the child parcel is greater than the average of the parent densities, but is still lower in magnitude than one parent and higher than the other. The second category will be called strong cabbeling, which aligns with the more traditional view where the child density is greater than that of both the parents. Strong cabbeling is especially interesting because (in the absence of some other equal and opposite forcing mechanism) the relative density of the child parcel causes it to sink and generate vertical currents (downwelling). In this thesis, "strong cabbeling" and "cabbeling" will be used interchangeably, but when weak cabbeling is being discussed, the qualifier "weak" will always be used.

One relatively common natural phenomenon that exhibits cabbeling is the thermal bar. A thermal bar occurs when two masses of water with temperatures on different sides of T_{md} are adjacent and mix together. Thermal bars form in both the autumn and spring in many lakes, but autumn thermal bars are often disrupted by wind mixing, so springtime thermal bars are reported on more often. To form a spingtime thermal bar in a lake, a mass of warm water whose temperatures are greater than T_{md} (this could be fed by a river mouth for example, or by heat exchange with the atmosphere) sits in a shallow region of the lake and is adjacent to a mass of cooler lake water whose temperatures are less than T_{md}. Mixing occurs along the interface between these two fluids which results in the formation of dense water that sinks, causing downwelling. The sinking mass is replaced by near-surface waters which further contributes to cabbeling and dense water formation. Tsydenov et al. (2016) shows 2.5D numerical simulations (the Coriolis force is included, but derivatives of any quantity with respect to the out of the page direction are zero) of the thermal bar in a model for a deep lake. Their figure 4 highlights the main process discussed above. Additionally, if the thermal bar exists on a slope, the dense fluid flows down the slope to deeper regions in the lake. Thermal bars may have significant ecological implications, as well as impacting pollution transport in lakes. For example, horizontal currents typically cannot penetrate the thermal bar, so there is limited horizontal mixing which compounds eutrophication problems in near-shore regions (Holland and Kay, 2003). Historically, the thermal bar was thought to be a mechanism responsible for deep water renewal in Lake Baikal (Shimaraev et al., 1993), but other mechanisms have since been proposed (Schmid et al., 2008).

A more vigorous example of strong cabbeling where horizontal currents may form in freshwater may be found near a power plant outflow. Power plants are often adjacent

to a lake, river, or some other body of water and will use this ambient water to cool the internal components. This water absorbs heat and is expelled back into the body from which it came. In the winter, the ambient water may approach the freezing point, so there is potentially a significant temperature difference between the discharged water and the ambient water. When the warmer water is expelled into the cold ambient, it is initially less dense and will float. However, as the warm water mass mixes with the ambient water, it becomes denser and sinks. Additionally, there may be vigorous mixing due to mechanical energy input from outflow of the plant, further inducing mixing and cabbeling. A recent study by Faulkner et al. (2021) shows numerical simulations of the dispersion of thermal discharge from Heysham power station (UK). This study serves as an example of the potential temperature differences between expelled water and ambient water. They showed that discharged water was between 3 and 9 degrees warmer than the ambient water in the winter and spring. Data from Landsat 8 shows that the ambient water was between 4 and 6 degrees in the winter and as high as 13 degrees in the spring.

Large scale cabbeling is difficult to study at high resolution with direct numerical simulations due to the characteristic length scales required to study it. For example, thermal bars have been observed to extended several hundred metres lakeward and several tens of metres deep in the near-shore regions of Kamloops Lake (Canada) (Carmack, 1979). As an example in a simulation context, the domain used in the study of Tsydenov et al. (2016) models the near-shore regions of Lake Baikal and as such covers 10 kilometres in the cross-isobath direction and 300 metres in depth. In any case, the scales of this phenomenon require the use of turbulence models to estimate the sub-grid scale turbulence and the diffusion of mean quantities. Holland et al. (2001) used a diffusivity that was inversely proportional to the local buoyancy frequency above some small cutoff. Below this cutoff, a constant diffusivity four orders of magnitude greater than the molecular value was chosen. Tsydenov et al. (2016) used the two-parameter $k-\epsilon$ model of Wilcox (1988) to compute the vertical diffusivity, while also using a constant horizontal value. The $k-\epsilon$ model is useful in many contexts as it is the simplest complete turbulence model. However, its performance has been known to suffer in complex flows (though the term "complex" is not exactly precise in this context) (Pope, 2000). As with any empirical model, it can be tuned to fit the specific context. In this thesis, the difficulty of selecting an appropriate turbulence model and tuning is side-stepped by instead performing small scale direct numerical simulations (DNS). More information on DNS is presented in section 2.4.1

1.2.2 NLEOS Parameter

Generally speaking, for a polynomial equation of state, there are a set of NLEOS parameters that characterize the magnitude of the non-linear terms relative to the linear term. The following section is intentionally left general since the exact definition of the NLEOS parameters differ from chapter to chapter. Thus we will speak about it in broad terms here.

The main role of the NLEOS parameter is best understood for the quadratic equation of state in (1.5). This EOS yields a single non-dimensional NLEOS parameter, and its magnitude and sign both play important roles in predicting the dynamics. For studies in cold water, characteristic temperatures responsible for driving motion (often set by initial conditions or relaxation terms for example) are not the only relevant temperatures in the flow. The temperature of maximum density and the proximity of the characteristic temperatures to T_{md} also play a role in the dynamics. Since the characteristic temperatures in the numerator and denominator are determined by the specific context, the role this parameter plays in this thesis will be discussed in the relevant chapters.

Generally speaking, if the NLEOS parameter is large (compared to unity), then we should expect the quadratic term in the equation of state to have a leading order effect on the dynamics. On the other hand, if the NLEOS parameter is small compared to unity, then the quadratic term becomes secondary to the linear one. A recent example of the use of the NLEOS parameter (the authors called it β in their work, but we will adopt Θ) can be found in Olsthoorn et al. (2019). In this study, the authors studied the development of Rayleigh-Taylor instabilities with diffuse interfaces in temperatures below the temperature of maximum density. For given layer temperatures T_1 and T_2, they defined their Θ analogue as

$$\Theta = \frac{T_1 - T_2}{T_1 + T_2 - 2T_{md}}. \tag{1.8}$$

Note that T_1 and T_2 in their study were both greater than T_{md}, so the denominator was never zero. Using this definition and defining a non-dimensional temperature as

$$T = \frac{\tilde{T} - T_2}{T_2 - T_1}, \tag{1.9}$$

the quadratic equation of state from Olsthoorn et al. (2019) became

$$\rho = -\Theta T^2 - (1 - \Theta)T. \tag{1.10}$$

Thus, for Θ near unity, the EOS becomes more quadratic, whereas for Θ near zero, it becomes more linear. In this study, Θ was restricted to be between 0 and 1.

Hanson et al. (2021) performed numerical simulations of a stratified parallel shear flow such that the interface between the two fluid layers crossed T_{md}, thus, mixing across the interface generated dense fluid that would fall to the bottom of the domain. The top layer had a temperature of T_0 and the bottom layer had a temperature of $T_0 + \Delta T$ (ΔT is the temperature difference between the top and bottom layers). In their study, they used the cubic EOS from Brydon et al. (1999), shown in (1.6). Hanson et al. (2021) did not specifically define any non-dimensional parameters to characterize each term in the NLEOS, but we will do that here to provide an example of a recent study with a wider range of NLEOS parameters. Since their equation of state is cubic, we can define two NLEOS parameters, each quantifying the magnitude of higher order terms relative to the linear term. We will call them Θ_1 and Θ_2. Note that in (1.6), the temperature of maximum density is 3.5°C instead of the true value of 3.98°C. As mentioned previously, this is probably an artifact from the optimization procedure to determine the coefficients in Brydon et al. (1999), as their NLEOS is meant to be used for seawater and assumes the salinity is non-zero. The actual value of T_{md} does not matter for the definition of Θ_1 and Θ_2, only the difference between some characteristic temperature and T_{md}. A Taylor series expansion of the equation of state given by (1.6) about T_0 gives

$$\frac{\tilde{\rho} - \tilde{\rho}(T_0)}{\rho_0} = \alpha(T_0)(\tilde{T} - T_0) + \frac{1}{2}\alpha'(T_0)(\tilde{T} - T_0)^2 + \frac{1}{6}\alpha''(T_0)(\tilde{T} - T_0)^3, \tag{1.11}$$

where a tilde represents a dimensional variable, α is the thermal expansion coefficient from (1.3), and a prime denotes a temperature derivative. We can non-dimensionalize the temperature anomaly about the upper layer temperature as

$$\tilde{T} - T_0 = (\Delta T)T. \tag{1.12}$$

Here, T is the non-dimensional temperature for this system and takes values between 0 and 1. Upon substitution of the above into (1.11), we see that the magnitude of the linear term is $\alpha\Delta T$. Dividing the whole equation by this factor, and defining

$$\rho = \frac{\tilde{\rho} - \tilde{\rho}\,(T_0)}{\alpha\Delta T} \tag{1.13}$$

we get

$$\rho = T\left(1 + \frac{1}{2}\Theta_1 T + \frac{1}{6}\Theta_2 T^2\right), \tag{1.14}$$

where

$$\Theta_1 = \frac{\alpha'(T_0)\Delta T}{\alpha(T_0)}, \quad \Theta_2 = \frac{\alpha''(T_0)\Delta T^2}{\alpha(T_0)}. \tag{1.15}$$

Thus, for small Θ_1 and Θ_2, the system behaves as if the density and the temperature were linearly related, whereas for larger Θ_1 and Θ_2, the quadratic and cubic terms are more comparable in size and therefore play a more significant role in the dynamics.

As an example, we will compute Θ_1 and Θ_2 for the CB case in Hanson et al. (2021), as this case is representative of the rest of their runs where cabbeling occurred. This case has $T_0 = 2°\text{C}$, and $\Delta T = 4°\text{C}$. Substituting T_0 and ΔT into the above equations gives $\Theta_1 = -2.6$ and $\Theta_2 = 0.14$. In this formulation, Θ_1 is significant compared to unity, so we should expect effects from this term to be apparent. Additionally, Θ_2 is smaller indicating the cubic term in the cubic NLEOS plays a relatively insignificant role.

1.3 Thesis Layout

The remainder of thesis is laid out as follows. Chapter 2 is a broad technical background section that highlights the common mathematical and computational threads that are used throughout this thesis. A discussion of the equations of motion and details on the Boussinesq and incompressibility approximations follow. The chapter closes with a discussion of some of the broad details of software used, as well as a brief section highlighting the motivation for using such a model. Following the Methods chapter, the following three chapters (chapters 3, 4, 5) discuss three different classes of process studies. Each chapter considers the dynamical response under a different characteristic interval of the NLEOS. Chapter 3 (published as Grace et al. (2022)), highlights the evolution of a water column as heat is added. The added heat increases the density in this study, but this results in only relatively small spatial density differences. This chapter highlights one of the most important features of the non-linearity of the freshwater EOS; its positive slope between the freezing point and T_{md}. This chapter discusses the development and degeneration of convective instabilities in the presence of mean shear characteristic of under-ice flows. Chapter 4 (published as Grace et al. (2021)) begins to discuss the dynamic response for a larger but still monotonic interval of the NLEOS. In this chapter, the evolution characteristics of two classes of gravity current are compared (one that is positively buoyant and one that is negatively buoyant). The characteristic density difference is controlled by the choice of initial conditions. Finally, chapter 5 (yet to be published at the time of this writing) extends the work of chapter 4 by allowing non-monotonicity of the NLEOS and discusses the general evolution of a cabbeling gravity current. In this chapter, under a particular set of circumstances, an initially positively buoyancy current mixes and generates a coherent bottom flowing current. The characteristics of this process are investigated and quantified. Figure 1.3 highlights the different temperature intervals for each chapter as well as the re-

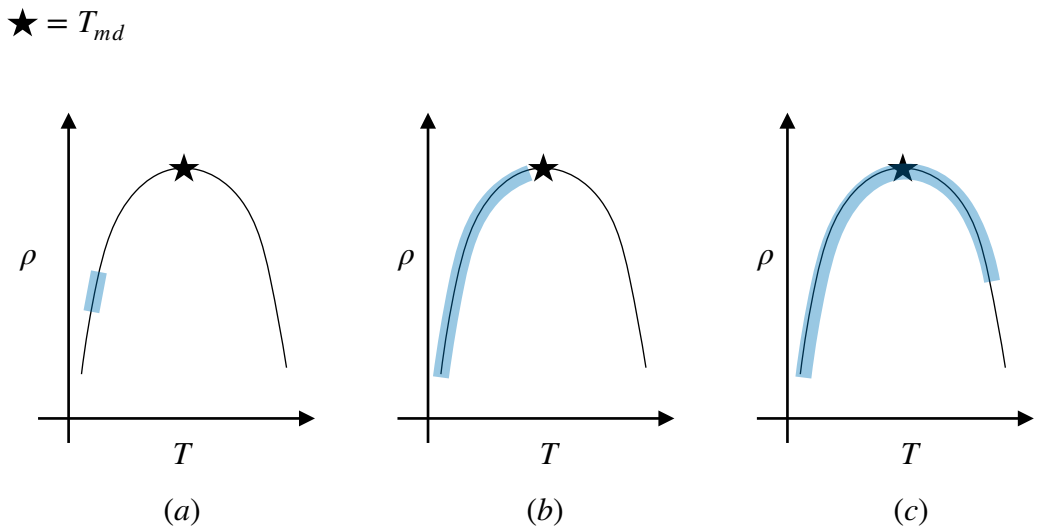

Figure 1.3: A schematic representation of the different intervals of the NLEOS that chapters 3, 4, and 5 are concerned with. Panel (a) (chapter 3) shows a small approximately linear sub-interval of the NLEOS. The key is that heat is continually added to the domain and the interval stays nearly linear. Panel (b) (chapter 4) shows a larger monotonic sub-interval that is non-linear. Panel (c) (chapter 5) shows a non-monotonic and non-linear sub interval of the NLEOS.

sultant density differences. Lastly, chapter 6 concludes the work and provides some future directions for the thesis as a whole.

Chapter 2

Technical Background

This chapter presents the mathematical and physical foundations upon which the rest of this thesis is built. The technical background below will provide information on common threads between each chapter, but specific techniques and methods will be highlighted in the chapter they appear in. The goal of this chapter is to highlight some of the details of the full equations so we can understand where they come from and what assumptions we make to get them. After sketching the derivation of the equations of motion, the incompressibility assumption and the Boussinesq approximation will be discussed. Following this discussion, the numerical model used throughout this thesis is introduced. The technical aspects of the numerical model are briefly highlighted, but the primary focus will be placed on the reasoning behind the choice of numerical method and its strengths.

2.1 Conservation Laws

A conservation law is a mathematical sentence that describes how a quantity of interest changes in space and time, and what mechanisms or processes are responsible for this change. Our understanding of every physical process is derived from a conservation law at some stage, and it is important to understand where these laws come from and what equations they lead to. In the following section, the equations of motion for a fluid will be derived under only the most basic assumptions, and the approximations used in this thesis will be discussed and applied afterwards. This exposition is included as a reminder that the main results of this thesis (and many others that use the same equations) are approximations to an even more complicated set of equations. Additionally, this section can also be provided as a resource or primer for new researchers to get a brief overview of

where the common approximations come from. The work below is from a combination of several sources. Specifically from Kundu (1990), Vallis (2006), and Batchelor (2000).

The conservation of mass, momentum, and energy will be used throughout this thesis. For the sake of exposition, we will derive the conservation of mass from its integral form, and show how it can be expressed in differential form. The conservation of momentum and energy can be derived by following similar procedures, but will only be highlighted here. A more in-depth and complete derivation of conservation of momentum and energy for a fluid can be found in Kundu (1990). For readers who would like to skip the discussion of the full equations of motion and only want to see their final form after the application of common approximations, please skip to section 2.4.

2.1.1 Conservation of Mass

The total mass of a fluid M within a region W can be expressed as the volume integral of its density, ρ, over this region. The region W is time-dependant, meaning that it can deform as the fluid flows. This requires the definition of two objects used in the study of fluid dynamics. The first is called a fluid particle, and the second is called a material volume. A fluid particle is a small packet of fluid that has enough molecules to have consistent thermodynamic properties, but is large enough to adhere to the continuum assumption. A material volume is a set of fluid particles identified at the initial time that retain their identity as the fluid flows. As a simple example, think of an initially dyed packet of fluid that is followed as the flow evolves. We can write the total mass in a region W as

$$M = \iiint_{W(t)} \rho \, dv. \tag{2.1}$$

Assuming the mass within W is conserved over its evolution, the statement of the conservation of mass is

$$\frac{dM}{dt} = \frac{d}{dt} \iiint_{W(t)} \rho \, dv = 0. \tag{2.2}$$

As W itself is a time-dependant region, the time derivative and integral do not commute directly. To solve this problem, we will use the Reynolds Transport Theorem (RTT). The RTT re-expresses the time derivative of the integral of a quantity as a sum of the integral of the time rate of change of the quantity within the region $W(t)$ plus the flux of quantity through the bounding surface of the region. The RTT is a generalization of the Leibniz integral rule from calculus (Kundu, 1990). Using the RTT, we can write the integral as

$$\iiint_{W(t)} \left(\frac{\partial \rho}{\partial t} + \nabla \cdot (\rho \boldsymbol{u}) \right) dv = 0, \tag{2.3}$$

where $\boldsymbol{u}$ is the flow velocity. The region W is finite, and the integrand is continuous over W. Since (2.3) holds for any W, we can write the conservation of mass in differential form as:

$$\frac{D\rho}{Dt} + \rho\nabla \cdot \boldsymbol{u} = 0. \tag{2.4}$$

This equation indicates that changes in the fluid's density changes due to compression and expansion. Here, the operator $\frac{D}{Dt} = \frac{\partial}{\partial t} + \boldsymbol{u} \cdot \nabla$ is the material derivative. It appears often in studies of fluid flows. The first term represents the time rate of change of a quantity at a particular location in space, while the second term represents the variation of a quantity as it moves with the flow. Note that steady flow is one where $\frac{\partial X}{\partial t} = 0$ for all quantities X.

2.1.2 Conservation of Momentum

The conservation of momentum is a statement of Newton's second law, commonly written as simply as $\boldsymbol{F}_{net} = m\boldsymbol{a}$, or that the net force acting on a body is proportional to its acceleration, with the constant of proportionality being the mass of the body. For this equation to be useful, we must first determine the forces acting on the fluid. In this thesis, we must account for two classes of force: body forces and surface forces. In this thesis, the only body force considered is the gravitational force. Surface forces, or the forces exerted on an area element of size dA by its neighboring elements, on the other hand are specific to continua and include normal forces and shear forces. Using a technique similar to the one we used for the conservation of mass (albeit with a more details), we can write the conservation of momentum in differential form as

$$\rho\frac{D\boldsymbol{u}}{Dt} = -g\rho\hat{\boldsymbol{k}} + \nabla \cdot \boldsymbol{\tau}. \tag{2.5}$$

The gravitational force per unit volume on the fluid is represented by $-g\rho\hat{\boldsymbol{k}}$. This force only acts in the direction parallel to gravity (the vertical direction in this thesis). Here, $\nabla \cdot \boldsymbol{\tau}$ represents the internal forces within the fluid. Assuming a Newtonian fluid, we can use the linear constitutive law for a fluid (the stress-rate of strain relationship) to relate the internal stresses to the velocity field. We can recast internal forces in tensor notation so as to be able to use the Einstein summation convention (repeated indices imply summation):

$$\tau_{ij} = -p\delta_{ij} + 2\mu e_{ij} + \lambda e_{kk}\delta_{ij} \tag{2.6}$$

where e_{ij} is the rate of strain tensor, δ_{ij} is the Kronecker Delta, μ is the dynamic viscosity, and λ is the bulk viscosity. The bulk viscosity is only relevant for compressible fluids, whereas μ is a very important parameter for compressible and incompressible fluids alike.

The stress tensor is a sum of two basic parts; the isotropic component that would exist if the fluid were at rest (this is the first term in the above equation), and the deviatoric stress tensor, which is non-isotropic and is a result of velocity gradients within the flow (this is the sum of the last two terms in the above equation). We can use tensor notation to express the last term in (2.5) as

$$\tau_{ij,j} = -p_{,j}\delta_{ij} + \mu\left(u_{i,jj} + u_{j,ij}\right) + \lambda u_{k,kj}\delta_{ij} \tag{2.7}$$

(the comma between indices represents a derivative with respect to the indices after it) where the first term represents the contribution to the total stress by the thermodynamic pressure (the diagonal entries in the rate of strain tensor), the second term represents the shear stresses (the diagonal entries of the rate of strain tensor), and the third term is the volumetric strain rate. Upon contraction and expressing back in vector notation, we have

$$\nabla \cdot \boldsymbol{\tau} = -\nabla p + \mu\nabla^2\boldsymbol{u} + (\mu + \lambda)\nabla(\nabla \cdot \boldsymbol{u}). \tag{2.8}$$

Thus, the full variable density conservation of momentum for a Newtonian fluid becomes:

$$\rho\frac{D\boldsymbol{u}}{Dt} = -\nabla p - g\rho\hat{\boldsymbol{k}} + \mu\nabla^2\boldsymbol{u} + (\mu + \lambda)\nabla(\nabla \cdot \boldsymbol{u}). \tag{2.9}$$

The first term on the right is the pressure gradient. The second term is the force of gravity per unit volume, the third term represents the diffusion of momentum by viscosity, and the last term represents the diffusion of momentum by compression of fluid elements.

As a brief aside, there is a point of nuance with the definition of the pressure in the above equation. Kundu (1990) points out that thermodynamic quantities are only defined for equilibrium states. Since the flow state is not generally in equilibrium (there is motion, diffusion of temperature and momentum, etc.), the pressure defined above is not exactly the thermodynamic pressure. However, we can assume that the relaxation timescale for the molecules in the fluid is much shorter than the timescales of the motion, thus allowing us to interpret the motion as a progression through a series equilibrium states. This allows p to become an adequate representation of the true thermodynamic pressure. This matters for the calculation of other state variables through the equation of state, as only thermodynamic variables play a role.

2.1.3 Conservation of Energy

The conservation of internal energy is a statement of the first law of thermodynamics: the rate of change of internal energy with time is due to external heat fluxes (heat entering the

system increases the temperature of the flow which in turn increases the internal energy), pressure work (compression of elements by the system resulting in a decrease in volume of elements, thereby increasing the internal energy). We could instead write the conservation of stored energy (internal + mechanical), but the total mechanical energy is not a separate law, and is derivable from the conservation of momentum. As an example, see Kundu (1990). We can subtract the total mechanical energy from the stored energy to get a conservation law for the internal energy per unit mass e, which is written as

$$\rho \frac{De}{Dt} = -\nabla \cdot \boldsymbol{q} - p(\nabla \cdot \boldsymbol{u}) + \varepsilon. \tag{2.10}$$

The first term on the left represents the rate of change of the internal energy per unit volume (per volume because we have multiplied by the fluid density ρ). The first term on the right is the divergence of the heat flux. This is easily seen if this term is integrated over a three-dimensional region and Gauss' theorem is used. The second term is the pressure work done on the body, and finally, the last term is the increase in heat due to viscous dissipation, or the rate that kinetic energy is turned into heat via fluid friction. The viscous dissipation is defined as $\varepsilon = 2\mu e_{ij} e_{ij}$ (Kundu, 1990) and is always greater than or equal to zero. At this stage there is no simplification that can be done to this equation.

In this section we have highlighted the conservation of mass, momentum, and energy for a fluid in a very general form. At the moment, they are in a state that is difficult to analyze or simulate numerically, and are infrequently used when considering the motion of water. These equations can be simplified significantly by using two common approximations for the studied of variable density flows; the incompressibility approximation and the Boussinesq approximation. In the following section, these approximations will be discussed, and their impact on the equations of motion will be shown.

2.2 The incompressibility approximation

In this thesis, flows are treated as incompressible. This means that the expression of the conservation of mass is replaced by the incompressibility condition $\nabla \cdot \boldsymbol{u} = 0$. As a reminder, the conservation of mass equation is:

$$\frac{1}{\rho} \frac{D\rho}{Dt} + \nabla \cdot \boldsymbol{u} = 0. \tag{2.11}$$

In order to replace the above with $\nabla \cdot \boldsymbol{u} = 0$, the dominant balance in the above equation must be among the terms u_x, v_y, and w_z, or in other words

$$\left| \frac{1}{\rho} \frac{D\rho}{Dt} \right| \ll \max \left\{ |u_x|, |v_y|, |w_z| \right\}. \tag{2.12}$$

This means that the material derivative is much smaller in magnitude than at least two of the individual terms representing the divergence of the velocity field so that in an approximately incompressible flow, density changes are so small that they have a negligible effect on the mass balance (Vallis, 2006). Under this assumption, stretches of the fluid in one direction are compensated by compressions in another, rather than by changes in density. Thus, under the incompressibility approximation, the continuity equation is replaced by

$$\nabla \cdot \boldsymbol{u} = 0. \tag{2.13}$$

There are several restrictions that must be met for a fluid to be considered incompressible. Practically speaking, they are as follows. The squared Mach number, U^2/c^2, must be much smaller than unity (c is the speed of sound in the relevant media). If waves are under consideration, the ratio of estimated wave propagation velocities to the speed of sound must also be much smaller than unity. Since the characteristic velocities that we are interested in studying in this thesis are all much slower than c, these restrictions are satisfied. Lastly, depths must be much smaller than the ratio c^2/g. In water, this depth is approximately 200 km, so this condition is easily satisfied as the depths presented within this thesis are all on the order of 1 m. Finally, density changes as a result of heat exchange by internal dissipation or molecular diffusion must be small compared to the reference density. An in-depth discussion of these restrictions can be found in Batchelor (2000).

2.3 The Boussinesq approximation

The Boussinesq approximation is a commonly used approach for simplifying the equations of motion for studying geophysical flows, and will be used throughout this thesis. Below, we will summarize discussions provided in Kundu (1990), Batchelor (2000), and Vallis (2006).

The main thrust of the Boussinesq approximation is that the full density field in the equations of motion is replaced by a constant reference density *except* in the buoyancy term. This motivates us to decompose the density into the sum of a reference density ρ_0

and a perturbation about the reference density ρ':

$$\rho = \rho_0 + \rho'(x, y, z, t). \tag{2.14}$$

The perturbation may be due to a stratification, motion, or something else. However, it must be much smaller in magnitude than ρ_0. Furthermore, we can write the full fluid pressure as

$$p = P_0 + p^H(z) + p'(x, y, z, t). \tag{2.15}$$

where it is decomposed into a sum of a constant reference pressure P_0 (the equilibrium pressure on a small element of fluid located at a reference height z_0), p^H is the part of the pressure in hydrostatic balance with ρ_0, and p' represents the pressure fluctuation due to motion. The pressure in hydrostatic balance with ρ_0 is the solution to the following equation:

$$\frac{dp^H}{dz} = -\rho_0 g. \tag{2.16}$$

By substituting (2.14) and (2.15) into (2.9) one arrives at

$$\rho_0 \left(1 + \frac{\rho'}{\rho_0}\right) \frac{D\boldsymbol{u}}{Dt} = -\frac{dp^H}{dz}\hat{\boldsymbol{k}} - \nabla p - \rho_0 g\hat{\boldsymbol{k}} - \rho' g\hat{\boldsymbol{k}} + \mu\nabla^2\boldsymbol{u}. \tag{2.17}$$

Note that we have removed the $(\mu + \lambda)\nabla(\nabla \cdot \boldsymbol{u})$ term because of the incompressibility condition $\nabla \cdot \boldsymbol{u} = 0$. Since we are assuming $\rho'/\rho_0 \ll 1$, the second term in the parentheses on the left hand side can be ignored. Additionally, the vertical derivative of the hydrostatic pressure exactly cancels $-\rho_0 g$, so we arrive at the following equation for the conservation of momentum under the Boussinesq approximation:

$$\rho_0 \frac{D\boldsymbol{u}}{Dt} = -\nabla p' - \rho' g\hat{\boldsymbol{k}} + \mu\nabla^2\boldsymbol{u}. \tag{2.18}$$

In order to ensure that $\rho'/\rho_0 \ll 1$, several conditions must be met. Firstly, the changes in the density fluctuation due to other thermodynamic variables (temperature and pressure for a homogeneous fluid) must be small so that ρ' continues to be much smaller than ρ_0. A discussion is provided in Vallis (2006), but in short, as long as the pressure and temperature fluctuations are much smaller than $\mathcal{O}(10^5)$ atm and $\mathcal{O}(10^3)$ °C respectively, then an $\mathcal{O}(1)$ change in ρ'/ρ_0 cannot occur. Since the conditions within this thesis preclude extremely large pressures and temperature variations, the Boussinesq approximation is justified.

Lastly, we can simplify the internal energy equation. The equation is re-written below:

$$\rho \frac{De}{Dt} = -\nabla \cdot \boldsymbol{q} - p(\nabla \cdot \boldsymbol{u}) + \varepsilon. \tag{2.19}$$

It is important to note that even though we are assuming the fluid is incompressible, we cannot assume that the $p(\nabla \cdot \boldsymbol{u})$ term is small compared to the other terms in this equation.

Following Batchelor (2000), we can write

$$\rho \frac{De}{Dt} = \left(\rho C_p \frac{DT}{Dt} - \alpha T \frac{Dp}{Dt} \right) - p(\nabla \cdot \boldsymbol{u}), \tag{2.20}$$

which is an expression derived from the first and second laws of thermodynamics applied to a material volume. Batchelor (2000) contains a derivation of the above equation, so details are omitted here. C_p is the specific heat capacity at constant pressure (assumed to be independent of temperature in this thesis), and α is the coefficient of thermal expansion of the fluid. Substituting the above into (2.19), we arrive at

$$\rho_0 C_p \left(\frac{DT}{Dt} - \frac{\alpha T}{\rho_0 C_p} \frac{Dp}{Dt} \right) = -\nabla \cdot \boldsymbol{q} + \varepsilon, \tag{2.21}$$

where we have replaced ρ with its reference value ρ_0. We can scale the left hand side of the above equation as

$$\rho_0 C_p \left(\frac{\Delta T}{\tau} \frac{DT'}{Dt'} - \frac{\alpha T^{\inf} P}{\rho_0 C_p \tau} T' \frac{Dp'}{Dt'} \right) = ..., \tag{2.22}$$

where variables with a prime are dimensionless in the above. Here ΔT is a characteristic temperature difference, τ is a characteristic timescale (assume the material derivative of pressure operates on the same timescale τ as the material derivative of temperature), P is a characteristic value for pressure, and $T^{\inf}$ is a characteristic temperature.

The magnitudes of ρ_0 and C_p are about $1000\,\mathrm{kg\,m^{-3}}$ and about $4000\,\mathrm{J\,kg^{-1}\,{}^{\circ}C^{-1}}$ respectively. For a non-linear equation of state, the thermal expansion coefficient α varies with temperature in the range of $0\,{}^{\circ}\mathrm{C}^{-1}$ (at T_{md}) to about $10^{-4}\,{}^{\circ}\mathrm{C}^{-1}$ at 10°C. Any higher temperature could have been chosen because α does not vary much in order of magnitude past this value. Its sign can also be negative or positive depending on whether the temperature is above or below the temperature of maximum density. Finally, for geophysical flows, we can choose $T^{\inf}$ to be in the neighborhood of 300 K (since $T^{\inf}$ is an absolute temperature scale, we have to express its value in units of Kelvin). This leaves two parameters that can control the size of the pressure term in (2.22); the pressure scale P, and the temperature difference ΔT. For simplicity, assume that the temperature is the main stratifying agent. In stratified regions, characteristic temperature differences can be on the order of 10 °C. Since $\alpha T^{\inf}/\rho_0 C_p \Delta T \sim \mathcal{O}(10^{-3})\,\mathrm{atm^{-1}}$ at most, and the characteristic pressure P would have to be about 10^3 standard atmospheres in order for this term to be comparable to

unity. For example, the pressure at the bottom of the Mariana trench (the deepest part of the Pacific ocean) is about of 10^3 standard atmospheres (Vallis, 2006). If the temperature differences within the flow are smaller (say $\Delta T = 1\,^{\circ}\mathrm{C}$), then the pressure would instead have to be 10^2. Of course, with smaller temperature differences, the magnitude of the pressure term becomes more important to the energy balance. However, the pressure required are still much higher than those found in this thesis. From this analysis, it is clear that the pressure term in the conservation of energy equation provides a negligible correction to the overall energy balance, so under the assumptions of this thesis, we can re-write the above equation as

$$\frac{DT}{Dt} = -\frac{1}{C_p \rho_0} \nabla \cdot \boldsymbol{q} + \frac{\varepsilon}{C_p \rho_0}. \tag{2.23}$$

This equation says that changes in temperature of the flow are due only to heat fluxes into the flow, and generation of heat by fluid friction. The heat generated by fluid friction is often ignored in this equation as it is often inconsequential compared to other heat fluxes within geophysical fluid flows. For an example where this term cannot be ignored, consider a lubricant in an engine. One of the primary roles of a lubricant is to absorb heat from friction generated by the mechanical engine components and subsequently to transport this heat away.

The important heat fluxes can be broken into two categories: external and internal. Empirical evidence has demonstrated that heat flow follows Fourier's law of heat conduction $\boldsymbol{q}_{in} = -k\nabla T$. Thus, large gradients induce a large diffusive heat flux, and heat flows from high temperatures to low temperatures. Alternatively, we can specify external heat fluxes as $\boldsymbol{q}_{ext}$ and these could be represented as boundary conditions (longwave radiation incident on the surface of a body of water, or heat exchanged by sensible, latent, or material processes), or as internal forcing terms (shortwave solar radiation, see chapter 3). Substituting in Fourier's law of heat conduction and letting the thermal diffusivity be defined as $\kappa = k/C_p\rho_0$, we can write the evolution of the fluid temperature as

$$\frac{DT}{Dt} = \kappa \nabla^2 T - \frac{1}{C_p \rho_0} \nabla \cdot \boldsymbol{q}_{ext}. \tag{2.24}$$

where we have left the exact form of $\boldsymbol{q}_{ext}$ to be discussed later.

2.4 The equations of motion and numerical solver

The full set of equations of motion after simplification using the Boussinesq approximation read as follows:

$$\frac{D\boldsymbol{u}}{Dt} = -\frac{1}{\rho_0}\nabla p - \frac{\rho'}{\rho_0}g\hat{\boldsymbol{k}} + \nu\nabla^2\boldsymbol{u} \tag{2.25}$$

$$\frac{DT}{Dt} = \kappa\nabla^2 T - \frac{1}{C_p\rho_0}\nabla\cdot\boldsymbol{q}_{ext} \tag{2.26}$$

$$\nabla\cdot\boldsymbol{u} = 0, \tag{2.27}$$

$$\rho = \rho(T), \tag{2.28}$$

where in the above equation, ρ is now the perturbation density about the reference, and we have let $\kappa = k/C_p\rho_0$. The functional form $\rho(T)$ has been left unspecified here, and will be discussed in each chapter.

2.4.1 The SPINS code

The primary results presented in this thesis are a product of data analysis from direct numerical simulations (DNS) of the above equations in different contexts. In this section, we will give a very brief overview of the software used for the numerical simulations and its regular usage. The technical details are spared and the discussion is instead a broad overview of the utility of the software, followed by a discussion of the motivation for using such a model.

The open-source software used for data generation is the pseudo-Spectral Parallel Incompressible Navier-Stokes solver (SPINS) developed in our research group. Technical details can be found in Subich et al. (2013). This software has been used for the study of a wide variety of density driven flow phenomena. An (incomplete) list of examples include studies on the evolution of mode-2 internal waves in various configurations (Deepwell and Stastna, 2016; Deepwell et al., 2017, 2019, 2021), the formation and evolution of solitary waves (Xu et al., 2016; Xu and Stastna, 2018, 2019; Xu et al., 2019; Xu and Stastna, 2020), the evolution of double diffusive systems in various contexts (Penney and Stastna, 2016; Legare et al., 2021), interaction of waves with bottom topography (Olsthoorn and Stastna, 2014; Harnanan et al., 2015, 2017), the evolution and degeneration of internal standing waves (Grace et al., 2019), and perhaps most relevant, the study of parallel shear flows in the cabbeling regime (Hanson et al., 2021). These are just some of the examples of studies

that have used SPINS, and are cited to highlight its broad applicability when studying density driven flows.

SPINS uses an Adams-Bashforth adaptive three level time discretization, which achieves third order accuracy in time, and the code attains spectral accuracy in space (the order of accuracy increases as the number of grid points is increased). For uniformly spaced grid points, fields are expressed in a Fourier basis, and when grid points are clustered, the basis is chosen to be Chebyshev polynomials. Derivatives are calculated using the Fast Fourier Transform (FFT) algorithm when the grids are uniform, and the FFT-based (i.e. matrix free) version of the Chebyshev differentiation matrix used when clustered grids are used. Fourier transforms are performed using a numerical package known as FFTW (Frigo and Johnson, 2005). Finally, the Message Passing Interface (MPI) protocol is used to handle the parallelization procedure. Information on the parallelization scheme can be found in Subich et al. (2013).

One of the design strengths of SPINS is that users can easily design their own case files and can include whatever momentum forcing, thermal forcing, or passive tracer forcing is relevant to their problem without modifying the primary code files. Additionally, various diagnostics are included in the `Science` package, and users can include whichever diagnostics are relevant to the problem at hand. Examples of available diagnostics include four options for the EOS (linear, quadratic, cubic, or full), energy diagnostics from Winters et al. (1995), computation of the viscous kinetic energy dissipation, and computation of the boundary stresses. Diagnostics are available on an iteration by iteration basis and are output to a text file that can be analysed using post-processing tools like MATLAB or Python. Another utility of SPINS is that once the user defined casefile is successfully compiled, the problem parameters, grid information, boundary conditions, filter information, and timing information are saved in a configuration file that exists separately from the model itself. This file can be easily edited, transported between machines, and read into the model without having to recompile. It also provides a record of the simulations performed.

Figure 2.1 schematizes the usage of SPINS where the level of user interaction required to run the code increases from right to left. Some specific aspects of each section of SPINS are highlighted within each box. This figure is intended to be a very broad overview of SPINS.

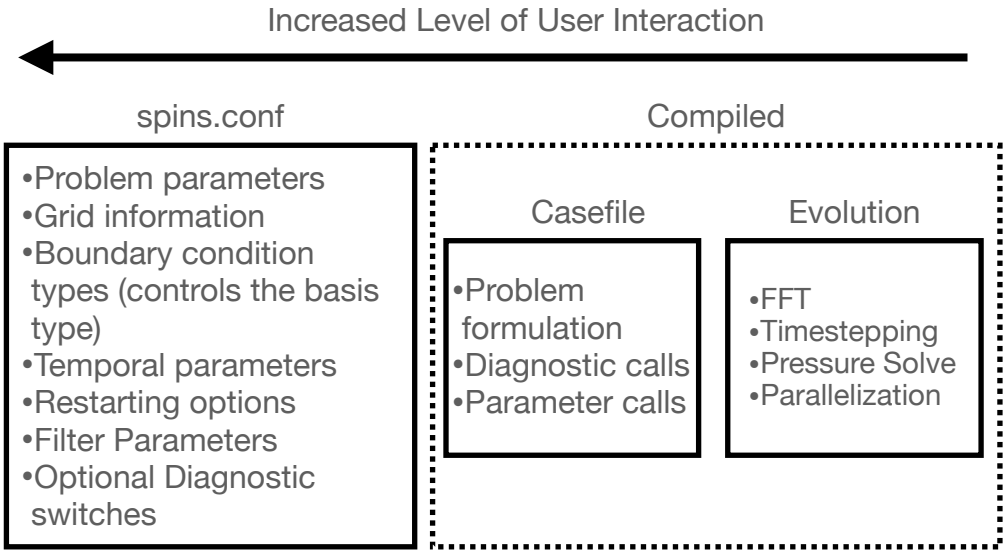

Figure 2.1: A schematization of the SPINS workflow. User interaction increases from right to left. For a given casefile, the `spins.conf` is the file with whom the user most often interfaces. Most importantly, this file contains the problem specific parameters that the user may wish to vary for a given experiment. The user may want to edit the case file, which is where the particular forcing and diagnostic information and code is kept. The case file should only be modified when planning a new experiment. Finally, the evolution code is mostly hidden from the user. This is where the actual solvers do their work.

2.4.2 Why pseudo-spectral methods?

When modelling some sort of physical process, our first decision is often in regards to what physical process or mechanism we want to focus our efforts on. Once we have made this decision, we need to understand the limitations of our modelling approach, and finally determine if those limitations are relevant to the dynamics, or if they can be ignored. In a perfect world the order of operations would be to formulate the modelling question, and then to choose a relevant model based on its strengths for studying the question at hand. In reality this order of operations is often reversed. The numerical model is chosen first, often due to factors such as model expertise, availability, and in some cases price–point. Next, the physical process which we would like to model is chosen. For this approach, it is imperative that we choose a process to study so that we can maximize the strengths of our chosen model while also minimizing the weaknesses. This was the approach used in this thesis. The model choice used in this thesis was primarily due to the modelling expertise available, and thereby directed the types of questions asked. Below, we highlight why pseudo-spectral models may be useful and what can be done to maximize their strengths.

The strengths of pseudo-spectral methods are immense for solving problems in specific contexts. For pseudo-spectral methods, solutions are expanded in terms of a certain basis. As an example, when boundary conditions are periodic on a certain interval, or can be periodically extended, we can express functions as a Fourier series (an infinite sum of sines, cosines, or complex exponential functions). In a numerical setting, the continuous interval is instead discretized, and this action forces our infinite Fourier series to become finite sum. Thus, to represent functions on the discretized grid, we require a discrete Fourier transform (DFT). In this thesis, sample points are typically uniformly spaced, which allows us to utilize the speed and accuracy of the Fast Fourier Transform (FFT) algorithm to compute DFTs. The FFT algorithm is incredibly efficient, undergoing $\mathcal{O}(N \log(N))$ flops in a single dimension with N points. Details of its implementation in SPINS can be found in Subich et al. (2013). Furthermore, when the geometry of a problem can be simplified, this leads to other potential simplifications in the parallelization scheme, further increasing efficiency. For an example, see the appendix in Deepwell (2018), which highlights the efficiency of the parallelization of SPINS simulations with uniform and clustered grids at various grid resolutions.

Furthermore, pseudo-spectral methods have little to no spurious numerical dissipation or dispersion in the absence of a filter. Other alternatives to spectral methods (finite volume methods or finite difference methods) suffer from significant and unpredictable numerical dissipation and dispersion, often caused by the choice of advection scheme. This can lead to artificially damped solutions and/or unphysical oscillation, and in some

cases, completely incorrect results. As an example, Vitousek and Fringer (2011) presented simulations of the evolution of internal solitary waves using a low order model in its non-hydrostatic configuration (allowing physical and numerical dispersion) and its hydrostatic configuration (allowing numerical dispersion only). They found that at low lepticity (ratio of the horizontal grid spacing to upper layer depth) in the hydrostatic configuration, numerical dispersion generated very short trailing waves that were eventually dissipated. The process of numerical dispersion followed by dissipation of the trailing waves caused a significant change in the propagation velocity and location of the leading solitary wave. In the non-hydrostatic configuration, the trailing solitary waves were instead generated by physical dispersion and converged to the correct length scale. Furthermore, they were not significantly damped by numerical or physical dissipation. By increasing the lepticity, the numerical dispersion in both the non-hydrostatic and the hydrostatic configurations lead to severe damping of the wave leading to indistinguishable results between the waves in each configuration.

Pseudo-spectral methods avoid spurious diffusion and dispersion, and instead control aliasing with the use of a numerical filter. The numerical filter applied in SPINS is an exponential filter and is discussed in detail in Deepwell (2018). In short, the exponential filter is a low-pass filter, where the amount of energy removed from the system is predictable. The user can specify a cutoff wavenumber k_c (in one dimension for simplicity), where every $k < k_c$ remains unaffected by the filter, but $k > k_c$ becomes attenuated. Hyper-viscosity is an alternative to a numerical filter, but is not used in this thesis. See Ulloa et al. (2019) for a recent example of the use of hyper-viscosity in dynamical studies in cold water.

Pseudo-spectral methods are not without their limitations. As discussed above, geometries must be simple so as the method is able to use the FFT algorithm. Other numerical schemes allow for arbitrary boundary conditions (like inflows for instance), whereas pseudo-spectral methods are relatively limited in the boundary condition choice. Freedom to arbitrarily specify boundary conditions often comes at the cost of accuracy and speed though. For the purposes of this thesis, these simple geometries and basic boundary conditions are sufficient to represent the processes we are interested in. A series of more directed discussions regarding the applicability of geometries and boundary conditions are found in each chapter.

Chapter 3

Numerical simulations of the three-dimensionalization of a shear flow in radiatively forced cold water below the density maximum

3.1 Author's Note

This chapter is a modification of the material that appeared Grace et al. (2022). The main changes include a complete non-dimensionalization of the equations of motion, as well as an extended discussion on the governing non-dimensional parameters. Figures are reported in terms of non-dimensional variables except for figures 3.2 and 3.5.

3.2 Introduction

During ice-covered seasons, and especially during the later winter, the primary mechanism responsible for introducing energy into the water column is solar radiation. Some of that radiation is reflected or absorbed by the ice, and some of it penetrates into the underlying water column, with its intensity decreasing approximately exponentially with depth. The rate at which the intensity of the radiation is attenuated with depth is encoded in an attenuation length scale that is a function of both the clarity of the water and the wavelength

of the incident radiation. Smaller attenuation lengths represent more absorption near the ice-water interface, and larger attenuation lengths represent penetration to greater depths.

Owing to the fact that freshwater temperatures beneath ice are typically below T_{md}, the added heat that increases the temperature of the water also increases its density. Since the bulk of the heat is added near the surface, solar radiation ultimately leads to the formation of an unstable stratification that induces overturning and subsequent homogenization of the water column. As mentioned previously, Yang et al. (2017) used thermistor chain data in Lake Simcoe, Canada, over the winter in 2015 to show homogenization of the water column due to overturning once the snow on the ice surface had melted. Their figure is reproduced in figure 3.1. This figure shows that the time the surface snow melts (approximately April 1 in panel (b)) coincides with an increased intensity of solar radiation entering the water column (inferred from the daily-averaged time rate of change of the water column temperature integrated over the column) (panel (d)) and homogenization of the water column (panel (c)). Prior to this time, when ice and snow cover limited the incoming solar radiation, the dominant heat flux came from bottom sediments. This is the usual indicator of Winter I. Winter II occurs when the sediments have released all of their heat and snow cover melts allowing solar radiation to penetrate the water column (Kirillin et al., 2012).

This result provides practical evidence of total homogenization by convection driven by solar radiation. Part of the unique nature of the cold water regime is that characteristic density differences ($\Delta\rho = \rho_1 - \rho_2$) within the flow can be very small. The density differences within a flow are usually characterized by the Atwood number, $\mathrm{At} = (\rho_1 - \rho_2)/(\rho_1 + \rho_2)$ (Andrews and Dalziel, 2010). There has been some interest in mixing in small At flows. Boffetta et al. (2009, 2010); Andrews and Dalziel (2010) and Akula et al. (2013) quote At in the range of $\mathcal{O}(0.01) - \mathcal{O}(0.1)$ but it can be much smaller in other applications. Temperature and density differences within the flows examined in this chapter are small. For example, based on the initial and final states considered, At is in the range of $\mathcal{O}(10^{-5})$.

The process of overturning generated by solar radiation is complicated by the presence of subsurface currents. For instance, there is evidence of very slow (several mm/s) subsurface currents beneath ice cover in Lake Vendyurskoe (Russia) (Malm et al., 1998), induced by a uni-modal seiche. More vigorous subsurface (several cm/s) currents can occur as a result of under ice river plumes as well. In simulations of an under-ice river plume, Kasper and Weingartner (2015) showed that velocities were in the range of 5-10 cm/s beneath ice cover. The discharge that they used was representative of the spring freshet of a small arctic river. This order of magnitude agrees with measurements of the flows beneath landfast ice in the Alaskan Beaufort Sea by Weingartner et al. (2017). There is considerable theoretical evidence showing that the development of the convective instabilities is coupled to the shear generated by flows like those beneath ice cover. Benilov et al. (2002) used a

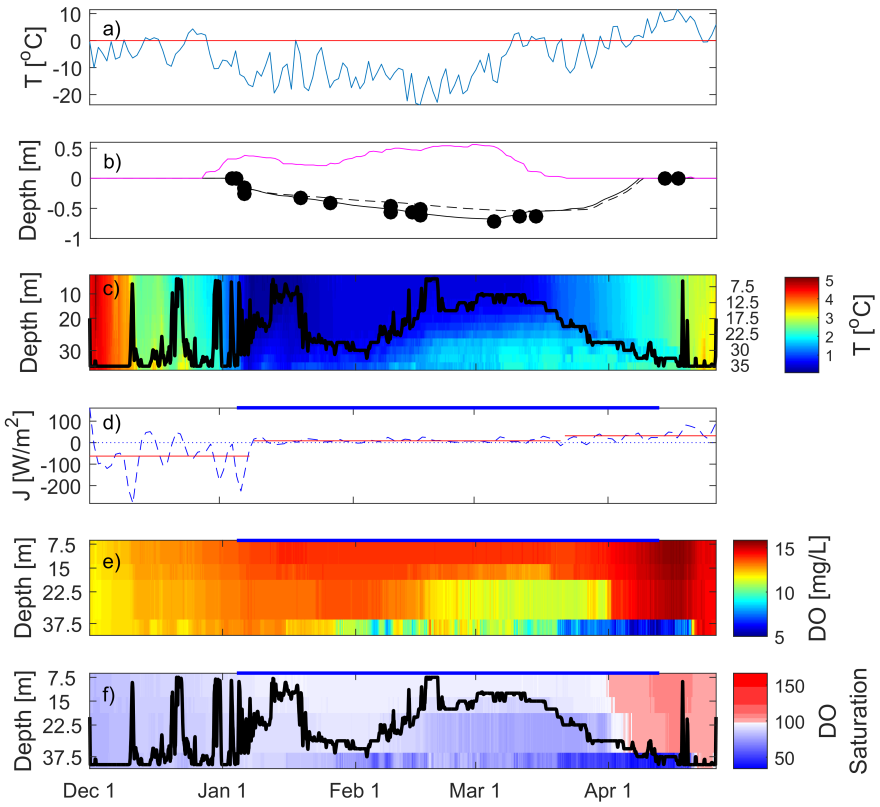

Figure 3.1: Time series of (a) ERA-Interim temperature (a climate reanalysis data set covering 1979 to August 2019). (b) Predictions of ice thickness from the Canadian Lake ice model without snow (solid black line) and with snow (dashed black line), as well as observations of ice thickness (black markers) and snow cover (pink line). A positive depth indicates height above the surface. (c) Water column temperature profiles at the measured levels at K42 (a sensor location) and the estimated mixed layer (black line). (d) Daily average heat flux time series. Red lines indicate the mean over three periods: Before ice cover J = -62.5 W/m^2, Winter I when J = $+8.4$ W/m^2, and Winter II when J = $+31.8$W/m^2. Blue dash line indicates zero. (e) Dissolved oxygen concentrations at K42. (f) Percentage of dissolved oxygen saturation and the estimated mixed layer (black line). The thick blue line above Figures 2d–2f indicates the duration of ice cover from 8 January until 18 April. Figure adapted with permission from Yang et al. (2017).

jet velocity profile and a quasi-two layer inverse stratification to show that near the tip of the jet (where the vertical shear is near zero), Rayleigh-Taylor instabilities (RTI) occurred, but on the flanks of the jet (where the vertical shear is changing with depth), no RTI were noted. The authors followed this with a numerical study that showed that by increasing the magnitude of homogeneous shear, the width of the unstable region in spectral space decreased but stayed finite. Furthermore, the growth rates always had an interior peak, indicating that there is always a single fastest growing instability. Their conclusion was that streamwise instabilities will always occur in their system and the length scale of the primary instability is proportional to the magnitude of the shear in some way. Mikhailenko et al. (2005) went a step further and showed that streamwise RTI are suppressed in regions where

$$|\tilde{U}_z| \geq \frac{\tilde{\sigma}_i}{\sqrt{2}}. \tag{3.1}$$

Here, $|\tilde{U}_z|$ is the local magnitude of the shear, and $\tilde{\sigma}_i$ is the growth rate of the fastest growing instability in the absence of any background shear. While the result of Mikhailenko et al. (2005) is mathematically sound, the theory does not include a spanwise dimension. Multiple studies in varying convection contexts have shown that shear interacting with an unstable stratification in three dimensions leads to rollers with their cores aligned with the background current. Kuo (1963) commented that cloud streets occur because of the suppression of streamwise instability, leaving spanwise perturbations to grow. Keisuke et al. (1991) noted that the interaction between Rayleigh-Bénard convection and shear in their experiments on coherent turbulent structures led to the formation of rollers. Finally, Pirozzoli et al. (2017) showed these rollers in a similar setup using numerical simulations for a variety of Reynolds numbers and Rayleigh numbers. To our knowledge, no numerical studies on cold water convection induced by volumetric thermal forcing interacting with shear have been carried out.

In this chapter, we study the interaction between a shear flow and convection induced by non-uniform heating in cold water. Heat is continually added such that an unstable density gradient is created near the surface giving rise to convective instabilities. We investigate the development of the instabilities and the transition to turbulence using high resolution three dimensional simulations. We discuss with examples the roles that the magnitude of the shear and the attenuation length scale play in the transition to turbulence. In this chapter, the word "turbulence" is used to describe the random and chaotic flow state, and is used in the qualitative sense. A directed discussion on the turbulent state will be pursued in future work.

The structure of the chapter is as follows. First we describe the experimental configuration and some particular aspects of the numerical model. Next, we show the equations of

motion and describe the setup we are modelling. Following this is a non-dimensionalization of the equations of motion and a discussion of the governing non-dimensional numbers. Then we show the results of several numerical simulations highlighting the instability development and the transition to turbulence. The last section provides a summary and discussion of the results, as well as a description of the limitations of simulating this system in two dimensions. We conclude with future research directions.

3.3 Experimental Configuration

The study presented in this chapter is motivated by under-ice dynamics as a result of heat deposition in lacustrine bodies over the winter. In a complete lacustrine system, many competing mechanisms and processes must be included to properly represent the full range of dynamics. However, the specific modelling choices presented herein are meant to represent experimental scales, thus maximizing the capabilities of our numerical model (discussed in chapter two). Pursuant to this, the conceptual model presented below is simplified in order to have a properly constrained study.

In this study we use the pseudospectral numerical model SPINS (Subich et al., 2013) to perform direct numerical simulations of the incompressible Navier-Stokes equations under the Boussinesq approximation to model the interaction between cold water (temperatures between 0°C and the freshwater temperature of maximum density) convection generated by volumetric thermal forcing and a shear current in a rectangular domain of length and width L (ranges from 1.024m to 2.048m) and depth H (2.048m). We adopt the standard oceanographic coordinate system so that the streamwise (direction of the shear current), spanwise, and vertical (positive upwards) directions are denoted by (x, y, z) respectively and corresponding unit vectors $\hat{\boldsymbol{i}}$, $\hat{\boldsymbol{j}}$, and $\hat{\boldsymbol{k}}$, and $z = 0$ is along the bottom of the domain. The boundary conditions for the top and bottom surfaces are free-slip for velocity and no-flux for temperature, while the boundary conditions are periodic in the horizontal directions. The uniform grid spacing is $(\Delta x, \Delta y, \Delta z) = (4 \times 10^{-3}, 4 \times 10^{-3}, 2 \times 10^{-3})$m. A resolution sensitivity test was performed on the Slow-Narrow case (table 3.2) and revealed that the instability development was insensitive to higher resolutions, thus, the resolution was selected to balance accuracy and expediency of simulation. A domain size test was also performed and the domain size presented herein is sufficient to resolve the scales of interest. Static parameter information is found in table 3.1. Where relevant, the value is directly referenced, otherwise the location in the text is referenced. The values of parameters that are varied for each case are included in table 3.2.

In the simulations in this study, the temperature is an initially uniform value of T_0

(table 3.1), chosen to be less than the temperature of maximum density for freshwater, T_{md}. The choice of a uniform temperature is made to simplify the modelling approach. Ulloa et al. (2019) and Ramón et al. (2021) observed a cross-shore shear flow within the convective mixed layer in their simulations indicating some numerical evidence for the coexistence of a shear flow in a uniform temperature environment (more on this in section 3.4).

The dimensional equations of motion that are solved by the model are

$$\frac{D\tilde{\boldsymbol{u}}}{D\tilde{t}} = -\nabla\tilde{p} - g\rho\hat{\boldsymbol{k}} + \nu\nabla^2\tilde{\boldsymbol{u}}, \tag{3.2}$$

$$\frac{D\tilde{T}}{D\tilde{t}} = \kappa\nabla^2\tilde{T} + \tilde{F}(\tilde{z}), \tag{3.3}$$

$$\nabla\cdot\tilde{\boldsymbol{u}} = 0. \tag{3.4}$$

In this chapter, dimensional variables contain a tilde, while non-dimensional ones do not. Dimensional parameters (such as physical constants) do not have tildes. The material derivative is represented by $\frac{D}{D\tilde{t}} = \frac{\partial}{\partial\tilde{t}} + \tilde{\boldsymbol{u}}\cdot\nabla$, the three dimensional velocity is given by $\tilde{\boldsymbol{u}}$, time is given by $\tilde{t}$, pressure divided by the reference density ρ_0 is given by $\tilde{p}$. Viscosity is given by ν, the temperature diffusivity by κ, and g is the gravitational acceleration, values of which are found in table 3.1. ρ is the density perturbation about the reference density ρ_{md}, about 999.97 kg/m^3. Note that the reference density has been absorbed into both $\tilde{p}$ and rho. This gives p units of m^2/s^2, and leaves ρ unitless (hence there is no tilde). The nonlinear equation of state used in this chapter is

$$\rho = -C(\tilde{T} - T_{md})^2 \tag{3.5}$$

where $\tilde{T}(x, y, z, t)$ is the temperature field, and the value of the constant C is given in table 3.1.

The volumetric heating is represented by $\tilde{F}(\tilde{z})$ [°C/s] with an example profile shown in figure 3.2(b). This profile is a simple model of penetrative short wave radiation. The forcing takes the form of an exponential with a single decay scale and is called the Beer-Lambert Law. Mathematically, it is given by

$$\tilde{F}(\tilde{z}) = \frac{Q_0}{\ell}\exp\left(\frac{\tilde{z} - H}{\ell}\right), \tag{3.6}$$

where H is the total depth of the domain, and $\tilde{z} = 0$ along the bottom of the domain. Two important parameters appear in this formulation of the forcing. They are Q_0 (dimensions

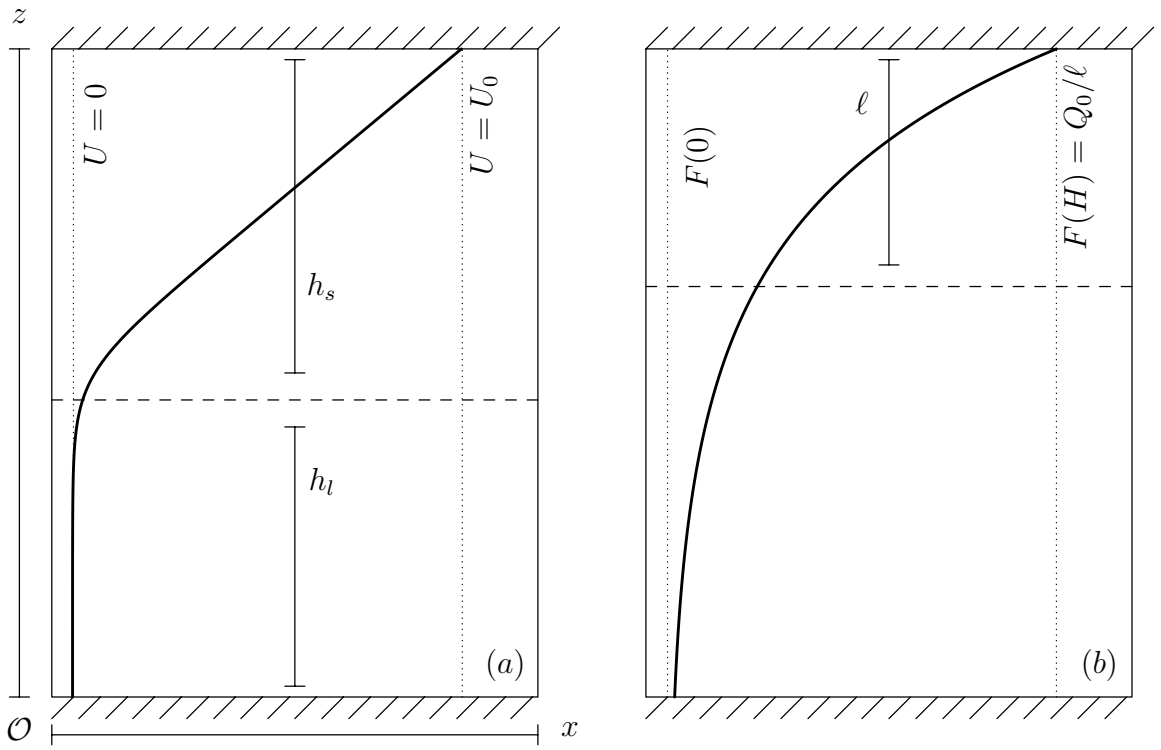

Figure 3.2: Panel (a) shows the background velocity profile from equation (3.8). The maximum upper layer velocity is U_0. The upper layer depth is h_s, and the lower layer depth is h_l. The thermal forcing profile is shown in panel (b). The decay scale of the thermal forcing is ℓ, and the magnitude at the surface is Q_0. One e-folding scale is located at a height $H - \ell$.

of (°C m/s), the magnitude of the thermal forcing at the top of the domain, and ℓ, the attenuation length. The value for Q_0 used throughout the chapter is found in table 3.1, and corresponds to an intensity of approximately 30 W/m^2 when multiplied by $\rho_0 C_p$. This value is an order of magnitude estimate for the intensity of radiation that penetrates beneath a representative amount of snow and ice cover on a natural body of water in the late winter (Kirillin et al., 2012; Ulloa et al., 2019). $Q_0/\rho_0 C_p$ represents the total heat flux into the body of water. The exponential envelope describes how much of that heat is absorbed by the water column at a specific depth. Since changes of temperature are functions of the divergence of the heat flux (see (2.26) for instance), a factor of $1/\ell$ appears (ℓ is discussed below).

The attenuation length ℓ is provided in table 3.2 for each case. The attenuation length controls how fast the incoming radiation is attenuated with depth and is a function of both the water's clarity and the frequency band of the incident radiation. The Jerlov water-type system presents a basis for categorizing water based on its clarity and assigns attenuation length scales based on how certain frequency bands of light are absorbed for a given turbidity (Jerlov, 1976). Common parametrizations of penetrative shortwave radiation often contain more than one forcing component, each with its own associated attenuation length. Including multiple frequency bands may be necessary to adequately represent mechanisms such as photosynthesis, gas dynamics, or stratification development (Simpson and Dickey, 1981a; Hodges and Dallimore, 2006). For reference, other established codes like the MITgcm (Campin et al., 2019), and ELCOM (Hodges and Dallimore, 2006) use two and three band models respectively in their default setups. The columnar model used in Simpson and Dickey (1981a) and Simpson and Dickey (1981b) used up to 10 bands for some experiments.

Since this study is not concerned with the precise distribution of heat by the solar radiation, and is instead concerned with the redistribution of heat by instabilities generated by the unstable stratification, we follow the approach of Ulloa et al. (2019) and Bouffard and Wüest (2019) and parameterize the incident radiation as a single-band model. In the context of cold water, Bouffard and Wüest (2019) simplified the Jerlov system and made an order of magnitude estimate that attenuation length for clear water beneath ice is $\mathcal{O}(1\text{m})$ and for turbid water beneath ice is $\mathcal{O}(0.1\text{m})$. The values for ℓ chosen for each case (table 3.2) were chosen to be similar in magnitude to the attenuation length used in Ulloa et al. (2019), who used $\ell = 0.4$m. For cases where ℓ was changed from the value in the Base case, the values were chosen such that there were clear differences in dynamics but was also in the neighborhood of the turbid estimate from Bouffard and Wüest (2019).

Since heat is continuously added to the domain, the domain averaged temperature will continue to increase as there is no explicit mechanism to remove it. By integrating equation

(3.3) over the entire domain, the domain averaged temperature becomes

$$\bar{T}(t) = T_0 + \frac{Q_0}{H}\left(1 - e^{-H/\ell}\right)\tilde{t}. \tag{3.7}$$

Thus, the average temperature of the domain increases at a rate $Q_0\left(1 - e^{-H/\ell}\right)/H$. The utility of defining $\bar{T}$ comes when we will non-dimensionalize the system in section 3.5.

In all cases, we should expect convective instabilities to grow at a rate proportional to two quantities: i) the density difference between consecutive fluid layers, often quantified by the Atwood number (see section 3.2), and ii) how much energy is initially present in each wavenumber. The initial energy in each wavenumber is controlled by the size of the initial white noise perturbation. Each simulation presented is seeded with a velocity perturbation of $u_{pert} = 10^{-6}$ m/s, the magnitude of which is held constant across all cases.

The initial velocity profile (current will be used interchangeably) considered for this chapter has a layer of constant shear atop a layer with no background velocity. Measurements of the velocity profiles in the near-mouth region of small river plumes (Osadchiev et al., 2020) indicate nearly piece-wise linear velocity profiles. The form of the current used in this chapter is given by

$$\tilde{U}(\tilde{z}) = \frac{U_0}{H}\int_0^{\tilde{z}} \left(1 + \tanh\left(\frac{\tilde{z}' - \frac{1}{2}H}{\delta}\right)\right) \mathrm{d}\tilde{z}', \tag{3.8}$$

and is shown schematically in figure 3.2(a). Here, δ controls how rapidly the profile transitions from motionless to the constant shear state. This parameter is held constant across all simulations at 0.1 m (table 3.1). Values for H and U_0 (the depth of the domain and maximum velocity of the current) are found in tables 3.1 and 3.2 respectively. A key feature of the profile in equation (3.8) is that it initially precludes the formation of shear instabilities by Rayleigh's inflection point criterion (Kundu, 1990). Shear instabilities provide a means for column wide mixing but are not of interest here.

Parameter	Description	Value	Dimensions
Q_0	Intensity of Solar Radiation	7.25×10^{-6}	°Cm/s
$\bar{T}$	Time varying domain averaged temperature	See equation 3.7	°C
ℓ	Attenuation length of solar radiation	See table 3.2	m
ν	Kinematic Viscosity	10^{-6}	m^2/s
κ	Thermal Diffusivity	10^{-7}	m^2/s
g	Gravitational Acceleration	9.81	m/s^2
C	Non-linear equation of state parameter	7.6×10^{-6}	$°C^{-2}$
T_{md}	Temperature of maximum density	3.98	°C
L	Domain width	See table 3.2	m
H	Domain depth	2.048	m
U_0	Background current velocity	See table 3.2	m/s
δ	Background current transition thickness	0.1	m

Table 3.1: List of dimensional parameters, a description, their value, and their dimensions.

Case	U_0 (m/s)	L (m)	ℓ (m)	$N_x \times N_y \times N_z$ –
Base	0	1.024	0.6	$256 \times 256 \times 1024$
Slow	0.001	1.024	0.6	$256 \times 256 \times 1024$
Fast	0.01	1.024	0.6	$256 \times 256 \times 1024$
Fast-Wide	0.01	2.048	0.6	$512 \times 512 \times 1024$
Fast-Narrow	0.01	0.512	0.6	$128 \times 128 \times 1024$
Medium-Attenuation	0.01	1.024	0.4	$256 \times 256 \times 1024$
Short-Attenuation	0.01	1.024	0.2	$256 \times 256 \times 1024$
Short-Attenuation-Wide	0.01	2.048	0.2	$512 \times 512 \times 1024$

Table 3.2: The cases considered in this chapter. U_0 is the maximum velocity of the background current, L is the streamwise length of the tank (equal to the spanwise length of the tank for all cases), ℓ is the attenuation length of the thermal forcing, and $N_x \times N_y \times N_z$ is the grid resolution.

3.4 Non-dimensionalization

In order to non-dimensionalize the system, we must use the parameters in table 3.1 to form a pressure scale $\mathcal{P}$, a velocity scale $\mathcal{U}$, a timescale $\mathcal{T}$, and a temperature scale θ.

Furthermore, we can use the Buckingham Pi theorem to rigorously identify the number of non-dimensional groupings that govern the system, and we can use our knowledge of the equations of motion to actually develop these non-dimensional groupings.

We can begin by decomposing the total temperature $\tilde{T}$ into a sum of $\bar{T}$ (the time-varying domain averaged temperature from (3.7)) plus the perturbation about this quantity, T_p, written as

$$\tilde{T} = \bar{T} + \tilde{T}_p. \tag{3.9}$$

By decomposing the temperature this way, we can define the temperature scale θ such that it characterizes only the perturbation about the background, and does not contain any information about the known time-varying average background state. Additionally, if the rate of heating is slow compared to other timescales of the problem, like the instability growth rate for example, the initial temperature of the domain T_0 can be used for scaling rather than $\bar{T}$ without accruing significant error. Substituting the temperature decomposition into (3.5) and expanding, we get

$$\rho = -C\tilde{T}_p^2 + 2C\tilde{T}_p(T_{md} - \bar{T}) + \rho\left(\bar{T}\right) \tag{3.10}$$

where

$$\rho\left(\bar{T}\right) = -C(\bar{T} - T_{md})^2$$

can simplify (3.10) to

$$\rho - \rho\left(\bar{T}\right) = -C\tilde{T}_p^2 + 2C\tilde{T}_p\Delta T, \tag{3.11}$$

where we have let $\Delta T = T_{md} - \bar{T}$, a parameter indicating the temperature difference between the temperature of maximum density and the domain averaged temperature. The second term on the left hand side of (3.11) is the density of the domain averaged temperature, which in general is not the domain averaged density. This term is balanced by a time-varying hydrostatic pressure and does not contribute to internal motion. We can let the total pressure be decomposed as $\tilde{p} = \bar{p} + \tilde{p}_v$, where $\bar{p}$ is in hydrostatic balance with $\rho\left(\bar{T}\right)$ so that

$$\frac{\partial \bar{p}}{\partial z} = -g\rho\left(\bar{T}\right), \tag{3.12}$$

and $\tilde{p}_v$ is the variation about this pressure. The above procedure has allowed us to simplify the equations of motion so as to be able to non-dimensionalize them. The equations of

motion are rewritten below for convenience.

$$\frac{D\tilde{\boldsymbol{u}}}{D\tilde{t}} = -\nabla\tilde{p}_v + Cg\tilde{T}_p^2 - 2Cg\tilde{T}_p\Delta T + \nu\nabla^2\tilde{\boldsymbol{u}} \tag{3.13}$$

$$\frac{D\tilde{T}}{D\tilde{t}} = \kappa\nabla^2\tilde{T} + \frac{Q_0}{\ell}\exp\left(\frac{\tilde{z}-H}{\ell}\right) \tag{3.14}$$

$$\nabla\cdot\tilde{\boldsymbol{u}} = 0 \tag{3.15}$$

The equations presented above are expressed in terms of only three basic dimensional quantities: time, length, and temperature. For the shear-free cases, there are 10 dimensional parameters that govern the system, and for the sheared cases, there are 12. The two extra parameters for the sheared cases arise from the initial condition, $\tilde{U}(\tilde{z})$. The complete list of parameters are shown in table 3.1, as well as a short description of each. As we shall see in the next section, two parameters within this list are dependant on others, thereby reducing the number of independent parameters to eight for the shear-free cases and 10 for the sheared cases. With this in mind, the Buckingham Pi theorem gives five non-dimensional groupings for the shear-free cases, and seven for the sheared cases.

In the following section, the non-dimensionalization will be carried out in detail for both the shear-free and sheared cases, highlighting the significance that each non-dimensional parameter has for the problem, along with some examples of where they have been used elsewhere.

3.5 Scaling for the Shear-Free System

In the shear free cases, there is no inherent velocity $\mathcal{U}$, or temperature scale θ. Thus, these scales must be functions of the problem parameters defined in table 3.1. We can choose the following scalings for the dependant variables:

$$\tilde{\boldsymbol{x}} = \ell\boldsymbol{x} \tag{3.16}$$

$$\tilde{\boldsymbol{u}} = \mathcal{U}\boldsymbol{u} \tag{3.17}$$

$$\tilde{t} = \frac{\ell}{\mathcal{U}}t \tag{3.18}$$

$$\tilde{p}_v = \mathcal{U}^2 p \tag{3.19}$$

$$\tilde{T} = \theta T + \bar{T}, \tag{3.20}$$

We have chosen the attenuation length ℓ to be the relevant length scale for the problem, allowing us to define the timescale $\mathcal{T} = \ell/\mathcal{U}$. We have chosen the advective timescale

because we are assuming that the density driven fluid motion is responsible for moving heat around the domain, rather than diffusion. We could use the total depth H as the characteristic depth, but as will be seen later, in the limit of $\ell/H \to 0$, (a very deep domain) the instabilities do not "feel" the bottom, and grow independently of this parameter. More on this in section 3.5.3. The pressure is scaled by $\mathcal{U}^2$, and finally, we have let $\tilde{T}_p = \theta T$ so the total temperature scales as $\theta T + \bar{T}$.

There are two minimum requirements that the velocity, time, pressure, and temperature scalings must satisfy in order to be useful.

1. The scales must have some functional dependence on the parameters relevant to the thermal forcing; Q_0 and ℓ. For the shear free cases, all motion is induced by spatial density differences within the flow which are induced by the thermal forcing.

2. The non-linear equation of state should play some role in determining how the motion scales. As characteristic temperatures approach the temperature of maximum density, the slope of the equation of state becomes very small effectively slowing motion by decreasing velocities.

We can start by non-dimensionalizing (3.13). Substituting in the above scalings, we arrive at

$$\frac{\mathcal{U}^2}{\ell}\frac{D\boldsymbol{u}}{Dt} = -\frac{\mathcal{U}^2}{\ell}\nabla p + Cg\theta^2 T^2 - (2Cg\theta\Delta T)T + \frac{\nu\mathcal{U}}{\ell^2}\nabla^2\boldsymbol{u}. \tag{3.21}$$

For clarity, we can re-write the above equation with the buoyancy term re-arranged:

$$\frac{\mathcal{U}^2}{\ell}\frac{D\boldsymbol{u}}{Dt} = -\frac{\mathcal{U}^2}{\ell}\nabla p - (2Cg\theta\Delta T)T\left(1 - \frac{\theta}{2\Delta T}T\right) + \frac{\nu\mathcal{U}}{\ell^2}\nabla^2\boldsymbol{u}. \tag{3.22}$$

We can see here that the parameters Cg and $\Delta T = T_{md} - \bar{T}$ always appear in the equations as single parameters. Letting

$$\mathcal{U} = \sqrt{2Cg\theta\Delta T\ell} \tag{3.23}$$

allows us to divide out the $\mathcal{U}^2/\ell$ term, revealing the following non-dimensional equation:

$$\frac{D\boldsymbol{u}}{Dt} = -\nabla p - T\left(1 - \frac{\Theta}{2}T\right) + \frac{1}{\sqrt{\mathrm{Gr}}}\nabla^2\boldsymbol{u}. \tag{3.24}$$

where we have defined the NLEOS parameter Θ as

$$\Theta = \frac{\theta}{\Delta T} \tag{3.25}$$

and the Grashof number as

$$\mathrm{Gr} = \left(\frac{\mathcal{U}\ell}{\nu}\right)^2. \tag{3.26}$$

$\mathcal{U}$ is sometimes called the buoyancy velocity scale, and arises because of the assumption that motion is driven exclusively by the density differences within the flow. In the current context, $\mathcal{U}$ is a function of two temperature scales: θ and ΔT. Each one of these temperature scales satisfies the requirements listed above; θ captures the dependence on the temperature differences set by the thermal forcing, while ΔT captures the dependence on proximity of the characteristic temperatures to T_{md}, and thus the variable slope of the NLEOS. Previous studies of similar setups, Bouillaut et al. (2019) for instance, have defined the buoyancy velocity using a linear equation of state (no variation in the slope of the NLEOS), which leads to a buoyancy velocity that is only a function of the internal temperature differences (θ in the framework presented in this chapter).

We can find a closed form expression for θ in order to determine closed form expressions for $\mathcal{U}$ and $\mathcal{T}$. To do this, we need to non-dimensionalize (3.14). Using the scalings in equations (3.17)-(3.20), non-dimensionalizing equation (3.14) gives

$$\frac{\theta}{\mathcal{T}}\frac{DT}{Dt} + \frac{d\bar{T}}{d\tilde{t}} = \frac{\kappa\theta}{\ell^2}\nabla^2 T + \frac{Q_0}{\ell}\exp\left(\frac{z-H}{\ell}\right). \tag{3.27}$$

We can let

$$\frac{d\bar{T}}{d\tilde{t}} = \frac{Q_0}{H}\left(1 - e^{-H/\ell}\right), \tag{3.28}$$

and simplifying the above set gives us

$$\frac{DT}{Dt} = \frac{1}{\sqrt{\mathrm{GrPr}^2}}\nabla^2 T + \frac{Q_0}{\mathcal{U}\theta}\left(\exp\left(\frac{z-H}{\ell}\right) - \frac{\ell}{H}\left(1 - e^{-H/\ell}\right)\right). \tag{3.29}$$

From the above, we can identify several non-dimensional parameters. The first is the Prandtl number

$$\mathrm{Pr} = \frac{\nu}{\kappa}, \tag{3.30}$$

which measures the relative strength of momentum diffusion to temperature diffusion. The next is the non-dimensional depth

$$\mu_1 = \frac{H}{\ell}. \tag{3.31}$$

which will be discussed in detail later. The last non-dimensional grouping is $Q_0/\mathcal{U}\theta$, and represents the ratio of the the heat flux by volumetric forcing (Q_0), to the convective heat

flux scale ($\mathcal{U}\theta$). To estimate θ, we will assume that these two scales are approximately equal. In general, this is not true until the system is at equilibrium, but this still provides a consistent yardstick on which we can base the case intercomparisons in the chapter. Additionally, the initial temperature changes of the system are driven almost exclusively by the volumetric thermal forcing (the last term on the right hand side of in (3.29)) rather than thermal diffusion, so we set $Q_0/\mathcal{U}\theta = 1$ allowing us to define θ as:

$$\theta = \left(\frac{Q_0^2}{Cg\ell\Delta T}\right)^{1/3}. \tag{3.32}$$

Importantly, the temperature scale is not linearly related to any of the problem parameters. The temperature scale is proportional to $Q_0^{2/3}$ indicating that the radiation intensity would have to increase by almost three times in order to double the temperature scale (all other parameters held constant). Furthermore the temperature scales with both $\ell^{-1/3}$ and $\Delta T^{-1/3}$, meaning that in order to double the temperature scale, the attenuation length or the bulk temperature difference needs to be decreased by almost 10 times. Understanding this will become important when discussing whether or not we might see similar dynamics at the field scale.

With the temperature scale in hand, the timescale, velocity scale, and the pressure scale become:

$$\mathcal{U} = (2Cg\ell\Delta TQ_0)^{1/3}, \quad \mathcal{T} = \left(\frac{\ell^2}{Cg\Delta TQ_0}\right)^{1/3} \tag{3.33}$$

In this framework, both the velocity scale and the timescale vary proportionally to a sub-linear power of the attenuation length, indicating that doubling the attenuation length does not double to velocity and timescales. Additionally, the velocity scale is proportional to a sub-linear power of the intensity of the radiation, and the timescale is inversely proportional to it. This is consistent with the fact that more energy input by the thermal forcing increases the flow speeds as there is more potential energy that can be changed to kinetic energy by buoyancy production.

Finally, the five parameters that govern the shear-free system are as follows:

$$\Theta = \frac{\theta}{\Delta T}, \quad \mathrm{Gr} = \left(\frac{\mathcal{U}\ell}{\nu}\right)^2, \quad \mu_1 = \frac{H}{\ell}, \quad \mathrm{Pr} = \frac{\nu}{\kappa}, \quad \mu_2 = \frac{L}{\ell}. \tag{3.34}$$

In order, they are the NLEOS parameter, the Grashof number, the dimensionless depth, the Prandtl number, and the aspect ratio. Each of these will be described below.

3.5.1 The NLEOS parameter

The NLEOS parameter,

$$\Theta = \frac{\theta}{T_{md} - \bar{T}}, \tag{3.35}$$

is the ratio of the temperature scale induced by the thermal forcing to the difference between the mean temperature difference and the temperature of maximum density. Θ controls when the non-linear term of the NLEOS will be of comparable magnitude to the linear one, indicating when we should expect the non-linear term to play a meaningful role in the governing equations. In the cases presented in this chapter, $\Theta \sim \mathcal{O}(10^{-5})$, so the non-linear terms in the NLEOS can be ignored. However, it is useful to briefly discuss what one might see when the non-linear terms play a meaningful role in this system. In convection and convection related contexts, NLEOS effects are often characterized by asymmetric plume growth, resulting in larger downward excursions by plumes compared to excursions by upward growing plumes. Olsthoorn et al. (2019) discussed the development of diffuse interface Rayleigh-Taylor instabilities using the NLEOS. They compared the growth of instabilities originating at the mid-depth of their domain and showed that under a linear EOS, the upward and downward growing plumes were symmetric, while under the NLEOS, the downward growing plumes grew faster than those growing upwards. Another example is from the study of Ozgökmen and Esenkov (1998), who noted that falling salt fingers grew faster than rising ones as they increased their non-dimensional non-linearity parameter (equivalent to Θ in this thesis) up to 1. When they increased it to 3, rising plumes did not appear to form. More discussion on NLEOS effects can be found in chapters four and five.

It is also useful to discuss under what circumstances might we be able to achieve $\Theta \sim 1$ in a similar laboratory or field setup. In terms of a field campaign or a laboratory experiment, three parameters in the definition for Θ can be realistically varied. They are Q_0, ℓ, and ΔT. Kantha and Clayson (2000) provides a resource of measurements from a multitude of studies that highlight the physical limitations of values of ℓ and Q_0 when considering laucustrine bodies of water. The attenuation length of incident radiation in the field varies over about 5-6 orders of magnitude depending the frequency of the incoming radiation. For example, infrared radiation (775-2600 nm) has an attenuation length on the order of 0.1mm to 10 cm and is typically independent of the turbidity of the water. The attenuation lengths in the UV (300-345 nm) and visible spectra (350-750 nm) are both functions of the clarity of the water. The attenuation length for the UV spectrum in optically clear water can vary between about 5-10m (for turbid water, the attenuation length is reduced by about an order of magnitude), and for the visible spectrum between about 50cm and 50 m. Since $\theta \sim \ell^{-1/3}$, smaller attenuation lengths lead

to larger temperature scales, so it may be difficult to achieve $\Theta \sim 1$ via the manipulation of ℓ unless it could be adequately constrained. Thus, in an experimental setting where band-limiting the incident radiation is potentially possible, one could achieve non-linear effects by using exclusively infrared light to drive instabilities. Achieving non-linear effects in the field may be tougher to measure as the incoming frequency is not band limited, and attenuation lengths are typically very large.

Another potential method of controlling the attenuation length is by the use of artificial dyes. This technique was used in the studies in Lepot et al. (2018) and Bouillaut et al. (2019). More information is presented in section 3.5.3. Furthermore, Q_0 can only achieve a maximum of about 10^{-3} °Cm/s (corresponding to about 1000 W/m^2) in only the most optimal conditions in the field. In the wintertime, this maximum is further reduced for two reasons: 1) the reduced solar zenith angle and 2) intermediate ice and snow cover. Of course, in a laboratory setting, controlling the intensity of incident radiation is trivial. The last parameter that could potentially be manipulated is ΔT. In the field, to realistically achieve non-linear effects, ΔT must be very small, meaning characteristic *in situ* temperatures must be very near the temperature of maximum density. As an example, consider if $\Theta \sim 1$, then from (3.35), we would have to have

$$\Delta T = \left(\frac{Q_0^2}{Cg\ell} \right)^{1/4} . \tag{3.36}$$

For the realistic values of Q_0 and ℓ discussed above, ΔT has a corresponding range of about 10^{-4} to 10^{-1} °C. Of course, such small temperature differences in the field can easily be erased by other processes like surface wave–induced mixing, or even heat fluxes from surface ice. Furthermore, we run into the issue of actually measuring these temperature differences. For example, a well calibrated thermistor may only have the accuracy of ±0.01°C (Anonymous, 2018).

3.5.2 Grashof Number

The Grashof number is a measure of the relative strengths of buoyancy forcing and momentum diffusion and is a common non-dimensional parameter in a variety of density driven flow contexts (often the Rayleigh number is used to characterize this ratio, but it is interchangeable with the Grashof number for the purposes of this thesis). A common occurrence of the Grashof number is in the study of gravity currents, where it is used as a control parameter (Cantero et al., 2007, 2008; Härtel et al., 2000a), and indeed as a brief

look-ahead, the Grashof number is a controlling parameter for the systems described in chapters 4 and 5 in this thesis. Recall the Grashof number is defined as

$$\mathrm{Gr} = \left(\frac{\mathcal{U}\ell}{\nu}\right)^2. \tag{3.37}$$

In the framework of the current chapter, using the definition of θ in (3.32) and $\mathcal{U}$ in (3.33), the Grashof number above can be re-written in terms of the problem parameters as

$$\mathrm{Gr} = \frac{(Cg\Delta T Q_0)^{2/3}\ell^{8/3}}{\nu^2}. \tag{3.38}$$

An important feature here is that the exponent on ℓ is greater than one, indicating that there could potentially be a large discrepancy between lab scale Grashof numbers and field scale Grashof numbers. As discussed above, attenuation lengths in the field can range over several orders of magnitude, whereas in experimental or numerical settings, their isolated influence is limited by the geometry of the tank or numerical domain. In this chapter, the Grashof numbers are in the range of $\mathcal{O}(10^4) - \mathcal{O}(10^5)$. In the study of Ulloa et al. (2019), a range of Grashof numbers can be estimated over the course of about a month of simulation time using the parameters listed in their table A1 as well as the maximum and minimum mixed layer temperatures. Using this information, Grashof numbers in their study ranged between about 1.4×10^4 and 1.7×10^4. This narrow range is due to the small range of ΔT over the course of the month.

In general, Grahsof numbers can be much larger for summertime process than those for processes beneath ice. An important reason for this is because the characteristic velocity scales are often much smaller due to the less vigorous forcing that occurs over winter. As a comparison, consider another convection process, this time due to surface cooling in the summer. In temperate lakes in the summer, there is an outward heat flux at the surface of the lake (due to outgoing longwave radiation, sensible and latent heat fluxes). As heat escapes the surface of the body of water, near surface water becomes denser and sinks, generating convective cells. The typical rate of heat loss in the late summer at night can amount to approximately 200 W/m^2 at night (Bouffard and Wüest, 2019), whereas in the winter, a reasonable estimate of incident shortwave radiation is about 30 W/m^2 (the value used in this chapter). Since these heat fluxes are the driver of the convection, it is sensible that higher forcing in the summer would amount to more vigorous convection. As an example, consider the results of Jonas et al. (2003), who studied convection due to surface cooling in a small wind protected lake (Soppensee located on the Swiss Plateau). Their outgoing surface heat flux was a maximum of 200 W/m^2 and they found convective velocities w_* were on the order of 5-6 mm/s over a depth h of about 6 metres. We can use

this information to estimate a flow Reynolds number $\mathrm{Re}_f = w_* h/\nu$. Since they provide evidence that the total dissipation is dominated by dissipation in the bulk (as opposed to the surface boundary layer), we can relate the flow Reynolds number to the Grashof number through the scaling law $\mathrm{Gr} \sim \mathrm{Re}^2$ (Grossmann and Lohse, 2000). This gives $\mathrm{Gr} \sim 10^9$; a $4-5$ order of magnitude difference between the results presented in this chapter as well as the results of Ulloa et al. (2019).

3.5.3 Attenuation Length

In this study, μ_1 represents the non-dimensional depth of the domain and is written as

$$\mu_1 = \frac{H}{\ell}. \tag{3.39}$$

A different interpretation of this parameter was studied in a context similar to the one presented here. Lepot et al. (2018) established a technique for generating volumetrically forced convection in a laboratory. In their experiments, the heat was generated by placing an intense light source at the bottom of a tank of water. The light shined on the tank and generated an inverse stratification, and the attenuation of the heating was controlled by the concentration of an added dye. This differed from other experiments of convection where plates on the bottom and top of the domain were heated and cooled and heat from the plate would have to diffuse across a thermal boundary layer. The goal of this study was to show that this method of internally heating the bulk fluid is a mechanism to achieve the so-called "ultimate regime of convection". In this regime, the Nusselt number (the non-dimensional vertical heat flux) scales with $\mathrm{Ra}^{1/2}$, where Ra is the Rayleigh number. This is different than the classical scaling of $\mathrm{Nu} \sim \mathrm{Ra}^{1/3}$. Bouillaut et al. (2019) took this setup a step further and showed the transition from the classical scaling to the ultimate scaling occurred as ℓ/H increased. Conceptually speaking, as ℓ/H becomes very small, we should expect the system to tend towards a Rayleigh Bénard convection type. In this kind of system, the heat flux from the source into the bulk is limited by the intermediate thermal boundary layer, so the efficiency of the heating is reduced.

It should be noted that the system of Lepot et al. (2018) and Bouillaut et al. (2019) is similar in spirit to the one presented in this chapter, though it is not identical. They performed experiments on fresh water heated from below with a linear equation of state, whereas we are simulating cold water heated from the top with a non-linear equation of state. In the simulations presented below, the non-dimensional attenuation lengths are $\mu_1^{-1} = \ell/H = (0.0977, 0.1953, 0.2930)$, whereas the range of Bouillaut et al. (2019) was $\ell/H = 0.0015 - 0.096$.

Since the convective instabilities are a result of the unstable stratification created by the thermal forcing, it is reasonable to surmise that the instabilities would have inherent length scales proportional to the length scale of the inverse stratification; a quantity set by ℓ. If $\ell \sim H$, then the bottom boundary will have some role to play, potentially limiting the growth of the instabilities, but in the context of actual lakes, the depth is often much greater than the attenuation length. Parameterization of the effect of μ_1 on a laucustrine system could be useful for the purposes of modelling vertical convection. The results of Lepot et al. (2018) and Bouillaut et al. (2019) show that it may be necessary to include this parameter in models to accurately reflect the vertical heat flux. For instance, for particularly shallow regions, clearer water is more likely to efficiently transport heat downward, (larger ℓ), where as in more turbid lakes, the efficiency of the vertical heat flux is not as high. Shallower regions such as sidearms are responsible for creating lateral intrusions that flow into deeper regions of the lakes, leading to (among other things) an increased rate of mixed layer warming (Ulloa et al., 2019).

3.5.4 Prandtl Number

The Prandtl number is simply the ratio of molecular viscosity and thermal diffusivity is held constant across all simulations at a value of 10. It is written as

$$\mathrm{Pr} = \frac{\nu}{\kappa}. \tag{3.40}$$

This value is representative for flows with temperatures near T_{md} as many recent studies use a constant Prandtl number in this range. See for instance Olsthoorn et al. (2019) and Ulloa et al. (2019) for recent cold water studies. In reality, since the viscosity and thermal diffusivity are both weak functions of the temperature near water's freezing point the Prandtl number varies about the chosen value of 10 slightly. For instance, Pr varies between about 13.84 at 0.01°C and 9.645 at 5°C (Dinçer and Zamfirescu, 2016). Lepot et al. (2018) briefly discussed the influence of the Prandtl number on the non-dimensional vertical heat flux, and they showed that varying the Prandtl number between 1 and 10 led to a relative independence of the heat flux on this parameter. They did not perform a comprehensive study, but in the range relevant to this thesis, the Pr dependence does not appear to be strong according to their results.

3.5.5 Aspect Ratio

μ_2 represents the "aspect ratio", and its significance arises when considering the effect of domain size on the instability formation. It is written as

$$\mu_2 = \frac{L}{\ell}. \tag{3.41}$$

We have established that the attenuation length ℓ sets the length scale inherent to the inverse stratification, subsequently setting the approximate length scale of the fastest growing mode. If the domain size is large enough to permit the fastest growing mode, then increasing μ_2 beyond this critical value simply allows more copies of the instability to grow. Allowing several copies of the instability to coexist can lead to pairing. An example of the pairing instability for Kelvin-Helmholtz billows can be seen in figure 2(f) of Mashayek and Peltier (2012). Thus, in the limit of large μ_2, the dynamics should initially be unchanged. However, beyond the initial growth of the instabilities, there may be some non-linear coupling of instabilities, thus μ_2 may be important late in the evolution. A focused discussion on the non-linear coupling is saved for followup work to this thesis.

3.6 Scaling for the Sheared System

The sheared system includes two more independent parameters; the initial background current velocity U_0, and the shear layer transition thickness δ. This creates two new non-dimensional groupings that describe the system. Once the background current has been added to the flow, there is now a mechanical source of energy that can move heat.

Consider the dimensional initial condition $U(z)$ in (3.8). We can scale it by the buoyancy velocity derived in (3.23). Letting

$$U(z) = \mathscr{U}(z)\mathcal{U}, \tag{3.42}$$

where $\mathscr{U}(z)$ is the dimensionless initial condition. This allows us to re-cast (3.8) in non-dimensional form as:

$$\mathscr{U}(z) = \frac{U_0}{\mathcal{U}}\frac{\ell}{H}\int_0^z \left(1 + \tanh\left(\frac{z' - \frac{1}{2}\mu_1}{\mu_3}\right)\right) dz'. \tag{3.43}$$

The prefactor of ℓ appears because z' scales with attenuation length. By multiplying the top and bottom of the coefficient of the integral by ℓ, H, and ν, we can write the

non-dimensionalized initial condition as

$$\mathscr{U}(z) = \frac{1}{\mu_1^2}\sqrt{\frac{\mathrm{Re}^2}{\mathrm{Gr}}}\int_0^z \left(1 + \tanh\left(\frac{z' - \frac{1}{2}\mu_1}{\mu_3}\right)\right) dz'. \tag{3.44}$$

where

$$\mathrm{Re} = \frac{U_0 H}{\nu} \tag{3.45}$$

is the Reynolds number (discussed below).

In studies where both buoyancy driven convection (free convection) and forced convection (convection driven by mechanical sources) coexist and are on similar scales, the motion is labelled as "mixed convection". Traditionally, the parameter that is used to characterize mixed convection is the bulk Richardson number (Gebhart et al., 1988) Ri_b, and is defined here as

$$\mathrm{Ri}_b = \frac{\mathrm{Gr}}{\mathrm{Re}^2}. \tag{3.46}$$

For example, this parameter was used as a control parameter in the numerical study of turbulent mixed convection in Pirozzoli et al. (2017). Note that (3.46) is different than the traditional form of the gradient Richardson number used in studies of hydrodynamic stability $\mathrm{Ri} = N^2/U_z^2$ (N^2 is the buoyancy frequency and U_z^2 is the squared vertical shear). However, since Gr quantifies the magnitude of the buoyancy term relative to the viscous term in the momentum equations, and (3.44) shows that the Reynolds number quantifies the magnitude of the background shear flow relative to the viscous velocity scale, (3.46) plays a similar role to the gradient Richardson number of comparing the magnitude of the buoyancy driven velocities to the velocities of the background shear flow.

When $\mathrm{Gr} \gg \mathrm{Re}^2$ ($\mathrm{Ri}_b \gg 1$), free convection is the dominant heat transfer mechanism, and heat moved by mechanical effects, like a background current or pressure gradient, becomes secondary. We can see that in (3.44), if Ri_b becomes large, the coefficient in front becomes small and the non-dimensional background current velocity scale approaches zero. In this case, the currents driven by free convection due to heating are simply stronger than the background current.

In the opposite case, $\mathrm{Gr} \ll \mathrm{Re}^2$ ($\mathrm{Ri}_b \ll 1$), forced convection becomes the dominant heat transfer mechanism, meaning buoyancy driven currents are secondary to mechanical ones. This occurs when the background current velocity is much larger than the buoyancy velocity scale. If there is a large discrepancy in these scales, it is sensible that the motion may not scale with $\mathcal{U}$, and would instead scale with U_0. From a quantitative perspective, the dominant heat transfer mechanism is reflected in the non-dimensional heat

flux (the Nusselt number), and it scales differently depending on the particular parameter regime (Grossmann and Lohse (2000) for example) and whether forced, or free convection is dominant.

As a brief aside, Ri_b can appear as a governing parameter in the equations of motion instead of the initial condition like (3.44). Pirozzoli et al. (2017) simulated the steady-state interaction between Rayleigh-Bénard convection and a background shear flow sustained by a pressure gradient. In their study, they chose the bulk flow current speed as their characteristic velocity scale, rather than a buoyancy driven velocity scale. They considered the steady-state evolution of domain scale rollers aligned with the background shear once the turbulence was fully developed in the range $\mathrm{Ri}_b \in [0.001, 100]$ as well as extreme values of ∞ (corresponding to pure Rayleigh-Bénard convection) and 0 (corresponding to a pure Poiseuille flow). Their choice of scaling velocity was sensible as they considered a steady-state response of the system where a pressure gradient was applied to balance the dissipative effects by turbulence, leaving the initial condition effectively forgotten, and as a result of this choice, Ri_b appeared as the coefficient to the buoyancy term.

The new set of non-dimensional parameters that govern the system are those in equation (3.34) and

$$\mathrm{Re} = \frac{U_0 H}{\nu}, \quad \mu_3 = \frac{\delta}{\ell}. \tag{3.47}$$

3.6.1 Reynolds number

The Reynolds number measures the relative magnitudes of inertia effects ($\boldsymbol{u} \cdot \nabla \boldsymbol{u}$) versus viscous effects ($\nu \nabla^2 \boldsymbol{u}$) and is denoted by

$$\mathrm{Re} = \frac{U_0 H}{\nu}. \tag{3.48}$$

The magnitudes of the Reynolds number is often used as an indicator for the level of turbulence, with higher Reynolds numbers indicating higher levels of turbulence. Generally speaking, Reynolds numbers are often much lower beneath ice due to the very weak currents. Field measurements of currents beneath ice indicate speeds on the order of one to several mm/s. See Malm et al. (1998) in Lake Vendyurskoe (Russia) or Rizk et al. (2014) in Lake Pääjärvi (Finland) for examples. The currents are often driven by seiching motion generated by vertical oscillations in ice-cover or basin-scale gyres and not directly from the wind. More recent numerical work by Ramón et al. (2021) and Ulloa et al. (2019) on an idealized lake indicates that near surface return flows generated by sidearm gravity currents had velocities on the order of about 5 mm/s for realistic rates of heating. This

is a stark contrast to the ice-free seasons where surface currents and surface waves are driven directly by the wind. Some of the momentum is extracted from the wind and is used to grow surface waves, while some penetrates beneath the wave affected surface layer and generates subsurface currents. These surface currents are functions of the wind speed and can range from relatively quiescent ($\mathcal{O}$(mm/s)) to vigorous ($\mathcal{O}$(m/s)) ($\mathcal{O}$ means "of order of magnitude" in this context) under strong wind conditions. This speaks to a more general phenomenon where under-ice currents are generated by weaker mechanisms when compared to the forcing mechanisms in the ice-free seasons.

3.6.2 Non-dimensional transition thickness

This parameter controls how rapidly with depth the background velocity profile transitions from the initially still state to the linearly increasing state. It arises from the initial conditions and it is denoted by

$$\mu_3 = \frac{\delta}{\ell}. \tag{3.49}$$

This parameter is not expected to have a meaningful effect once convective instabilities develop, and will not be discussed any further.

3.7 Vorticity Diagnostics

The main goal of this study is to examine how the system moves from a quasi-two-dimensional state to a fully three-dimensional state, and what role the attenuation length and the magnitude of the shear play in that process. A simple way to establish when the flow goes fully three-dimensional is to examine the vorticity components;

$$\boldsymbol{\omega} = \nabla \times \boldsymbol{u} \tag{3.50}$$

as well as the enstrophy;

$$\frac{1}{2}|\boldsymbol{\omega}|^2 = \frac{1}{2}(\omega_x^2 + \omega_y^2 + \omega_z^2), \tag{3.51}$$

where $\boldsymbol{\omega} = (\omega_x, \omega_y, \omega_z)$ (subscripts indicate direction in this context). For brevity, enstrophy components normalized by the total enstrophy are denoted as

$$\bar{\omega}_x^2 = \frac{\omega_x^2}{|\boldsymbol{\omega}|^2}, \quad \bar{\omega}_y^2 = \frac{\omega_y^2}{|\boldsymbol{\omega}|^2}, \quad \bar{\omega}_z^2 = \frac{\omega_z^2}{|\boldsymbol{\omega}|^2}. \tag{3.52}$$

Note that since enstrophy is a scalar quantity, the term "components" is an abuse of notation. When we refer to enstrophy components in the following sections, we are really referring to each quantity in (3.52).

A characteristic of three-dimensional fluid flow is that vorticity vectors typically have three non-zero components, while in two dimensional flow, there is only one non-zero component. Thus, to determine when and under what conditions the streamwise symmetry of the flow breaks, we can first look at how the vorticity components change over time.

We can take the curl of the dimensionless momentum equations to get a system of vorticity equations

$$\frac{D\omega_x}{Dt} = \frac{1}{\sqrt{\mathrm{Gr}}}\nabla^2\omega_x + \frac{\partial}{\partial y}\left(T\left(1-\frac{\Theta}{2}T\right)\right) + \boldsymbol{\omega}\cdot\nabla u, \tag{3.53}$$

$$\frac{D\omega_y}{Dt} = \frac{1}{\sqrt{\mathrm{Gr}}}\nabla^2\omega_y - \frac{\partial}{\partial x}\left(T\left(1-\frac{\Theta}{2}T\right)\right) + \boldsymbol{\omega}\cdot\nabla v, \tag{3.54}$$

$$\frac{D\omega_z}{Dt} = \frac{1}{\sqrt{\mathrm{Gr}}}\nabla^2\omega_z + \boldsymbol{\omega}\cdot\nabla w. \tag{3.55}$$

The terms on the right hand side of each of the above equations are responsible for the net changes in vorticity. The Laplacian (∇^2) terms diffuse vorticity in regions of high spatial variation, but will be ignored in the following analysis. The remaining terms are the baroclinic generation terms and the vortex tilting/stretching terms $\boldsymbol{\omega}\cdot\nabla\boldsymbol{u}$. Next, two metrics called S_i and B_i are defined as

$$S_i = \sqrt{\iint |\omega_j\partial_j u_i|^2 dx_1 dx_2}, \tag{3.56}$$

$$B_i = \sqrt{\iint |\epsilon_{ij3}\partial_j \rho_3|^2 dx_1 dx_2}. \tag{3.57}$$

S_i and B_i (note that $B_3 = 0$) are the horizontal L^2 norms of the tilting/stretching terms and baroclinic generation terms for the ith component of vorticity ($i = 1, 2, 3$) respectively. Note that we are letting $\rho_3 = T\left(1-\frac{\Theta}{2}T\right)$ for brevity in (3.57). These metrics allow us to compare the strengths of the vortex stretching/tilting and baroclinic terms in equations (3.53)–(3.55) at every vertical level in the domain.

3.8 Results

The results of this chapter are broken up into two subsections. The first describes the instability growth phase, and the second describes the transition to a turbulent state. The first subsection is broken down further into separate sections that describe the roles the shear layer and the attenuation length play. The role that the shear layer plays in that process is described through comparison of the Base, Slow, and Fast cases. These cases are chosen because they show three different behaviours based on the magnitude of the shear flow. The Base case shows one extreme where there is no shear flow, and the system evolves under only the volumetric thermal forcing. The Slow case presents an example where there is a background shear flow, but it is not strong enough to suppress the streamwise variation in the instability growth. Finally, the Fast case provides an example where the shear flow can temporarily prevent the streamwise variation in the instability growth. The role that the attenuation length plays in the instability growth is discussed after, with reference to the Fast, Medium-Attenuation and Short-Attenuation cases. These cases demonstrate how changing the attenuation length changes key aspects of the instability growth and eventual destabilization. The second section describes the transition to the full three-dimensional state and cases are compared as necessary.

Simulations are initialized with a uniform temperature (1°C), and are then thermally forced using the Beer–Lambert law. This generates an unstable background density profile. Figure 3.3 shows the temperature field at three times throughout the evolution of the Fast case. In this figure, the background current flows along the x direction (approximately out of the page). Panels (a) and (b) show the evolution during the instability growth phase, and panel (c) shows the water column once the instabilities have collapsed into a fully three-dimensional state. Note that fluid with temperatures near T_0 is rendered as nearly transparent, and the opacity increases with temperature. Figure 3.3 is one example of a case that exhibits temporary quasi-two-dimensional instability growth, and this is followed by a rapid collapse to a complex three dimensional turbulent state. The following sections describe the instability growth and transition to turbulence under different background and forcing conditions.

3.8.1 Instability Growth Phase

Both the magnitude of background shear flow, U_z, and the attenuation length of the thermal forcing, ℓ, play different roles in setting the growth rate and critical wavenumber of the instability as well as controlling the eventual destabilization of the water column. These two parameters will be discussed separately.

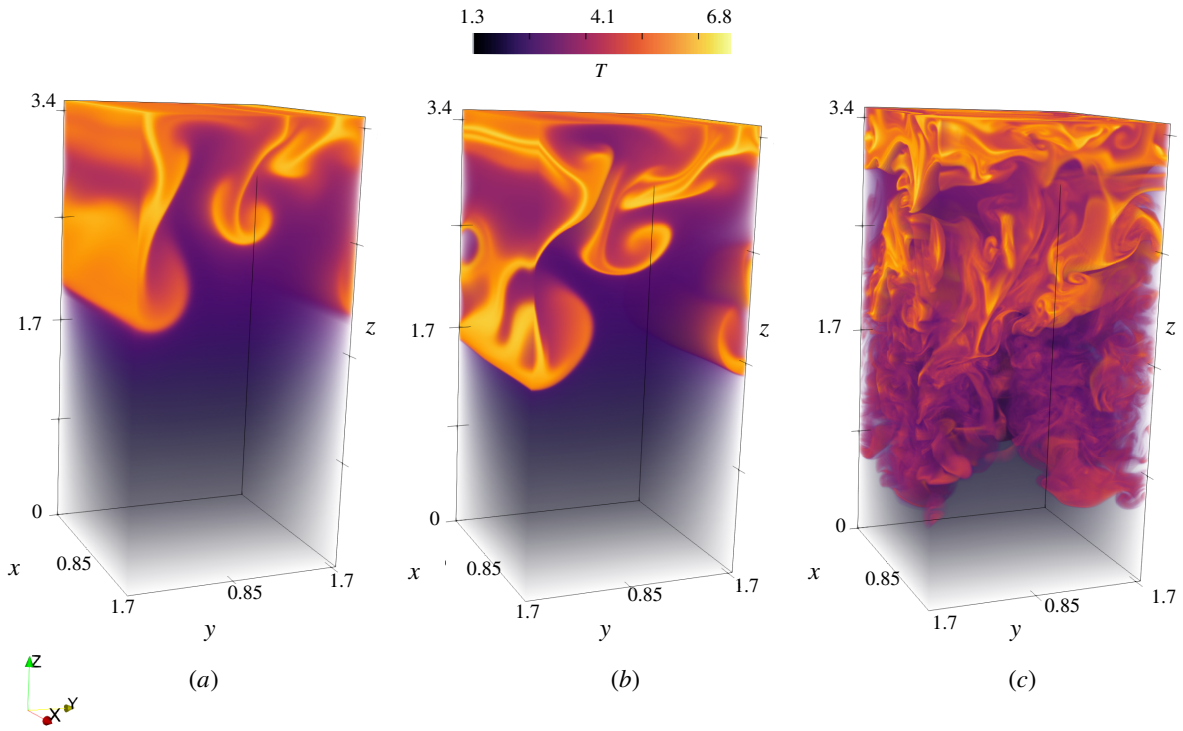

Figure 3.3: Renderings of the temperature field for the Fast case during the instability growth phase (panels (a) and (b)) and after full collapse of the water column (panel (c)). All temperatures and times are non-dimensionalized using the temperature scale in (3.32) and timescale in (3.33) respectively. Panel (a) is at $t = 5.9$, panel (b) at $t = 6.3$ and panel (c) and $t = 7.8$. The background current is directed along the x axis (indicated by the orientation axes in the bottom left corner). Higher temperatures correspond to higher opacity.

The role of the background shear flow, U_z

During the instability growth phase, the magnitude of the background shear controls whether or not the initial instability formation occurs with or without a preferential direction in the horizontal plane. Of the cases considered in table 3.2, only the Slow and the Base case exhibit randomly seeded instabilities, whereas every other case exhibits instabilities aligning themselves with the background shear flow. A comparison of the Fast and Slow cases in figure 3.4 highlights the basic role that the shear flow plays as the convective plumes grow. Panels (a) and (c) show $y-z$ and $x-z$ slices of w for the Slow case, while (b) and (d) show the same slices of w for the Fast case. Both $y-z$ slices have temperature contours overlaid in black. The $y-z$ slice is taken in the middle of the domain and the white dashed line in panels (a) and (c) indicate the heights at which the $x-y$ slices are taken. In panels (a) and (c), the direction of the background current is out of the page, while in panels (b) and (d) it is from left to right. The times of the plots are on the figure. Note that since the timescale is independent of the background current, and the intensity of the radiation is constant in every case, plots taken at the same time have had the same amount of thermal energy added.

As the Slow case develops, the instability caused by the unstable stratification generates regions of upwelling and downwelling near the surface, but the convective plumes that form do not orient themselves either as parallel or perpendicular to the background current. The Fast case, on the other hand, exhibits a strong and persistent streamwise homogeneity until full three-dimensionalization (discussed in the next section). It is interesting to note that the magnitude of the vertical velocity is the same for both of the panels shown, even though the magnitude of the background current varies by an order of magnitude between them. This suggests that the vertical currents induced during the instability growth phase are mostly independent of the background current, thus being solely influenced by the thermal forcing. This is confirmed by calculating the vertical buoyancy flux $\langle -\rho w \rangle$ for the Fast, Short-Attenuation, and Base cases and noting they are all on the same order of magnitude (not shown). There is some field evidence for this. Bouffard et al. (2019) estimated convective velocities over the course of March 2017 in Lake Onego (Russia), and the variation in daily maximums was very small, indicating that there could be an independence of the convective velocity scales from other under-ice flow factors.

The role of the attenuation length, ℓ

The role of ℓ is to control the rate at which incident radiation is attenuated with depth. The rate that energy is attenuated influences the size of the convective instabilities that

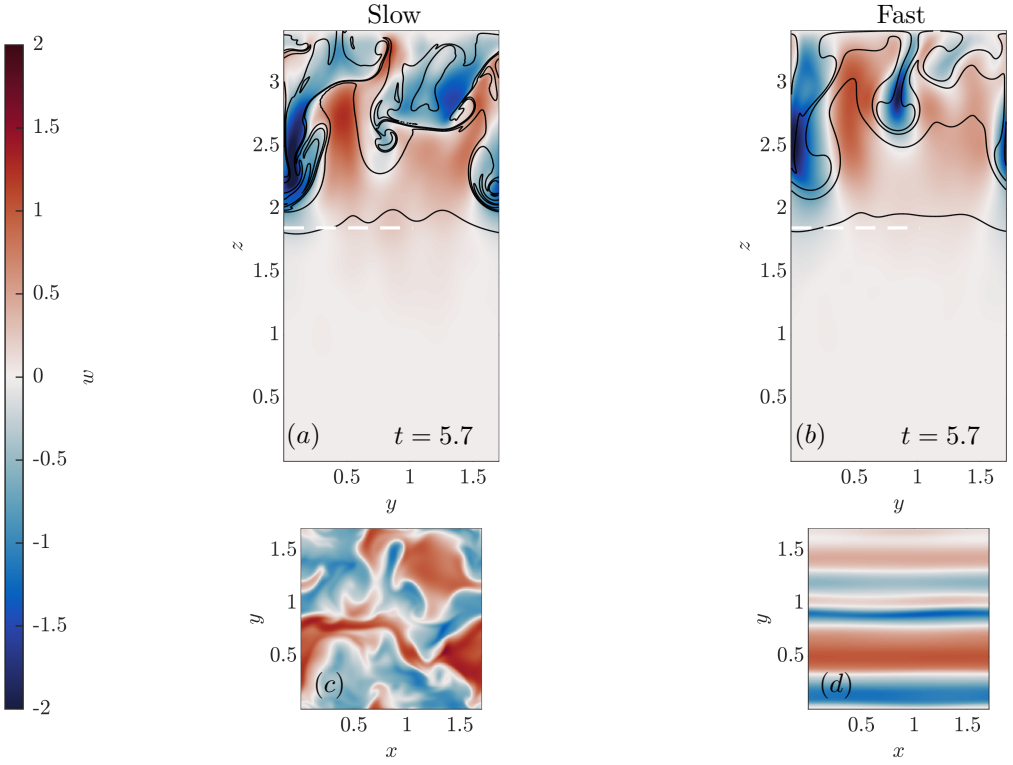

Figure 3.4: A comparison of the w fields for the Slow and Fast cases. The times are on the figure. $y-z$ slices of the Slow and Fast cases are shown in panels (a) and (b). $x-z$ slices at the same times are shown for both cases in panels (c) and (d). The height that the $x-z$ slice is taken at is indicated by the white dashed line in panels (a) and (b). The $y-z$ slices are taken in the middle of the domain.

grow. Given a constant rate at which energy is introduced by the thermal forcing, smaller values for ℓ force this energy to be concentrated over a smaller depth range thus leading to larger density differences over smaller distances. We can see the effect that the variation in attenuation length has on the instabilities by solving the viscous Taylor-Goldstein (vTG) equations (Appendix A) (Smyth et al., 2011).

For cases when the shear is sufficiently strong so as to orient the instability cores in the streamwise direction (as in the Fast case), we solve for growth rates of perturbations in the $y - z$ plane only. We make this assumption to facilitate a clearer comparison between growth curves for cases with different attenuation lengths. This decision is motivated by solving the vTG equations (in dimensional form) assuming that perturbations in any direction can grow (not shown), and noting that the maximum growth rate is found to lie along the $\tilde{k} = 0$ (streamwise wavenumber) boundary. This limit allows us to consider perturbations with only spanwise structure. Since the streamwise background current does not have any structure in the spanwise direction, it does not play a part in determining the stability of modes in the spanwise direction, and is not included in the model presented in Appendix A.

We solve the system using mean dimensional density profiles at times before the instabilities have significantly modified the stratification. Since heat is continuously added to the system, the maximum growth rates given by the vTG model are only an estimate, as a primary assumption of the model is a steady background state. Thus, we use the results of the linear model only as general guidelines for the understanding the instability growth, and not for a quantitative discussion.

The density profiles and growth curves are presented in figure 3.5. Quantities related to this figure are reported in dimensional terms for visual clarity. Panel (a) shows the density profile of the horizontally averaged temperature at 1000 s (solid lines) and 2500 s (dashed lines) for attenuation lengths of 0.2 m (red) and 0.6 m (blue). These correspond to the attenuation lengths in the Short-Attenuation and the Fast cases respectively. Since the amount of heat added to the domain is linearly related to the time of each profile, the profiles shown at 2500s have 2.5 times more heat added than the profiles at 1000s. Since the equation of state is non-linear, the density profile will not have the exact same structure as the thermal forcing, but since Θ is much less than unity in these cases, the increase in density is approximately linearly related to the increase in temperature. Pursuant to this, top-bottom density differences of the profiles at 2500s are about 2.5 times as large as those taken at 1000s. Thus the aspects of the density structure attributed to the non-linear equation of state are secondary for the dynamics.

As heat is added, the resultant density profiles take on an exponential structure similar

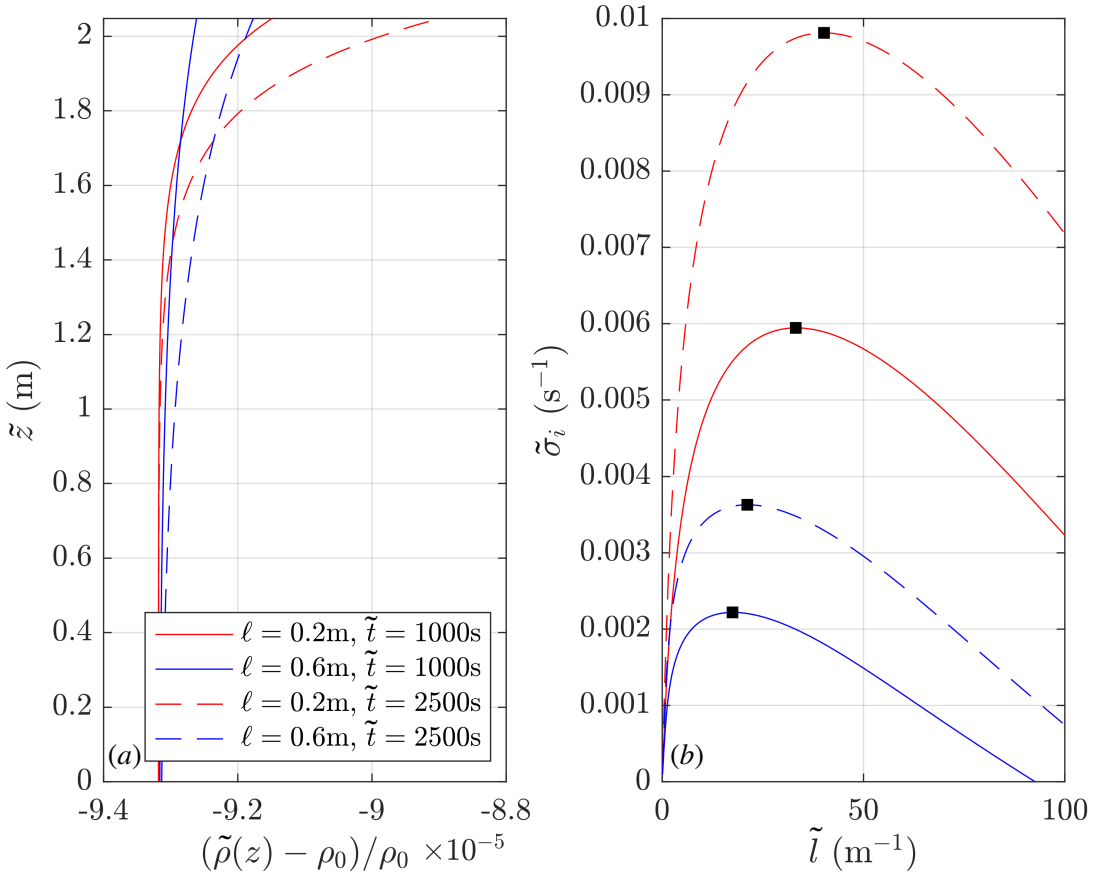

Figure 3.5: Panel (a) shows background density profiles at 1000s (solid) and 2500s (dashed) for the Fast and the Short-Attenuation cases. Panel (b) shows the growth rates as a function of spanwise wavenumber $\left(\tilde{l}\right)$. Note the difference in the location of the peak of the growth curve along the $\tilde{l}$ axis for the different attenuation lengths. The peaks are highlighted with markers. Note also that the growth rate is larger for the shorter attenuation length.

to the thermal forcing, thus gaining a vertical length scale on the order of the attenuation length. This vertical length scale should have some role to play in setting the horizontal length scales of the instabilities that grow in practice. Panel (b) shows the growth curves for instabilities growing on the background density profiles in panel (a). As the background state for a given attenuation length becomes more unstable as more heat is added (a comparison of curves with the same color), the peak of each growth curve shifts along the $\tilde{l}$ (spanwise wavenumber) axis only slightly but its magnitude increases by roughly 50%. This means that as more heat is added to the domain, the wavenumber pertaining to the fastest growing instability does not significantly change, but the growth rate does. This is to be expected because heat added to the domain increases the temperature differences between overlying layers of fluid, thus increasing their local Atwood number. However, for a given time, a comparison of cases with different attenuation lengths (a comparison of curves with the same linestyle) reveals a significant difference in both the location of the peak of the growth curve, as well as the growth rate. This figure suggests that the shorter attenuation lengths have faster growing instabilities with shorter characteristic length scales. This is to be expected because shorter attenuation lengths imply a larger amount of heat deposited near the surface across a smaller vertical scale, thus inducing a larger density gradient near the surface.

We can examine the role the attenuation length plays in practice by looking at the vertical velocities for the early development of the Short-Attenuation case at two times, shown in figure 3.6. The two main conclusions of figure 3.5(b) are qualitatively correct as smaller scale convective instabilities are observed to form much earlier in the evolution of that case relative to the Fast case. This can be seen by comparing figures 3.4(b) and 3.6(b), for example.

3.8.2 Transition Phase

The Instability Growth phase focused on the early development of the instability as the system gained heat and became more unstable. The following section highlights the processes that occur as the instabilities achieve a finite amplitude, subsequently collapse and the system moves to a turbulent regime. A full discussion of the fully developed turbulent regime itself is left for future work.

As the flow develops, the streamwise symmetry (quasi-two-dimensional state) from the growth phase breaks, leading to a three-dimensional turbulent state. A qualitative appreciation of an example of the fully three-dimensional state can be seen by considering panel (c) in figure 3.3. The full three-dimensionalization of the system will be investigated by considering the enstrophy components defined in (3.52).

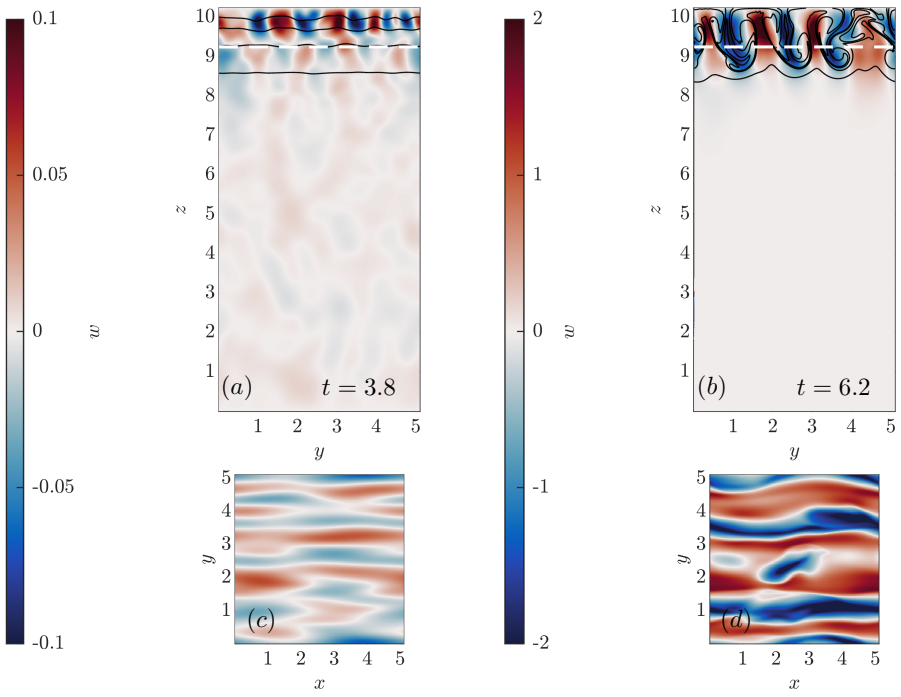

Figure 3.6: A comparison of the w field at two times for the Short-Attenuation case with temperature contours overlaid. Times are chosen to highlight the initial development of the instability and the state of the instability shortly before collapse. The times are on the figure. $y - z$ slices are shown in panels (a) and (b), and $x - z$ slices taken at the height indicated by the white dashed line. These are shown in panels (c) and (d). Note the difference in the colorbar limits in panels (a) and (c) versus (b) and (d).

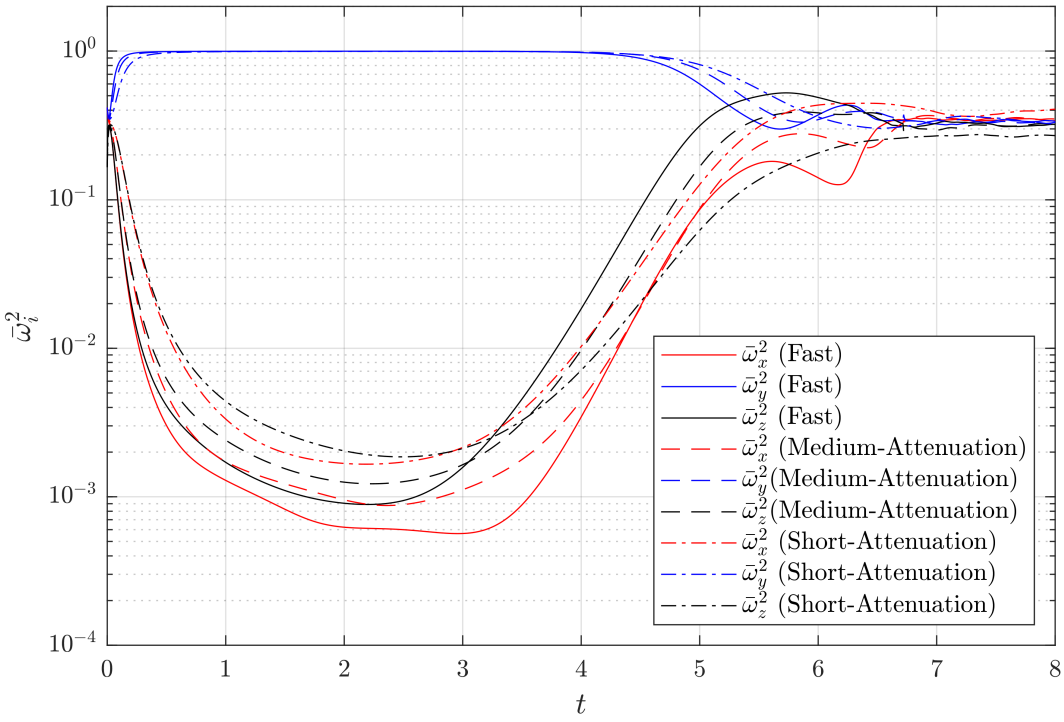

Figure 3.7: Enstrophy components normalized by the total enstrophy at that time for the Fast case (solid), Medium-Attenuation case (dashed) and the Short-Attenuation case (dot-dashed lines). For all cases shown, the streamwise, spanwise, and vertical components of enstrophy are red, blue, and black respectively.

Figure 3.7 shows the enstrophy components for the Fast case ($-$), Medium-Attenuation case ($--$) and Short-Attenuation case ($-\cdot$). The x, y and z components for each case are shown in red, blue, and black. This plot can be broken into two regimes, one where the streamwise and vertical enstrophy components are distinctly different than the spanwise component, and one where they are comparable. The former corresponds to when the instability is forming and transitioning, and the latter corresponds to when the flow is strongly three-dimensional and disordered.

This plot concisely demonstrates that the system reaches a turbulent state on a comparable non-dimensional timescale. Thus as the attenuation length is decreased, the dimensional time at which the system reaches the turbulent state is earlier. Figure 3.7 also highlights that prior to the full three-dimensionalization, there is an increase in the streamwise and vertical components of the enstrophy; $\bar{\omega}_x^2$ and $\bar{\omega}_z^2$ respectively. Thus, most of the enstrophy that is initially present is due to the background current, (appearing in $\bar{\omega}_y^2$) while the streamwise and vertical components emerge only after convective instabilities begin to modify the background state. Note that there is some initial activity in the streamwise and vertical components due to the white noise perturbation at the beginning of each simulation, but this decreases due to viscosity and the numerical filter.

As the instabilities develop and carry energy down to smaller scales with them, the net trend of the streamwise and vertical components of the enstrophy is to increase, resulting in a relative decrease of the spanwise component. This results in all three components being equal in magnitude. As the emergent components grow, $\bar{\omega}_z^2$ is more active than $\bar{\omega}_x^2$ for the Fast and Medium-Attenuation cases, and the disparity between the two is higher in the Fast case. The Short-Attenuation case is slightly different in that the streamwise component is more active than the vertical component prior to three-dimensionalization. This could arise from the fact that the instabilities grow fast enough that the shear is not able to completely suppress streamwise perturbations. This is evident in figure 3.6 (c) and (d), as there is some streamwise variation in the vertical velocity.

It should be noted that significant modification of the background current occurs only after the convective plumes are very large and have had sufficient opportunity to bring momentum lower into the water column. Since the instabilities induce vertical fluxes of momentum, it is reasonable to expect some change in the mean profiles of velocity, since the current is incapable of being maintained by forcing or a pressure gradient. Shown in figure 3.8 are mean velocity profiles for the Fast (left) and Short-Attenuation (right) cases at three different times. The times are chosen are to highlight the state of the mean current before, during, and after the instability growth phase

For both cases, the key is that during the initial formation of the instability, the mean

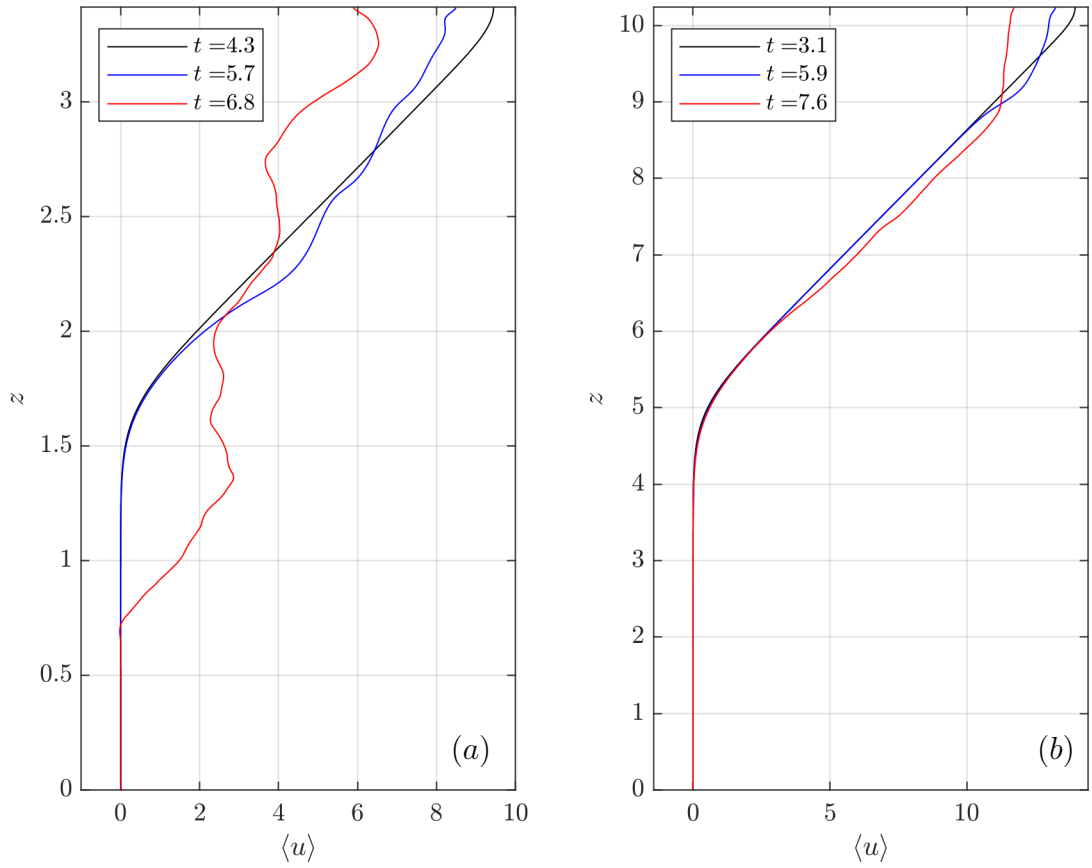

Figure 3.8: Streamwise current profiles at three times for the Fast (panel(a)) and Short-Attenuation (panel(b)) cases. Times are chosen to highlight the mean streamwise current profile before instability formation (black), during the transition (blue), and in the three-dimensional state (red). Angle bracket represent horizontal average.

current becomes slightly modified by the growth of the instabilities, but there is still some evidence that the shear layer persists. However, once the instabilities have grown significantly, the shear layer structure has changed substantially. At this point, the instabilities have moved momentum from the near surface regions to lower in the water column. The dimensional times that this process occurs is earlier for the Short-Attenuation case, consistent with the results described above.

Now consider figure 3.9 where we have taken the horizontal L^2 norm of each vorticity component for the Fast case. The horizontal L^2 norm is useful for assessing information regarding the vertical structure in the vorticity components. Panels (a,b,c) show the norms of the streamwise, spanwise and vertical vorticity component (with vorticity of the background current removed). Coinciding with the rapid increase in spanwise vorticity in the Fast case from figure 3.7, panel (b) of figure 3.9 shows a front of strong spanwise vorticity propagating downwards. Finally, around $t = 6.5$ we see larger values of streamwise vorticity near the bottom of the shear layer, which coincides with the sharp increase from figure 3.7, and the three-dimensionalization of the flow.

As the convective plumes grow and flow downwards, they bring streamwise momentum with them. The generation of spanwise and vertical vorticity occurs because of a flux of streamwise momentum from the tip and sides of the plume into the fluid moving at a different velocity below. This momentum flux manifests itself as $\bar{\omega}_y$ produced at tip and $\bar{\omega}_z$ produced at the sides of the plumes.

A closer look at this process is presented in figure 3.10. Shown are $y - z$ slices of the three components of vorticity overlaid with contours of the streamwise velocity for the Fast case at $t = 5.7$. This time was chosen because it coincides with the first local minimum of $\bar{\omega}_y^2$ for the Fast case in figure 3.7. The Medium-Attenuation case follows the same general pattern and is not shown. Strong spanwise and vertical vorticity (panels (b) and (c)) are associated with strong variations in u, denoted by the spatial overlap of contours and large positive and negative vorticities. Generally speaking, the streamwise component of vorticity is not a function of the streamwise component of velocity, and must be generated by spanwise variations in w or vertical variations in v. While there is some shear on fluid parcels caused by the falling plumes interacting with the upwelling water, the spanwise variations of w generated by this motion are small because the spatial variations of w are much smaller than variations in the other velocity components.

Shown in figure 3.11 are vorticity slices for the Short-Attenuation case at $t = 6.6$. This time was chosen as it coincides with the first local minimum of $\bar{\omega}_y^2$ for the Short-Attenuation case in figure 3.7. The same underlying principles can be seen to apply, except this time, the streamwise vorticity production is higher and more comparable to

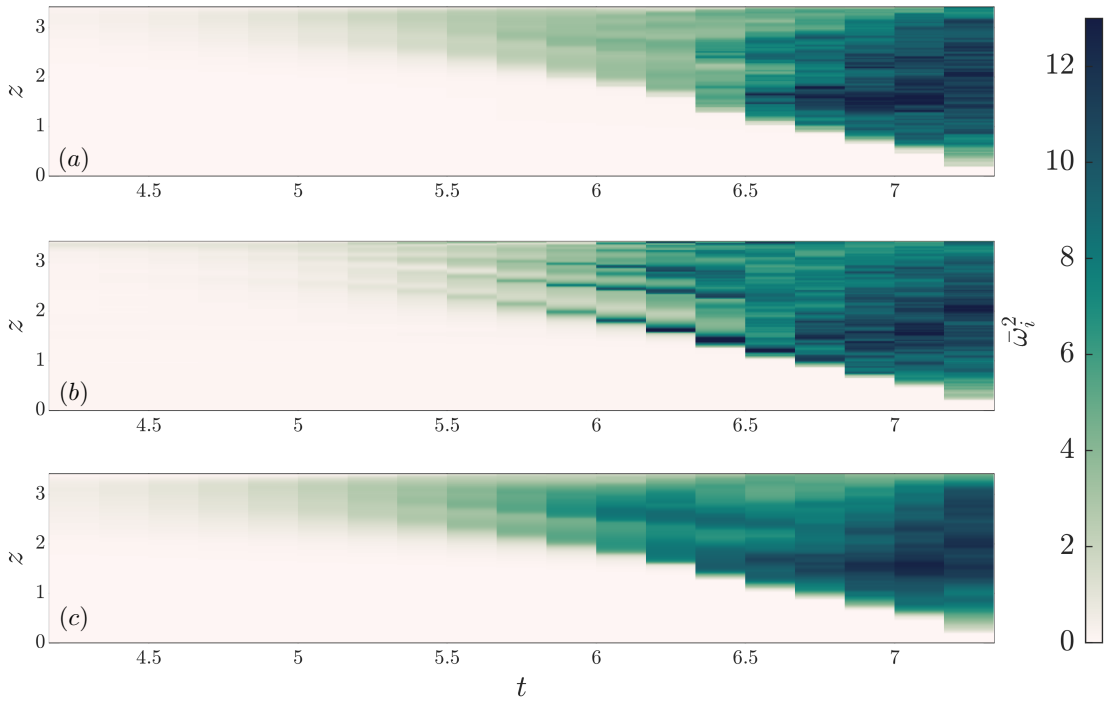

Figure 3.9: Horizontal L^2 norm of the vorticity components for Fast case. Panel (a) shows $\bar{\omega}_x^2$, panel (b) shows $\bar{\omega}_y^2$ and panel (c) shows $\bar{\omega}_z^2$. The vorticity contribution from the background current has been removed from $\bar{\omega}_y$ before squaring.

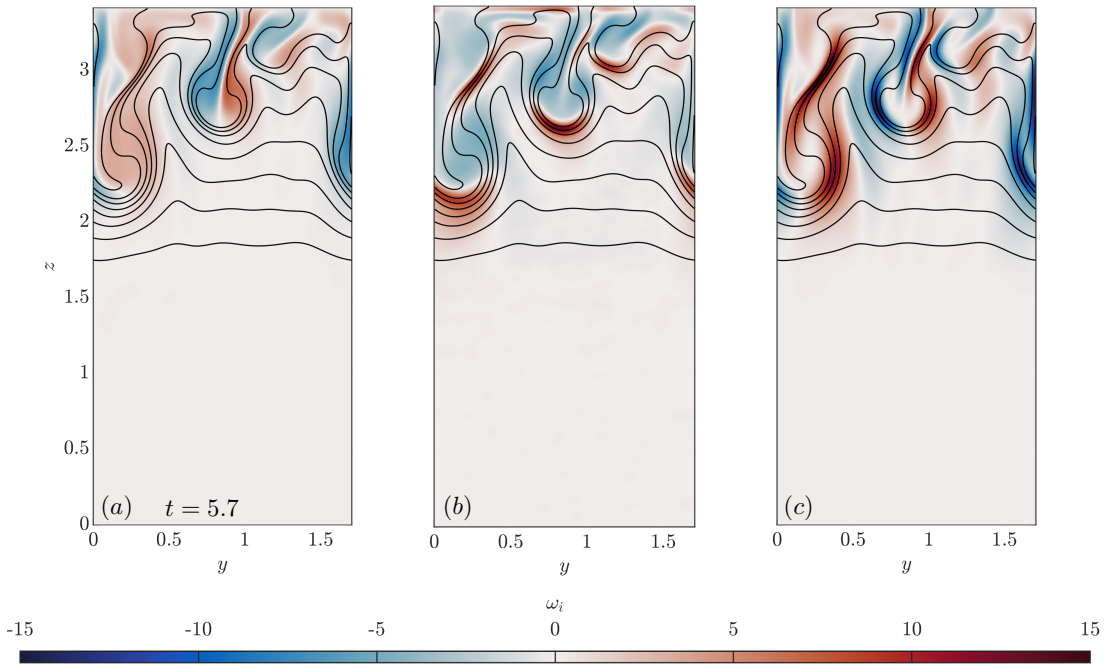

Figure 3.10: Panels (a) – (c) show the $y - z$ slices of each component of vorticity (x, y, and z respectively) at $t = 5.7$ for the Fast case. Contours of velocity are included on the plots.

the spanwise and vertical. Since the shorter attenuation length implies a smaller length scale for the instabilities, the density and velocity gradients are potentially higher, leading to more vorticity production. Since the streamwise vorticity in the Short-Attenuation case becomes as active as the other two components sooner relative to the Fast case, the system goes unstable much earlier than the Fast case. The implication is that the smaller scale instabilities create thinner interfaces and higher resultant velocity gradients leading to enhanced streamwise vorticity production and to an earlier transition to turbulence.

Below, we discuss the role that the vorticity dynamics plays in this process. To do this, first consider the terms that generate vorticity in the system, quantified by S_i and B_i.

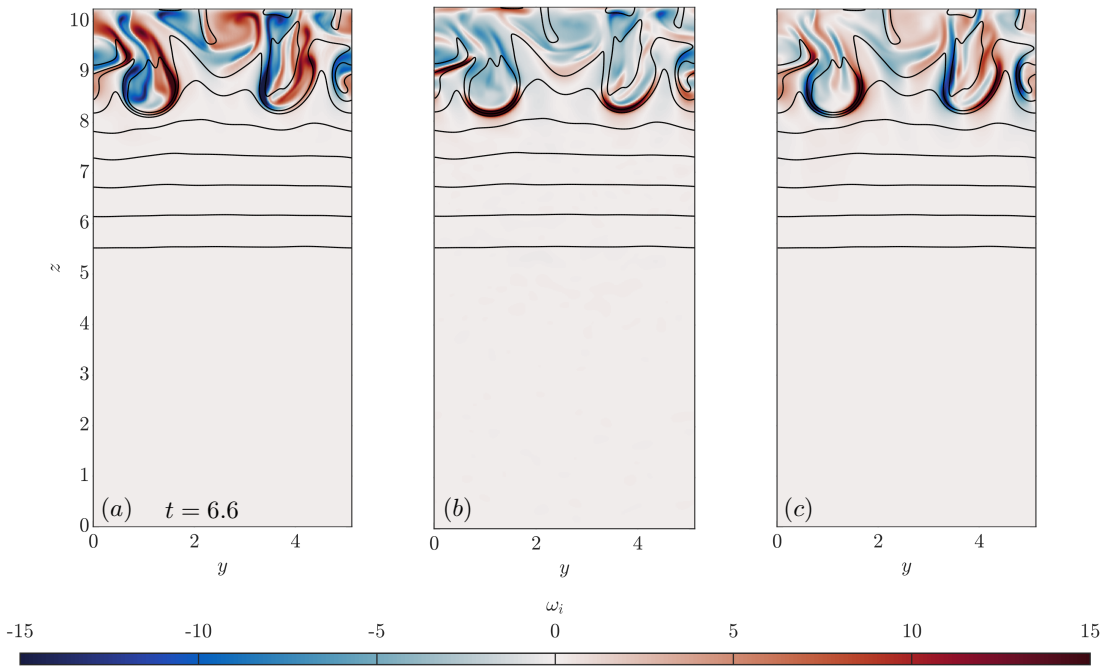

Figure 3.11: Panels (a) – (c) show the $y-z$ slices of each component of vorticity (x, y, and z respectively) at $t = 6.6$ for the Short-Attenuation case. Contours of velocity are included on the plots.

Shown in figure 3.12 (a) and (c) are profiles of S_i at $t = 5.6$ and $t = 6.3$ respectively for the Fast case. Panels (b) and (d) show the corresponding B_i values. The x, y, z components are given by the red, blue, and black curves. These times are shown because they describe the overall process that occurs during three-dimensionalization. For the Fast case, B_1 is systematically larger than S_1, but for the Slow case, S_1 and B_1 are generally comparable. This indicates that the generation of streamwise vorticity is primarily from baroclinic generation during the instability development phase in the Fast case whereas streamwise vorticity production is approximately the same from both mechanisms in the Slow case. At the same time, a comparison of S_2 and B_2 for the Fast case indicates that spanwise vorticity is generated primarily by vortex tilting/stretching as opposed to baroclinic production, while for the Slow case, these terms are of comparable magnitude again. This observation is consistent with the fact that there is very little streamwise variation in any variables at this time for the Fast case, where as the Slow case is fully three dimensional.

At a later time, during the three-dimensionalization of the Fast case we see that there is a substantial increase in S_1, S_2, and S_3 compared to the earlier time. Furthermore, the vorticity production coming from vortex tilting/stretching is greater than the baroclinic vorticity production by about an order of magnitude for both the spanwise and streamwise components. The baroclinic production is comparable across these two cases, while the production by tilting and stretching is greater in the Fast case. Thus, it is clear that it is vortex tilting/stretching that induces the three dimensionalization, and not the baroclinic generation of vorticity.

The same premise follows for the Short-Attenuation and Short-Attenuation-Slow cases. Profiles of S_i and B_i for the Short-Attenuation case are shown in figure 3.14, while such profiles are omitted for the Short-Attenuation-Slow case, as they are very similar to figure 3.13, but concentrated near the surface. Note that the non-dimensional times are not exactly the same between cases. However, qualitative comparisons can be made provided that the profiles are chosen just before the transition to three-dimensionalization. The key features to note here are the localization of the vorticity production near the surface, consistent with the smaller attenuation length and smaller instabilities, as well as the fact that the baroclinic generation of streamwise vorticity is much higher relative to the streamwise generation by tilting/stretching. This is consistent with higher density gradients induced by the smaller scale instabilities. This could explain the much larger streamwise component of vorticity when comparing figures 3.10 and 3.11.

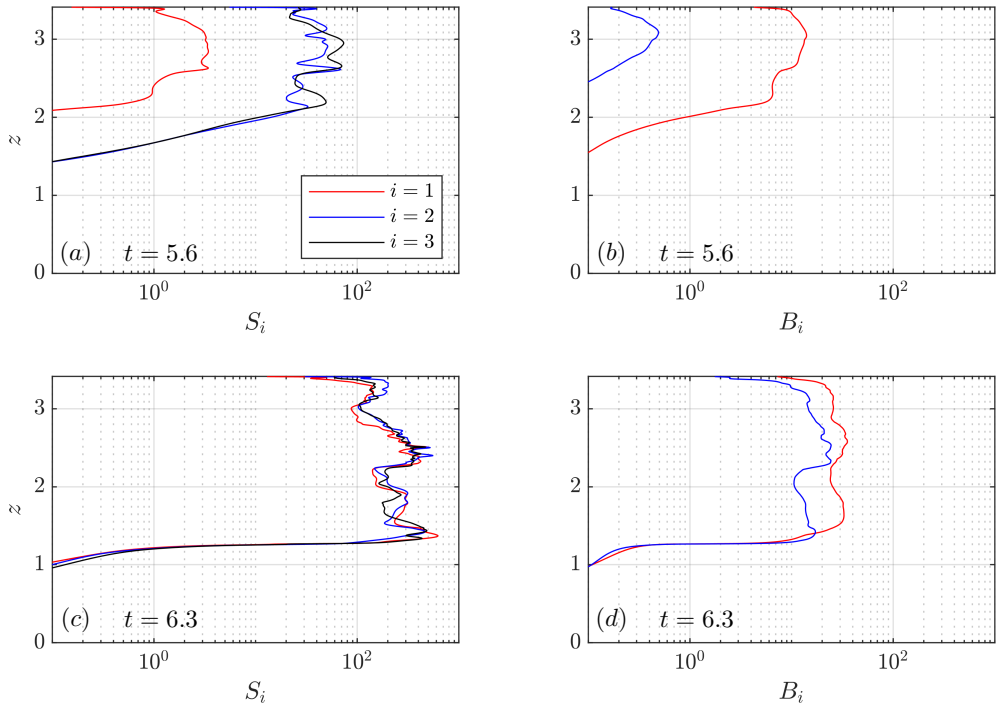

Figure 3.12: Panel (a) shows profiles of the horizontal L^2 norm of each component of vortex tilting/stretching for the Fast case at $t = 5.6$. Panel (b) shows the horizontal L^2 norm of each component of the baroclinic vorticity production at $t = 5.6$ for the same case. Panels (c) and (d) show the same quantities but at $t = 6.3$.

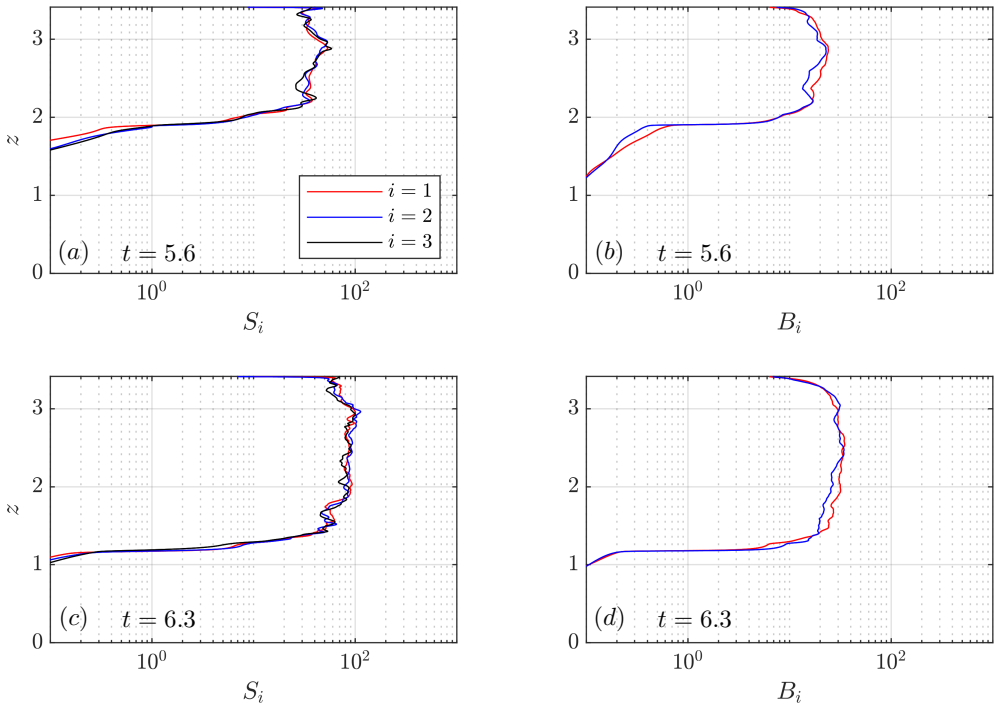

Figure 3.13: As in figure 3.12, but for the Slow case.

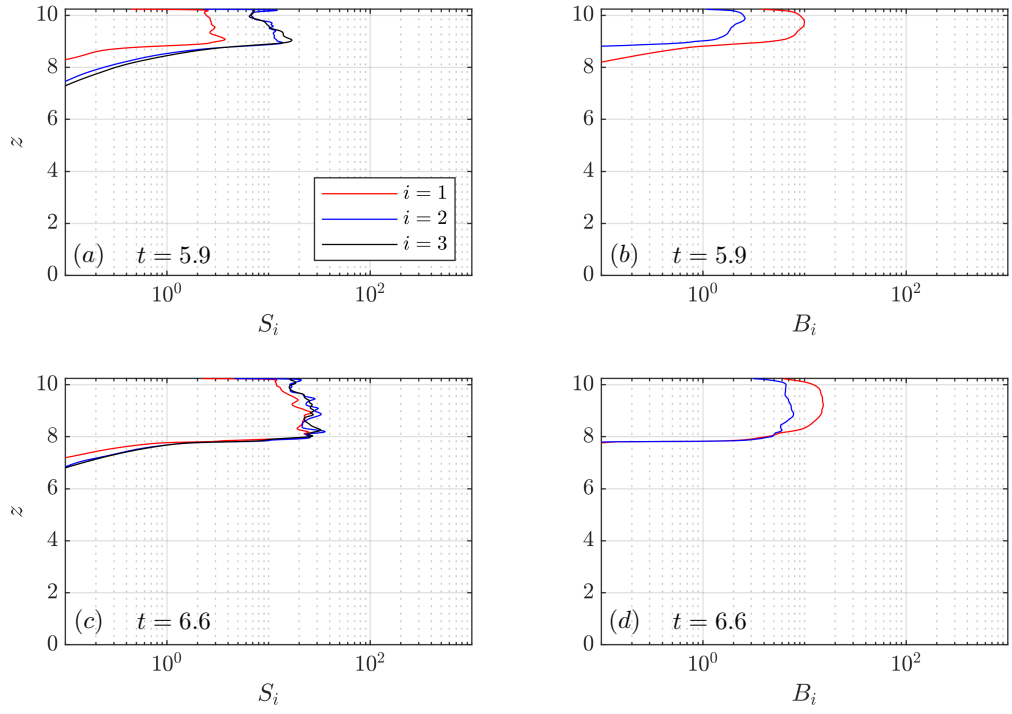

Figure 3.14: Panel (a) shows profiles of the horizontal L^2 norm of each component of vortex tilting/stretching for the Short-Attenuation case at $t = 5.9$. Panel (b) shows the horizontal L^2 norm of each component of the baroclinic vorticity production at $t = 5.9$ for the same case. Panels (c) and (d) show the same quantities but at $t = 6.6$.

3.9 Discussion

This thesis chapter (and the paper it is based on (Grace et al., 2022)) presents three-dimensional simulations of cold water ($T < T_{md}$) convection induced by volumetric thermal forcing in the presence of a subsurface current in a horizontally periodic rectangular prism. In this temperature regime, density differences, characterized by the Atwood number, achieved within the flow are often much smaller than other studies citing low Atwood numbers (Boffetta et al., 2009, 2010; Andrews and Dalziel, 2010; Akula et al., 2013). The incident thermal forcing is a simplified model of solar radiation akin to Bouffard and Wüest (2019); Ulloa et al. (2019); Ramón et al. (2021), and the background current is approximately linearly increasing from the mid-depth to the surface creating a region of constant shear and motionless region below. In this setup, heat is preferentially added to the near surface regions of the water column resulting in an unstable stratification, with the rate of attenuation of the incident radiation being controlled by ℓ.

Rayleigh-Taylor instabilities develop in all cases, but in cases with sufficiently strong shear, the background shear flow suppresses streamwise variation in the instabilities. The physical length scales of the instabilities that appear tend to correlate with the attenuation length. Cases with smaller attenuation lengths transition to a three-dimensional state earlier than cases with larger attenuation lengths.

All cases exhibited some degree of streamwise variability in the spatial structure of the instability but the variation was much stronger in the Base case and the Slow case. Whether or not the instabilities initially grow in a full three-dimensional state or a quasi-two dimensional state is complicated by the fact that the background density profile is constantly changing. The criterion for determining if streamwise RTI will be suppressed (Mikhailenko et al., 2005) is rewritten here for convenience:

$$|\tilde{U}_z(z)| \geq \frac{\tilde{\sigma}_i}{\sqrt{2}}. \tag{3.58}$$

Here, $|\tilde{U}_z|$ is the dimensional local magnitude of the shear, and $\tilde{\sigma}_i$ is the dimensional growth rate of the fastest growing instability in the absence of any background shear. In this setup, heat is continually added to the domain, and prior to instability formation, this heat modifies the stratification, which in turn modifies both the length scale of the fastest growing instability and the growth rate of instability. The background state in the Slow case quickly reaches a point where $\tilde{\sigma}_i/\sqrt{2} > |\tilde{U}_z|$, and this happens before significant modification of the background state and growth of the instability to its finite sized manifestation. Thus, when the perturbations finally grow, the shear that they experience is not strong enough to

enforce the quasi-two-dimensional instability growth. Contrast this to the Fast case, where the shear is ten times as strong, and instability occurs before $\tilde{\sigma}_i/\sqrt{2}$ becomes larger than $|\tilde{U}_z|$. Therefore, instabilities grow to finite amplitude in a quasi-two dimensional state.

For large enough attenuation lengths (the Fast and Medium-Attenuation cases), the growth of the convective instabilities induces a vertical flux of streamwise momentum, rapidly increasing the spanwise and vertical components of vorticity (refer to figure 3.10, panel (c)). The rapid increase triggers three-dimensional tilting/stretching of vorticity, which finally allows the instabilities to go from a quasi-two dimensional structure to a fully three-dimensional turbulent state. The Short-attenuation case exhibited qualitatively similar behaviour (refer to figure 3.11 panel (c)), but the baroclinic generation of vorticity was slightly stronger as the system transitioned from the quasi-two-dimensional state to the full three-dimensional one. The increased baroclinic production comes from the fact that the length scales between the plumes are much smaller in the Short-Attenuation case, allowing for higher horizontal density and velocity gradients leading to streamwise vorticity generation. This is evident in the fact that for the Short-Attenuation case, values of $\bar{\omega}_x^2$ are higher than values of $\bar{\omega}_z^2$ for much of the evolution.

The results of this chapter also bring up an important question about what one sees when simulating planar convection with a background shear flow (convection in only the $x-z$ plane). For instance, in Benilov et al. (2002), planar convection is seen as a reasonable representation of the full three dimensional physics, but by limiting the simulations to a single plane, the key mechanism responsible for three-dimensionalization and mixing is missing. When performing similar simulations to those in table 3.2, except limiting the domain to the $x-z$ plane, the background shear flow completely stabilizes the upper portion of the water column. Convective heat fluxes are temporarily (and in some cases indefinitely) stopped within the domain, leading to a cooler lower layer relative to a run without a shear flow. The cases discussed in Benilov et al. (2002) suffer from this behaviour, as there is no mechanism for the background state to become more unstable, thus eventually being able to overcome the stabilizing effects of the shear.

Building an understanding of the dynamical processes that are responsible for the transition from instability growth to turbulent convection in cold water is important for the eventual parameterization of these processes for larger scale models. The heat added to the system generates upwelling and downwelling and an associated momentum transfer that in turn disrupts the background shear flow. As was shown in the Results section, the mechanism by which the system goes unstable was shown to be intimately linked to the presence of the shear flow. More research is needed to investigate the long term impact of the instability collapse and resultant turbulence on the background current. For example, once the system is in a turbulent state, is there some sort of equilibrium, or slowly varying

but predictable background state that is achieved after enough time? Additionally, what does the turbulent state look like as the attenuation length is varied? In the limit of $\ell/H \to 0$, the system approaches a Rayleigh-Bénard type of convection system. Pirozzoli et al. (2017) simulated the interaction of this form of convection with mean shear and identified robust streamwise rollers that increased the efficiency of the downward heat flux. Bouillaut et al. (2019) used an experimental setup similar to the one presented in the present chapter. They heated a tank of freshwater from the bottom and measured the convective heat flux as a function of the Rayleigh number and ℓ/H and found that at larger ℓ/H, the upward heat flux was more efficient than for smaller values of ℓ/H, indicating that volumetric thermal forcing may be able to achieve the so-called "ultimate regime" of convection under the right conditions.

The results in this chapter also highlight a gap in the understanding of turbulence generated by unstable stratification. As an example, consider the K-Profile Parameterization (KPP) (Large et al., 1994), a more modern review of which is found in Van Roekel et al. (2018). The KPP is a mixed layer model, with a term that parameterizes non-local turbulence based on boundary fluxes of heat and salt. Since radiation from the sun is a volumetric heating mechanism rather than a boundary flux, it is not clear how much solar radiation should be included in the non-local term (Van Roekel et al., 2018), thus a separate parameterization for mixing in cold water by radiation may be needed. Furthermore, the parameterizations within the KPP are built on theories which rely on the presence of fully developed turbulence. It is interesting to note that the flow Reynolds numbers of the above simulations are quite low, indicating that the simulations may not reach a point where they could be considered as fully developed turbulence by models like the KPP. Low Reynolds numbers could indicate that the inertial sub-range of the kinetic energy spectra (Kundu, 1990) where vortex tilting and stretching typically dominate, may not be fully formed. However, it is clear from figures 3.12, 3.13, and 3.14 that stretching and tilting are still important to the development of the system.

Furthermore, future work should include a demonstration and discussion of the dynamics of a similar system where the background shear current is located near the bottom of the domain, as opposed to near the surface. This setup provides a companion to the simulations presented in this chapter. With a current located near the bottom, convective instabilities are free to form in three dimensions near the surface, and they can collapse and then contact the shear flow. Can the instabilities move momentum from the shear layer to the near surface region? Is this momentum flux more efficient once the instabilities collapse, or prior to collapse? Do fully three dimensional instabilities become two dimensional when they are subjected to the shear in this setup on long enough timescales?

Another direction one could consider is the impact of a different shear profile. One

key feature that is ignored in this chapter is an inflection point in the background velocity profile. An inflection point is a necessary condition for the development of shear instabilities by Rayleigh's inflection point criterion (Kundu, 1990). Shear instabilities provide another mechanism to mix the water column (Caulfield, 2021), and depending on the strength of the shear, these shear instabilities may grow faster than any convective instabilities. Once in a turbulent mixed state, does the hypothetical system generated by shear instabilities differ from a turbulence point of view when compared to the system presented in this chapter?

Chapter 4

Asymmetries in gravity currents attributed to the nonlinear equation of state

4.1 Author's Note

This chapter is a slight modification of the material that appeared as Grace et al. (2021). A discussion on how the non-dimensional parameters in the cubic equation of state used in this chapter relate to the NLEOS parameter discussed in the previous two chapters has been included.

4.2 Introduction and Overview

This chapter concerns itself with a larger but still monotonic interval of the NLEOS relative to the results and analysis of chapter 3. For a visual representation, refer back to figure 1.3(b). In this chapter, characteristic temperatures fall between the freshwater freezing point and the freshwater temperature of maximum density $\tilde{T}_{md}$. We will call this regime the "cold water regime". As mentioned in chapter 1, to examine this interval of the NLEOS, the specific flow phenomenon we will focus on is a gravity current. For a brief overview of gravity currents in previous studies, refer to section 1.1. In brief, gravity currents provide a canonical example of density driven flow and have often been used in numerical and laboratory scale studies to represent much larger scale phenomena. Simpson

(1982, 1999) and Huppert (2006) provide an overview of the history, theory, and practical applications of gravity currents in the laboratory and environment. For numerical analysis on the coexistence of coherent structures and turbulence, see Härtel et al. (2000a,b); Ouillon et al. (2019). With respect to the NLEOS, gravity currents have the benefit that one can control the interval of interest of the NLEOS by specifying appropriate initial conditions. This includes choosing an ambient temperature $\tilde{T}_a$ and intruding temperature $\tilde{T}_i$, and forming an *a priori* temperature difference $\Delta\tilde{T}$. This differs from the internally heated convection system in chapter 3, where an initial condition was specified, and the characteristic temperature difference was controlled by the intensity of the radiation and was a function of time.

An analogy of gravity currents in the cold water regime can be made to the ice pump mechanism beneath the Pine Island Glacier ice shelf in West Antarctica (Schoof, 2010). Autonomous underwater vehicle data from Jenkins et al. (2010) shows that warm and salty circumpolar deep water slips into a trough in the continental shelf and flows down into the cavity between the continental shelf and glacier. Once this water mass makes contact with the ice shelf, mixing and basal melting occur forming buoyant ice shelf water that flows upwards along the ice shelf (Schoof, 2010). This process has been identified as a possible mechanism responsible for the accelerated retreat of the Pine Island Glacier.

Near the Pine Island Glacier ice shelf, Walker et al. (2007) measured the salinity to be between 33 PSU and 35 PSU and temperature to be between -2°C and 1.5°C. In this regime, the density varies linearly with salinity, while simultaneously varying non-linearly with temperature. These observations suggest that density driven flows similar to gravity currents exist in regions where the equation of state is non-linear. Understanding the small scale processes that lead to increased melting in places like the Pine Island Glacier ice shelf is imperative to accurately projecting future sea-level rises resulting from enhanced glacier retreat.

Another example of cold water density driven flows comes from the study of the thermal structure of proglacial lakes, which are lakes found adjacent to glaciers. Several prototypical examples of these lakes can be found in the review by Carrivick and Tweed (2013). Proglacial lakes are primarily fed from meltwater originating from the adjacent glaciers and have a number of influences on the ice dynamics of the glacier, as well as influences on the local and regional climate. Proglacial lakes also act as fluvial sediment traps, meaning that sediment fluxes from glaciers are trapped in these lakes as runoff mixes with the ambient lake water (Carrivick and Tweed, 2013).

The characterization for the thermal structure of proglacial lakes is site specific due to the variation in their characteristics, so consider Bridge Lake (Lillooet Icefield, British

Columbia, Canada) where detailed data on the thermal structure is available (Bird et al., 2022). Over the months of July, August and September in 2013, the thermal structure of the lake at several locations of varying proximity to calved icebergs was measured. The temperatures in the measured parts of the lake remained below $\tilde{T}_{md}$. Bird et al. (2022) found that near the icebergs, the water column was isothermal over the depth (save for the very near surface region which was warmer due to incident thermal radiation during the daytime). Moving further away from the iceberg, a clear stable thermal stratification formed, where waters near the bottom were around 2-3 °C, and the temperature decreased as the surface was approached (again, save for the very near surface region that was warmer due to incident thermal radiation). Moving further still, the water column achieved a warmer isothermal state.

Bird et al. (2022) hypothesized that meltwater at a temperature of 0°C (which was less dense than ambient water) flowed upward along iceberg margins and away from the iceberg once it reached the surface, and this was driven by the density difference between the meltwater and the ambient. This example of a cold water density driven flow is important because is led to a thermal stratification and limited proximal warming near the iceberg.

This chapter presents a series of numerical simulations of two categories of freshwater gravity currents with temperatures restricted to the cold water regime. The first category consists of cool intrusions propagating into warmer denser ambients, and the second category consists of warm intrusions propagating into cooler lighter ambients. The results highlight the temporal and spatial differences between the two categories, and how the mechanism responsible for these differences can be attributed to the NLEOS. The remainder of this chapter is organized as follows. Section 4.3 shows the equations of motion, and defines the non-dimensional equation of state for each category of current, demonstrating how the dominant terms in the NLEOS change depending on which category of current is considered. Section 4.4 highlights phenomenological NLEOS effects, specifically how idealized density distributions change for each category of current. Following this, section 4.5 shows simulations of freshwater gravity currents at varying Grashof numbers in the cold water temperature regime. Lastly, section 4.6 concludes with a summary and discussion of the results and how they may relate to cabbeling with a look ahead to chapter 5.

4.3 Governing Equations and Model setup

In this chapter we use the Spectral Parallel Incompressible Navier-Stokes Solver (SPINS) (Subich et al., 2013) to simulate the evolution of various gravity currents with a charac-

teristic temperature and density of $\tilde{T}_i$ and $\rho(\tilde{T}_i)$ propagating into a motionless ambient of temperature and density $\tilde{T}_a$ and $\tilde{\rho}(\tilde{T}_a)$ in freshwater in two dimensions. The boundary conditions are free-slip for velocity and no-flux for temperature and the model achieves spectral accuracy. Previous studies have used SPINS to simulate the formation and propagation of gravity currents in numerous circumstances; Xu et al. (2016) and Xu and Stastna (2020) being two recent examples. The length of the domain is $L = 20$m and the height is $H = 2$m. The number of grid points in the horizontal and vertical directions are $N_x = 8192$ and $N_z = 512$ respectively, and are uniformly spaced. The grid spacing is approximately $\Delta x = 2.4 \times 10^{-3}$m in the horizontal and $\Delta z = 3.9 \times 10^{-3}$m in the vertical. The equation of state used in the model is a cubic fit from Brydon et al. (1999) modified so that the temperature of maximum density coincides with 4°C. In dimensional form (variables with a tilde are dimensional quantities), it is

$$\tilde{\rho}(\tilde{T}) = c_0 + c_1\tilde{T} + c_2\tilde{T}^2 + c_3\tilde{T}^3. \tag{4.1}$$

The values for c_0, c_1, c_2, and c_3 can be found in table 4.1 and values for $\tilde{T}_i$, $\tilde{\rho}(\tilde{T}_i)$, $\tilde{T}_a$ and $\tilde{\rho}(\tilde{T}_a)$ can be found in table 4.2. The temperature field is scaled as

$$T = \frac{\tilde{T} - \tilde{T}_a}{\Delta\tilde{T}} \tag{4.2}$$

with $\Delta\tilde{T} = \tilde{T}_i - \tilde{T}_a$ and the density field is scaled as

$$\rho = \frac{\tilde{\rho} - \tilde{\rho}(\tilde{T}_a)}{\Delta\tilde{\rho}} \tag{4.3}$$

where $\Delta\tilde{\rho} = \tilde{\rho}(\tilde{T}_i) - \tilde{\rho}(\tilde{T}_a)$ is the initial density difference. Both T and ρ take on values between 0 and 1. With the scalings in (4.2) and (4.3), (4.1) can be re-cast as

$$\rho = \mathrm{R}_1 T + \mathrm{R}_2 T^2 + \mathrm{R}_3 T^3 \tag{4.4}$$

where the coefficients are

$$\mathrm{R}_1 = \frac{\tilde{\rho}'(\tilde{T}_a)\Delta\tilde{T}}{\Delta\tilde{\rho}}, \quad \mathrm{R}_2 = \frac{1}{2}\frac{\tilde{\rho}''(\tilde{T}_a)\Delta\tilde{T}^2}{\Delta\tilde{\rho}}, \quad \mathrm{R}_3 = \frac{1}{6}\frac{\tilde{\rho}'''(\tilde{T}_a)\Delta\tilde{T}^3}{\Delta\tilde{\rho}}. \tag{4.5}$$

Prime symbols represent derivatives with respect to temperature. Values of R_1 and R_2 for each case are given in table 4.2 and $\mathrm{R}_3 = 0.0113$ for all cases. The scaling of density takes into account three quantities; the initial temperature difference between the intrusion and the ambient, the initial density difference between the intrusion and the ambient, and the

derivatives of the equation of state around the ambient temperature. Note that for a linear equation of state $R_1 = 1$ while R_2 and R_3 are zero. This is because the thermal expansion coefficient $\tilde{\rho}'(\tilde{T}_a)$ is constant and is equal to $\frac{\Delta\rho}{\Delta\tilde{T}}$.

We can use (4.3) to define a velocity scale and time scale as

$$U_b = \sqrt{g'H}, \quad t_b = \sqrt{\frac{H}{g'}} \tag{4.6}$$

where $g' = g\frac{|\Delta\tilde{\rho}|}{\rho_0}$ is the reduced gravity, ρ_0 is the constant reference density. These values are found in table 4.1. The spatial coordinates, two-dimensional velocity, time, and the dynamic pressure can then be non-dimensionalized as

$$(x, z) = \frac{(\tilde{x}, \tilde{z})}{H}, \quad (u, w) = \frac{(\tilde{u}, \tilde{w})}{U_b}, \quad t = \tilde{t}\sqrt{\frac{g'}{H}}, \quad p = \frac{\tilde{p}}{\rho_0 U_b^2}. \tag{4.7}$$

The initial condition of the temperature field is

$$T(x, z, t = 0) = \frac{1}{2}\left(1 - \tanh\left(\frac{x - x_\ell}{\delta}\right)\right), \tag{4.8}$$

where x_ℓ and δ are the dimensionless lock and transition lengths, which are 0.5 and 0.025 respectively. A schematic of the case with $\tilde{T}_i > \tilde{T}_a$ is provided in figure 4.1.

The scaling discussed above can be used to non-dimensionalize the incompressible Navier-Stokes equations under the Boussinesq approximation. We can define a control parameter called the Grashof number, Gr, the form of which follows Härtel et al. (2000b) as

$$\mathrm{Gr} = \left(\frac{U_b H}{\nu}\right)^2. \tag{4.9}$$

The relative strength of momentum diffusion to temperature diffusion is kept constant across all cases and is measured by the Prandtl number,

$$\mathrm{Pr} = \frac{\nu}{\kappa} = 10. \tag{4.10}$$

This value of the Prandtl number is representative of the value for freshwater near $\tilde{T}_{md}$. Finally, the equations of motion in non-dimensional form are

$$\frac{D\boldsymbol{u}}{Dt} = -\nabla p - \rho\hat{\boldsymbol{k}} + \frac{1}{\sqrt{\mathrm{Gr}}}\nabla^2\boldsymbol{u}, \tag{4.11}$$

$$\frac{DT}{Dt} = \frac{1}{\sqrt{\mathrm{GrPr}^2}}\nabla^2 T, \tag{4.12}$$

$$\nabla \cdot \boldsymbol{u} = 0, \tag{4.13}$$

along with the NLEOS (4.4). The material derivative is represented by $\frac{D}{Dt} = \frac{\partial}{\partial t} + \boldsymbol{u}\cdot\nabla$, the non-dimensional velocity by $\boldsymbol{u}$, time by t, and $\hat{\boldsymbol{k}}$ represents the unit vector in the positive (upwards) z direction.

The values for Gr, viscosity, and diffusivity are given in table 4.2. Case names that contain a T indicate that the gravity current is a cool intrusion ($\tilde{T}_i < \tilde{T}_a$) and flows along the top surface, while those with a B indicate the intrusion is a warm intrusion ($\tilde{T}_i > \tilde{T}_a$) and flows along the bottom surface. A control case is also included, called Control. For this case, the density field was evolved following an equation similar to (4.12), and has an equivalent driving density difference to the T and B cases. Evolving the density directly is equivalent to evolving the gravity current under a linear equation of state. All other flow parameters were unchanged for the control case. The cases in this chapter were chosen to have comparable Grashof numbers of other studies such as Cantero et al. (2007, 2008) and Härtel et al. (2000b). In section 4.5, the Grashof number is modified by changing the value of the viscosity. In order to keep $\mathrm{Pr} = 10$, the thermal diffusivity must was also changed by the same amount. Alternatively, we could have instead modified Gr by varying H across cases. To achieve the Gr in 2B/T and 3B/T, H would need to be reduced by about 66% and 78% relative to the 1B/T cases respectively. Furthermore, to keep the same aspect ratio of the domain, L, δ, and x_ℓ would also need to be reduced by the same amount.

Since the coefficients of (4.4) are functions of the ambient temperature within the domain, there are different leading order terms in the NLEOS for each type of current, and they are based on the relative magnitudes of R_1 and R_2. For example, for cases where $\tilde{T}_a$ is not close to $\tilde{T}_{md}$ (the exact meaning of "close" and "not close" will be discussed in chapter 5), the magnitudes of R_1 and R_2 are generally comparable. We can then write (4.4) as

$$\rho = \mathrm{R}_1 T\left(1 + \frac{\Theta_1}{2}T + \frac{\Theta_2}{6}T^2\right) \tag{4.14}$$

where the NLEOS parameters are

$$\Theta_1 = \frac{\mathrm{R}_2}{\mathrm{R}_1}, \quad \Theta_2 = \frac{\mathrm{R}_3}{\mathrm{R}_1}. \tag{4.15}$$

As per usual, the NLEOS parameters measure the relative magnitude of the non-linear terms in (4.4) relative to the linear one, while R_1 (interpreted as the scaled thermal expansion coefficient) sets the scale for the buoyancy forcing itself. Note that in this formulation, Θ_1 can be positive or negative because R_2 can be of either sign.

Alternatively, for cases where $\tilde{T}_a$ is close to (but not equal to) $\tilde{T}_{md}$, $\mathrm{R}_1 \ll \mathrm{R}_2$. This means that the dominant term in (4.4) is the quadratic term so that the NLEOS becomes

$$\rho = \mathrm{R}_2 T \left(\frac{1}{\Theta_1} + \frac{1}{2} T + \frac{\Theta_2}{6\Theta_1} T^2 \right) \tag{4.16}$$

In this case, Θ_1/Θ_2 measures the relative magnitude of the cubic term in (4.4). In the limit of $\tilde{T}_a = \tilde{T}_{md}$, the Θ_1^{-1} term vanishes because $\mathrm{R}_1 = 0$. In this limit, the coefficient of the last term in the brackets of (4.16) simply reverts to the ratio of R_3 and R_2 because Θ_1 and Θ_2 are no longer finite using the definition in (4.15).

Using the values for R_1 and R_2 from table 4.2 and the constant value $\mathrm{R}_3 = 0.0113$, we can estimate that for the B cases, $\Theta_1 = -0.5028$ and $\Theta_2 = 5.695 \times 10^{-3}$, indicating that the quadratic term of (4.4) is comparable in magnitude to the linear term. Furthermore, the cubic term is negligible compared to both the linear and quadratic term. For the T cases, $\Theta_1 = 42.6460$ and $\Theta_2 = 0.5$. In this case, both Θ_1^{-1} and the cubic term are negligible compared to unity, the NLEOS is quadratic to leading order in these cases. A more general discussion of the expected dynamics for different intervals of the NLEOS parameter will take place in chapter 5.

Parameter Symbol	Value	Dimensions	Description
g	9.81	$\mathrm{m/s^2}$	Acceleration due to gravity
ρ_0	1000	$\mathrm{kg/m^3}$	Constant reference density
c_0	999.865	$\mathrm{kg/m^3}$	NLEOS constant. See (4.1).
c_1	5.84×10^{-2}	$\mathrm{kg/(m^3{}^\circ C)}$	NLEOS constant. See (4.1).
c_2	-7.45×10^{-3}	$\mathrm{kg/(m^3{}^\circ C^2)}$	NLEOS constant. See (4.1).
c_3	3.30×10^{-5}	$\mathrm{kg/(m^3{}^\circ C^3)}$	NLEOS constant. See (4.1).
H	2	m	Depth of domain
L	20	m	Length of domain
$\lvert\Delta\tilde{\rho}\rvert/\rho_0$	4.57×10^{-5}	-	Dimensionless density difference

Table 4.1: List of constants used in this chapter, their values, and a description.

4.4 Phenomenological non-linear equation of state effects

Mentioned in chapter 3, the dynamic implications of the non-linear of equation of state have been discussed in several contexts like salt fingers (Ozgökmen and Esenkov, 1998), and

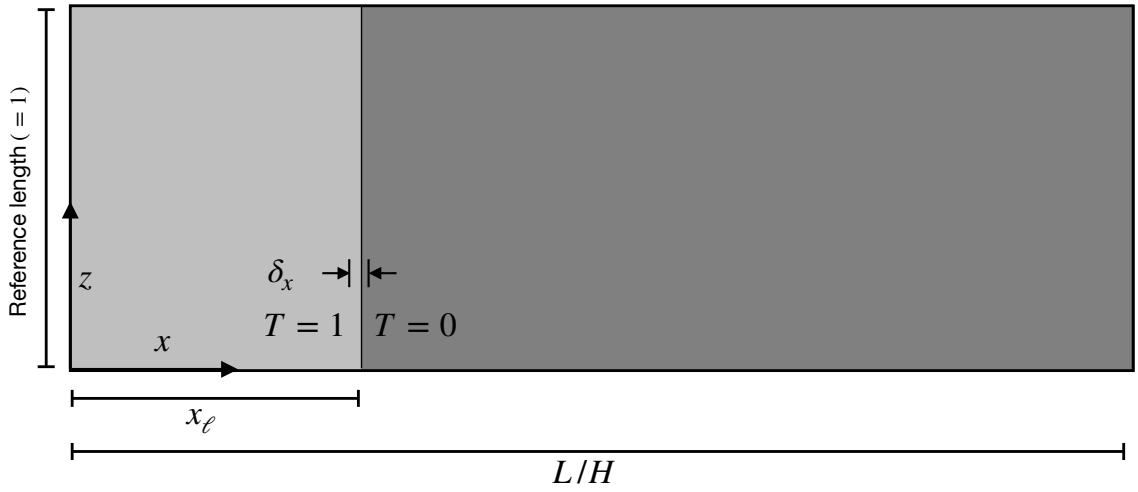

Figure 4.1: A schematic of the initial condition on temperature. $T = 1$ is the dimensionless temperature of intruding fluid while $T = 0$ is the dimensionless temperature of the ambient fluid. In the cool intrusion cases, $\tilde{T}_i < \tilde{T}_a$, and in the warm intrusion cases, $\tilde{T}_i > \tilde{T}_a$. The lock length is given by x_ℓ, the dimensionless tank length given by L/H, and the dimensionless tank height is equal to one (since the reference length is H; the dimensional depth of the tank). x is the horizontal coordinate, and z is the vertical coordinate, and gravity points in the negative z direction.

Case	$\sqrt{\text{Gr}}$	$\nu(\text{m}^2/\text{s})$	$\kappa(\text{m}^2/\text{s})$	$\tilde{T}_i(^\circ\text{C})$	$\tilde{T}_a(^\circ\text{C})$	R_1	R_2
1T	6.0×10^4	10^{-6}	10^{-7}	1.5	4	0.0226	0.9638
1B	6.0×10^4	10^{-6}	10^{-7}	4	1.5	1.9841	-0.9977
2T	1.2×10^4	5×10^{-6}	5×10^{-7}	1.5	4	0.0226	0.9638
2B	1.2×10^4	5×10^{-6}	5×10^{-7}	4	1.5	1.9841	-0.9977
3T	6.0×10^3	10^{-5}	10^{-6}	1.5	4	0.0226	0.9653
3B	6.0×10^3	10^{-5}	10^{-6}	4	1.5	1.9841	-0.9977
Control	1.2×10^4	5×10^{-6}	5×10^{-7}	-	-	1	0

Table 4.2: Outline of the cases in this chapter. T cases indicate cool intrusion, and B cases indicate warm intrusions. The Grashof number is defined in (4.9), ν is the viscosity, κ is the temperature diffusivity, $\tilde{T}_i$ is the intruding temperature, $\tilde{T}_a$ is the ambient temperature, and R_1 and R_2 are defined in (4.5). For the control case, density is evolved directly, so intruding and ambient temperatures are not defined.

Rayleigh-Taylor instabilities (Olsthoorn et al., 2019), but the impacts on freshwater gravity currents remain understudied. As heat is exchanged between the ambient and intrusion their density difference will subsequently decrease assuming the temperatures reside in the monotonic cold water regime between the freezing temperature and $\tilde{T}_{md}$, shown in figure 4.2(a). Figure 4.2(b) shows the dimensionless equations of state that model the density differences between the ambient and the intrusion as their temperature difference decreases. The equations for these equations of state were shown in section 4.3 Initially, the dimensionless temperatures of both currents are $T = 1$. The densities of all B (T) cases are scaled such that the density-temperature relationship is given by the dashed (dotted) curve, called ρ_w (ρ_c).

The two different scalings reveal an important feature about this problem. The rate that the density decreases is strongly dependent on its initial configuration. For cool intruding fluid that gains heat from a much larger volume of ambient fluid at $\tilde{T}_{md}$, the density will initially decrease at a relatively large rate, and as the temperature difference between the intrusion and the ambient approaches zero, the rate of decrease of the density difference will slow. Conversely, for a warm intrusion at or near $\tilde{T}_{md}$ that gives heat to the ambient, the density difference will decrease at a lower rate, until the temperature difference between the masses of water is small. At this point, the density difference begins to decrease more rapidly.

As the gravity current propagates, mixing between ambient and intruding fluids irreversibly modifies the temperature distribution within the flow. The constants in (4.4)

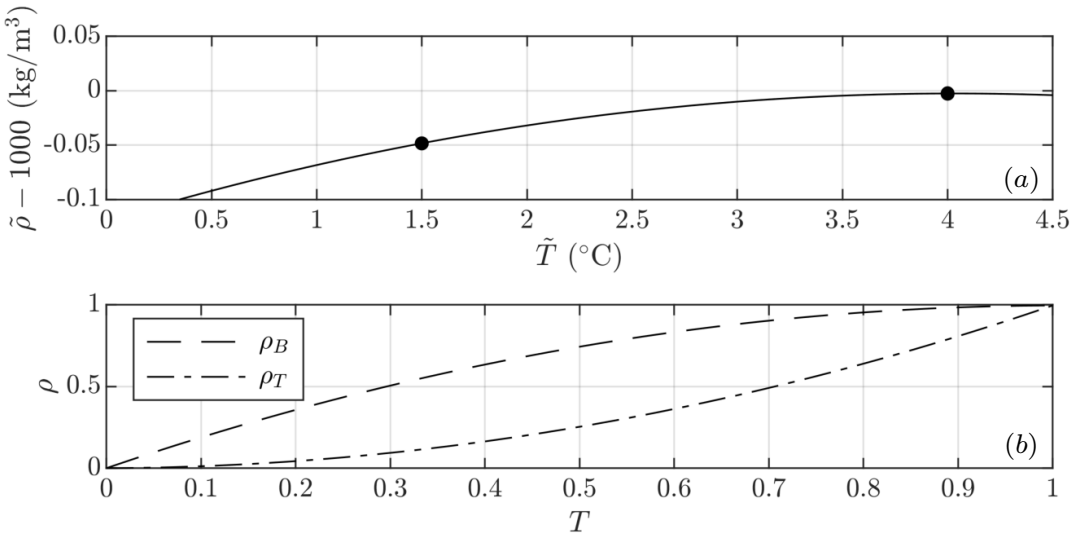

Figure 4.2: Panel (a) shows the equation of state in the temperature regime in this chapter. The temperature of maximum density according to the modified equation of state, (4.1), is approximately 4°C. The black markers indicate the temperature range in this chapter. Panel (b) shows the scaled density-temperature relationships for each set type of current, (4.4). For the T cases, the density initially undergoes a relatively rapid change and slows as the temperature nears zero (depicted by ρ_c), and vice versa for the B cases (depicted by ρ_w).

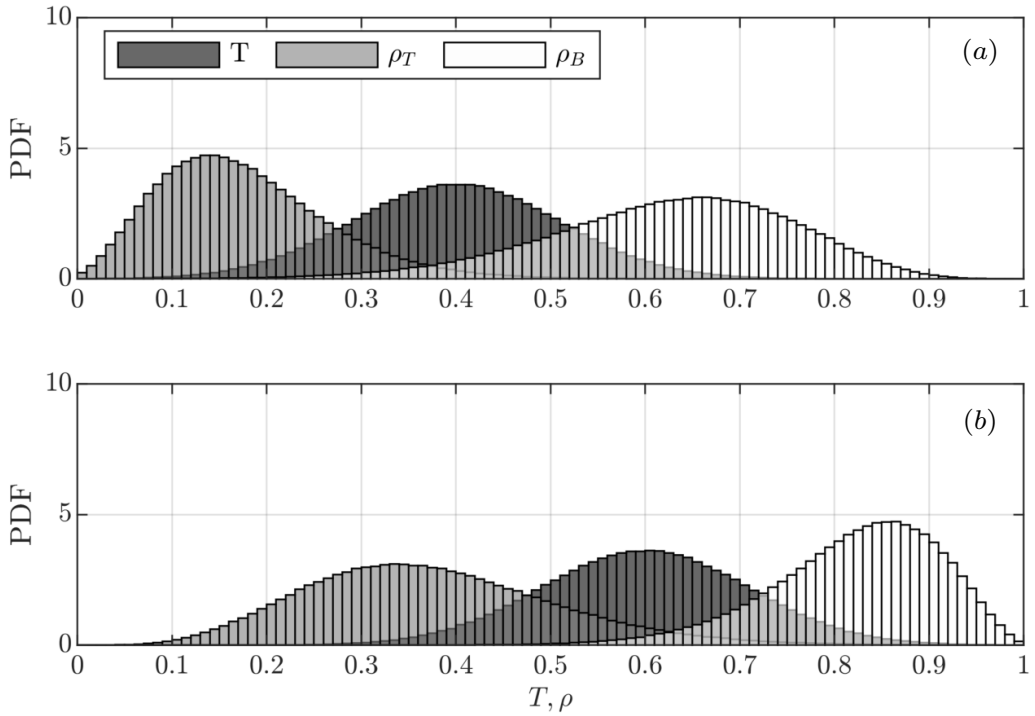

Figure 4.3: A conceptual demonstration of how density distributions with normally distributed temperatures depend on the dimensionless equation of state. Panel (a) shows a temperature distribution with a mean of 0.4, and panel (b) shows a temperature distribution with a mean of 0.6. Standard deviations are constant at 0.11. Refer to legend.

indicate that the resulting density distributions will be different for each type of current. Insight into the relationship between temperature distributions and density distributions can be gained by first considering a test flow with normally distributed temperatures. Since the relationship between T and ρ is nonlinear, the density distribution is not normally distributed. This is illustrated in figure 4.3. In figure 4.3(a), the flow has a mean temperature of $T = 0.4$, and in 4.3(b), it has a mean temperature of $T = 0.6$, each represented by the dark gray probability density functions (PDFs). These distributions were chosen to have standard deviations of 0.11.

When temperatures are distributed such that their mean is closer to $T = 0$ (representing the ambient temperature) than to $T = 1$ (representing the intruding temperature), densities described by $\rho_T(T)$ result in positively skewed and narrow distributions concentrated close to $\rho = 0.15$. Conversely, densities described by $\rho_B(T)$ result in negatively skewed and broad distributions with a peak located near $\rho = 0.65$. When temperatures are distributed such that their mean is closer to the intruding temperature, rather than to the ambient temperature, the opposite behavior occurs. Thus, depending on which equation of state the flow evolves under, the density distributions within the flow are characteristically different. This difference may result in large scale variation in the dynamics of the flows. Since each type of current in this study follows one of either $\rho_B(T)$ or $\rho_T(T)$, the density differences within the flow evolve in different ways. The results in the following sections demonstrate the structural and evolutionary differences that arise due to the characteristic differences between $\rho_B(T)$ and $\rho_T(T)$.

In general, temperature distributions in the simulations in this chapter are more complicated than the idealization in figure 4.3. However, normally distributed temperatures create a simple idealized model that the more complicated distributions presented in Section 4.5 can be compared to, regardless of the exact form of the temperature distribution.

The primary method by which we are going to examine the dynamical significance of the NLEOS in the cold water regime is by comparing gravity currents in two categories. The first category consists of cool intrusions propagating into warmer denser ambients ($\tilde{T}_i < \tilde{T}_a$), and the second category consists of warm intrusions propagating into cooler lighter ambients ($\tilde{T}_i > \tilde{T}_a$).

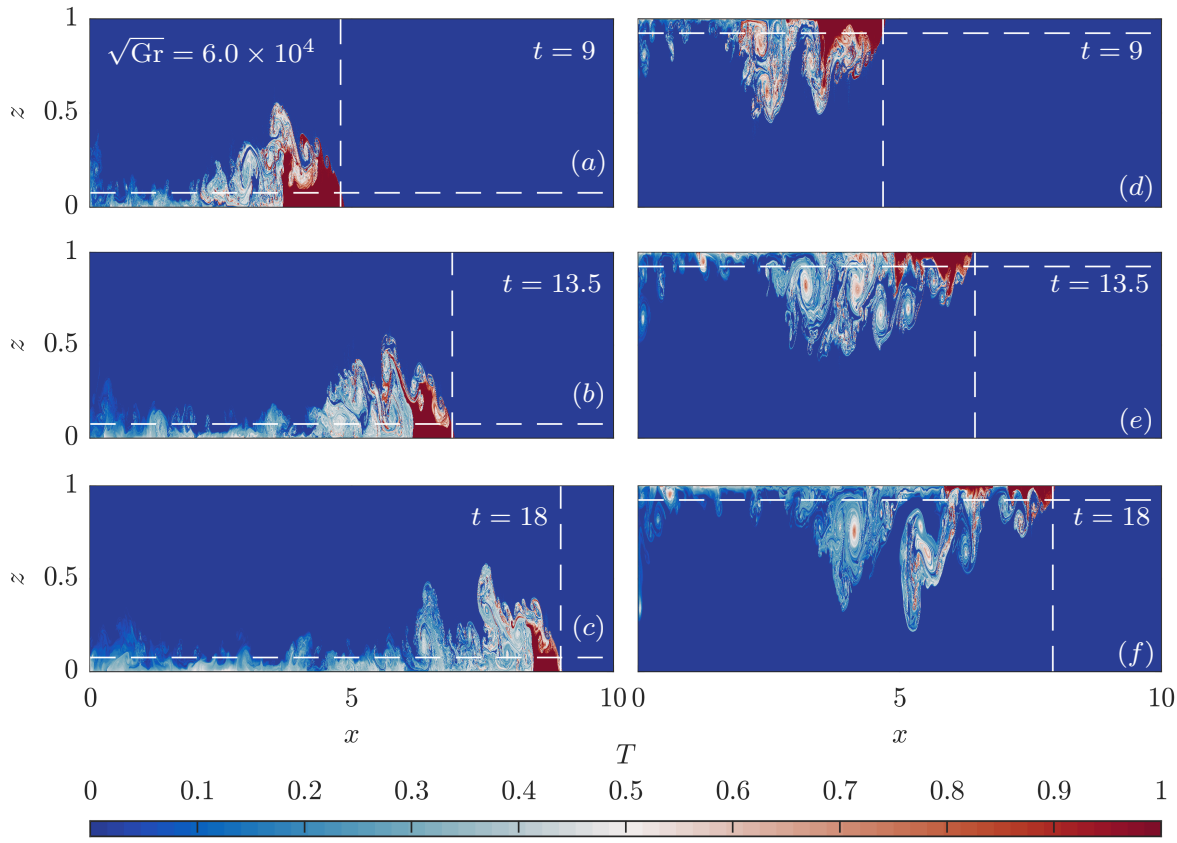

Figure 4.4: Temperature fields for cases 1B ((a), (c), and (e)), and 1T ((b), (d), and (f)). These cases were chosen because it best highlights the qualitative differences between cool and warm intrusions. The dashed vertical lines indicate the location of the nose of the gravity current, while the dashed horizontal lines indicated the critical height where the Froude number becomes insensitive to head height (Huppert and Simpson, 1980)

4.5 Results

4.5.1 Evolution and emergent density changes

The qualitative differences between the cool and warm intrusions are noticeable from a very early stage in their development, and these differences persist as the gravity currents continue to evolve. Shown in figure 4.4 is the dimensionless temperature field for cases 1B on the left, and 1T on the right. Initially, 4.4(a) and (d) show that the gravity currents are similar in structure but by $t = 13.5$ in (b) and (e), large scale differences between the two cases occur. In case 1T, vortices form in the tail of the current and intrude downwards into the water column, whereas for case 1B, much of the intruding fluid is trapped near the bottom surface, and no clear vortices form. The head of 1T is also smaller than the head of 1B. As 1T continues to propagate, small amounts of fluid are shed from the top surface and brought further into the water column (compare panels (c) and (f)), resulting in a much larger body than in 1B. The temperature fields of the 2B/T and 3B/T cases (not shown) have very similar structures, but they show less spatial variability in the temperature field due to the higher values of viscosity and thermal diffusivity. The 1B/T cases show the most spatial variability because they have the smallest viscosity and thermal diffusivity, and therefore the largest Grashof number considered here.

Distinct differences between the head locations occur as the currents continue to evolve. The difference is most apparent in panels (c) and (f), indicated by the dashed vertical lines. Comparing with the results of the 2B/T and 3B/T cases, the simulations reveal systematic differences in the head locations for all cool intrusions compared to the warm intrusions at the same Gr. Figure 4.5(a) show the head locations for all cases with power law fits to the data, and (b) shows the non-dimensional velocity calculated from the fits. The data from the simulations are plotted as coloured markers and the fits for the B and T cases are plotted as dashed and solid lines respectively. The head location data was fit to Ct^a (a and C are computed coefficients) over an interval of $t \approx 4$ to $t \approx 18$ using MATLAB's polyfit function. The choice of this range of times was motivated from a discussion about self-similar phases of gravity current evolution presented in Cantero et al. (2008). For sufficiently large Grashof number, gravity currents travel through several self-similar phases. They are called the acceleration phase, the slumping phase, the inertial phase, and the viscous phase. In the first three of these phases, the dominant balance in the momentum equation is between the driving pressure gradient generated by density differences, and the inertial term. For the viscous phase, the dominant balance is instead between the viscous term and the inertial term. The record of the head locations begins as about $t \approx 4$, which is the time Cantero et al. (2008) predicts that the transition between

the accelerating phase and the slumping phase occurs. This event is significant because the head height and the current speed attain their maximum values during this regime shift.

The head location for the B cases scale as $\sim t^{0.87}$ across the entire time interval shown. The scaling of the B cases nearly matches the theoretical scaling of Huppert and Simpson (1980) in the slumping phase, who report that the head location scales as $\sim t^{6/7}$ as long as $\phi > 0.075$, where ϕ is the head height of the gravity current. This height is included as horizontal dashed lines in figure 4.4. The T cases scale as $\sim t^{0.8}$. The rate of decrease of the head height is much higher in these cases, even reaching near the critical height 0.075 by $t \approx 18$, which could impact the current head speed. Included in panels (a) and (b) are the head location and head speed for the control case. The results show that the B cases propagate faster than the control case while the T cases propagate slower. The rate at which the head location scales is also very similar to the slumping regime in Huppert and Simpson (1980), $\sim t^{0.83}$.

Figure 4.5(c) shows the difference in head location, $x_B - x_T$, for each pair of cases with the same Gr. x_T represents the location of the T cases, and x_B the B cases. For the 1B/T and the 2B/T cases, the curves are coincident, while the curve for 3B/T shows that the 3T case stays closer relative to the B case during the evolution. A closer examination (not shown) reveals that 3B propagates slightly slower than 1B and 2B, while the 3T moves at a rate more comparable to 1T and 2T. This indicates that decreasing the Grashof number past this threshold affects the relative disparity in the head locations. Cantero et al. (2007) show that gravity currents with a low Grashof number reach a viscously dominated regime much earlier in their evolution than gravity currents with higher Grashof number. Though the 3B/T cases do not formally exhibit a clear transition to this scaling regime in figure 4.5(a), the results from panel (c) indicate that viscosity plays a quantifiable role in the head location for those cases. Time estimates from Cantero et al. (2008) suggest that the viscously dominated regime should occur near the end of our simulations for cases 3B/T, but long after the final simulation time for 1B/T and 2B/T.

A direct comparison of the two types of currents highlights the structural differences that occur as they evolve. To differentiate them further, consider the temperature PDF of case 1B in figure 4.6((a) – (g)), and case 1T in figure 4.6((h) – (n)). The PDFs are shown at several times between $t = 9.1$ and $t = 13.6$. In each panel, the ambient temperature is in the left most bin, while the intruding temperature is in the right most bin. At $t = 9.1$, the PDFs reveal that a broad distribution of intermediate temperatures form because of mixing of ambient and intruding fluids. By $t = 13.6$, the distributions evolve and form peaks centered around $T = 0.38$ in 1B and around $T = 0.3$ in 1T. Additionally, 1B has a relatively narrow distribution of temperatures about its peak at $T = 0.38$, while 1T is more broad. This indicates that more mixing has occurred in 1T. In both cases, there is

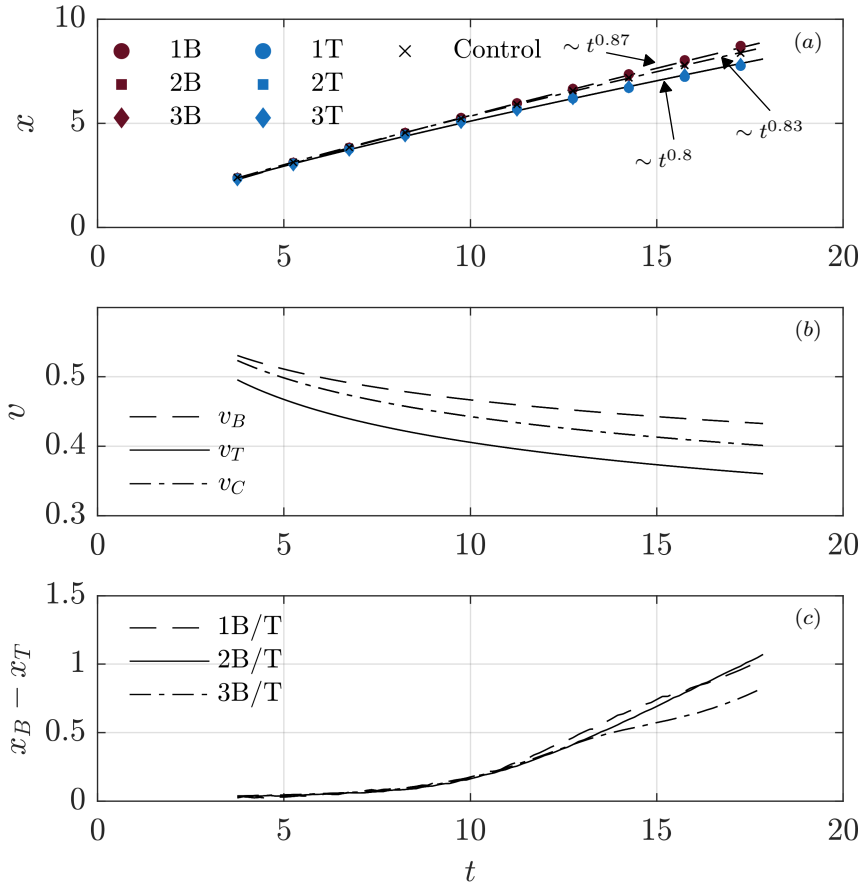

Figure 4.5: Panel (a) shows the head location of each current. Cool intrusions are denoted by blue markers and warm intrusions are denoted by red markers. The solid and dashed lines are power law fits for the cool intrusions and warm intrusions respectively. The Control case is denoted by $\times$ markers and the fit by the dot-dashed line. The power laws are marked on the figure. Panel (b) shows the velocity time series derived from the fits in panel (a). The solid curve is the fit for the cool intrusions, v_T, the dashed curve for the warm intrusions, v_B, and the dot-dashed line for the Control, v_C. Panel (c) shows the the difference in the head location $x_B - x_T$ (x_T is the head location for cool intrusions, and x_B is the head location of warm intrusions) as a function of time between cases with the same Gr. Cases 1B/T are denoted by the dashed line, 2B/T by the solid line, and 3B/T by the dot-dashed line.

a much lower probability of finding temperatures between about 0.6 and 0.95 within the domain. This is due to the much larger volume of ambient fluid.

The regions with temperatures between $T = 0.15$ and $T = 0.5$ (approximately surrounding the peaks in the PDFs in figure 4.6 (h) and (n) where mixing has occurred) in the gravity currents are plotted in figure 4.7. The peak in the intermediate temperatures in the PDFs approximately corresponds to the tail region of the gravity current, with the head being primarily outside this region. It is the tail region where ambient fluid is rapidly mixed with intruding fluid that forms the peak in the PDFs.

The density PDFs for case 1B are shown in figure 4.8((a) – (g)) and case 1T is shown in figure 4.8((h) – (n)) at the same times as the corresponding to figure 4.6. In each panel, the ambient density is in the left most bin, while the intruding density is in the right most bin. Figure 4.8 reveals the wide variations of the density distribution within the two currents. At $t = 9.1$, the density distribution for 1B is broad with a small peak at about $\rho = 0.5$, but for 1T, no such peak is exists and the range of densities in the domain are much closer to the ambient. This is a clear indication of how the NLEOS strongly affects the density distributions of the two currents. By $t = 13.6$, the density PDF for 1B has a clear peak (the tail of the current), while the PDF for 1T shows something completely different. The control case (not shown) has identical temperature and density PDFs due to the linear relationship between them. The density PDF exhibits a wider distribution than 1T, and no peak similar to 1B is evident.

Figure 4.9 shows the densities of the regions depicted in figure 4.7. The temperature bounds used in figure 4.7 translate to about $\rho = 0.02$ and $\rho = 0.25$ for 1T (figure 4.9((a)–(c)) and about $\rho = 0.25$ to $\rho = 0.75$ for 1B (figure 4.9(d) – (f)). The most obvious consequence of the NLEOS is the difference between the densities in the tail of each type of current. For 1B, as fluid travels toward the tail of the current, it mixes with some ambient fluid resulting in a relative density of about 0.6, and the buoyancy force on this fluid is strong enough to draw it back into the current. As fluid travels towards the tail in the 1T case, it mixes with ambient fluid and achieves a relative density that nearly matches the ambient. The buoyancy force on this fluid is not nearly as strong, and this leads to a larger tail.

An analogy to figure 4.3 can be made. As the fluid in the tail region is mixed over the course of the evolution of the current, the temperature distribution is seen to form a peak. As the peak becomes more well defined and closer to the ambient temperature, the density distributions are affected asymmetrically. The warm intrusions flatten with the mean closer to the intruding density, similar to what develops in figure 4.8(a) – (g). The cool intrusions form a peak that is close enough to the ambient density that it blends with

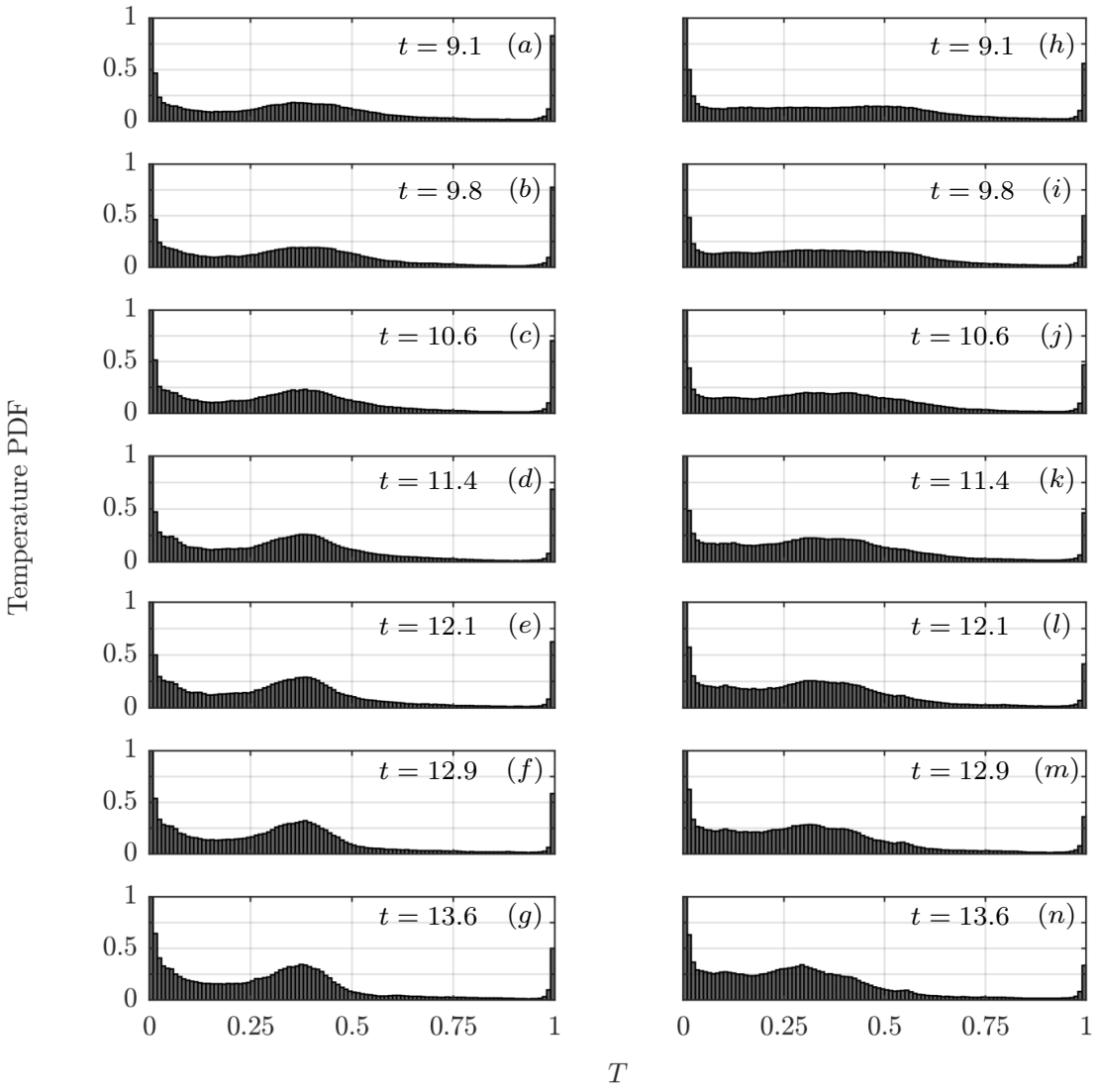

Figure 4.6: PDFs of the non-dimensional temperature for cases 1B((a) – (g)) and 1T((h) – (n)) at successive time intervals, indicated on the plots. The bin width is 0.01, and the vertical axis is capped at 1 to avoid clouding the data. The ambient temperature is located within the left most bin, and the intruding temperature is within the rightmost bin.

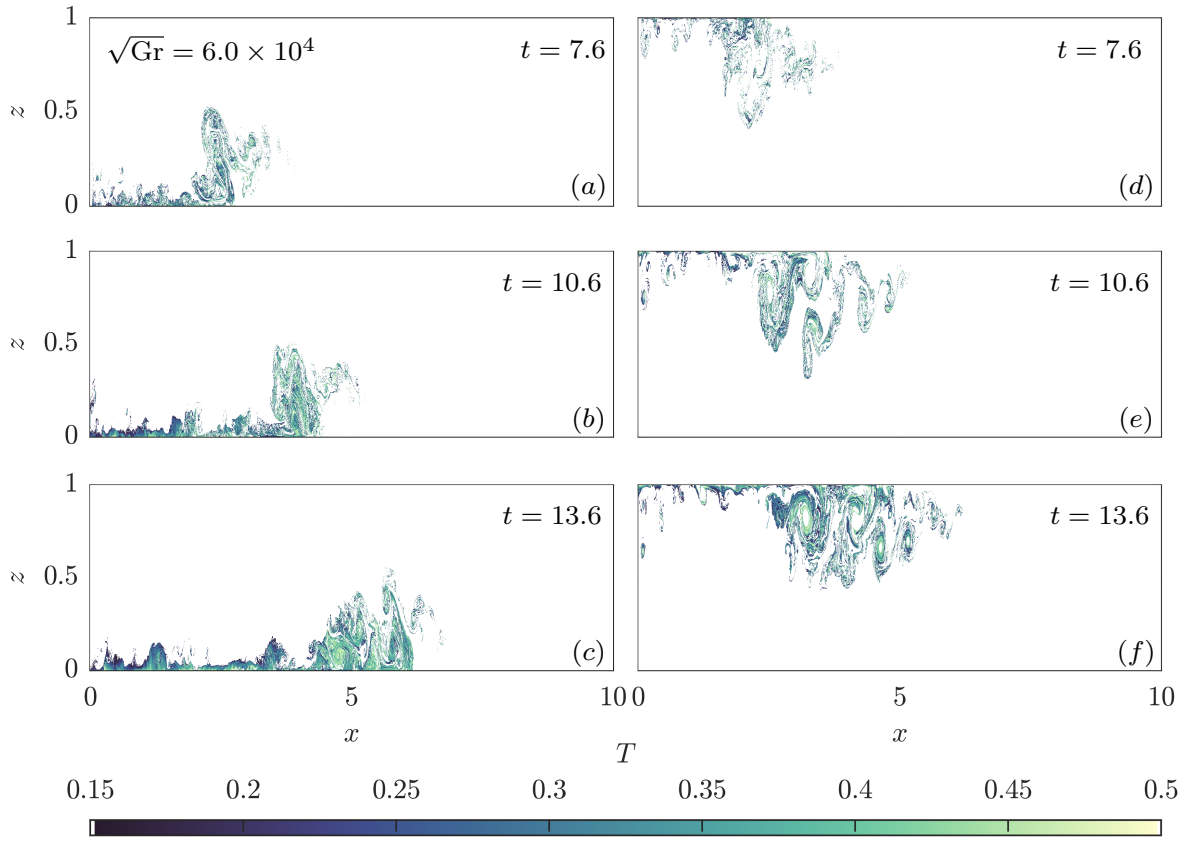

Figure 4.7: Regions of the gravity current where the non-dimensional temperature field varies between $T = 0.15$ and $T = 0.5$. Case 1B is shown in panels (a)–(c), and 1T in panels (d)–(f). Times of the plots are on each panel.

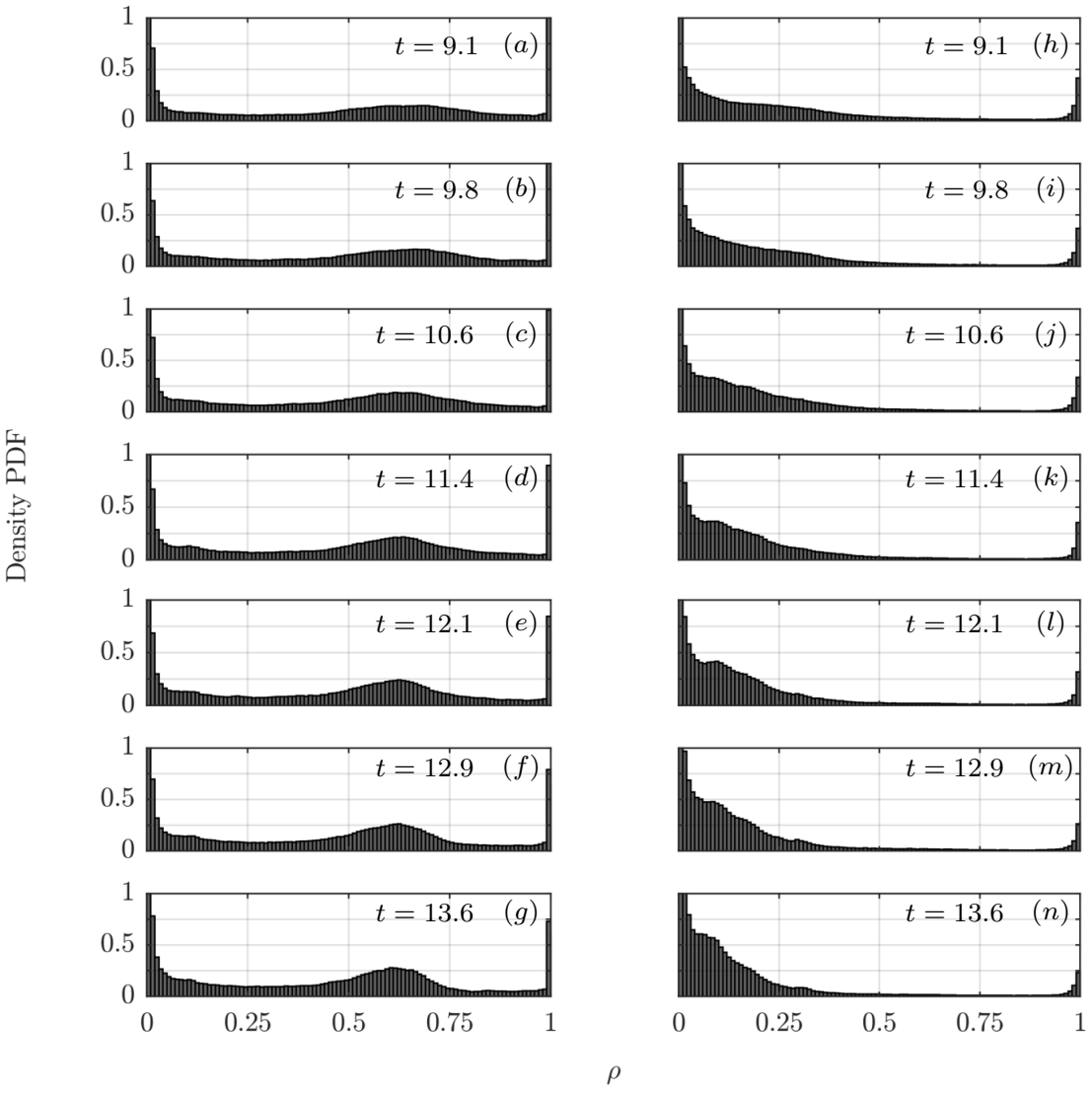

Figure 4.8: PDFs of the density for cases 1B((a) – (g)) and 1T((h) – (n)) at successive time intervals, indicated on the plots. The bin width is 0.01, and the vertical axis is capped at 1 to avoid clouding the data. The ambient density is located within the left most bin, and the intruding density is within the rightmost bin.

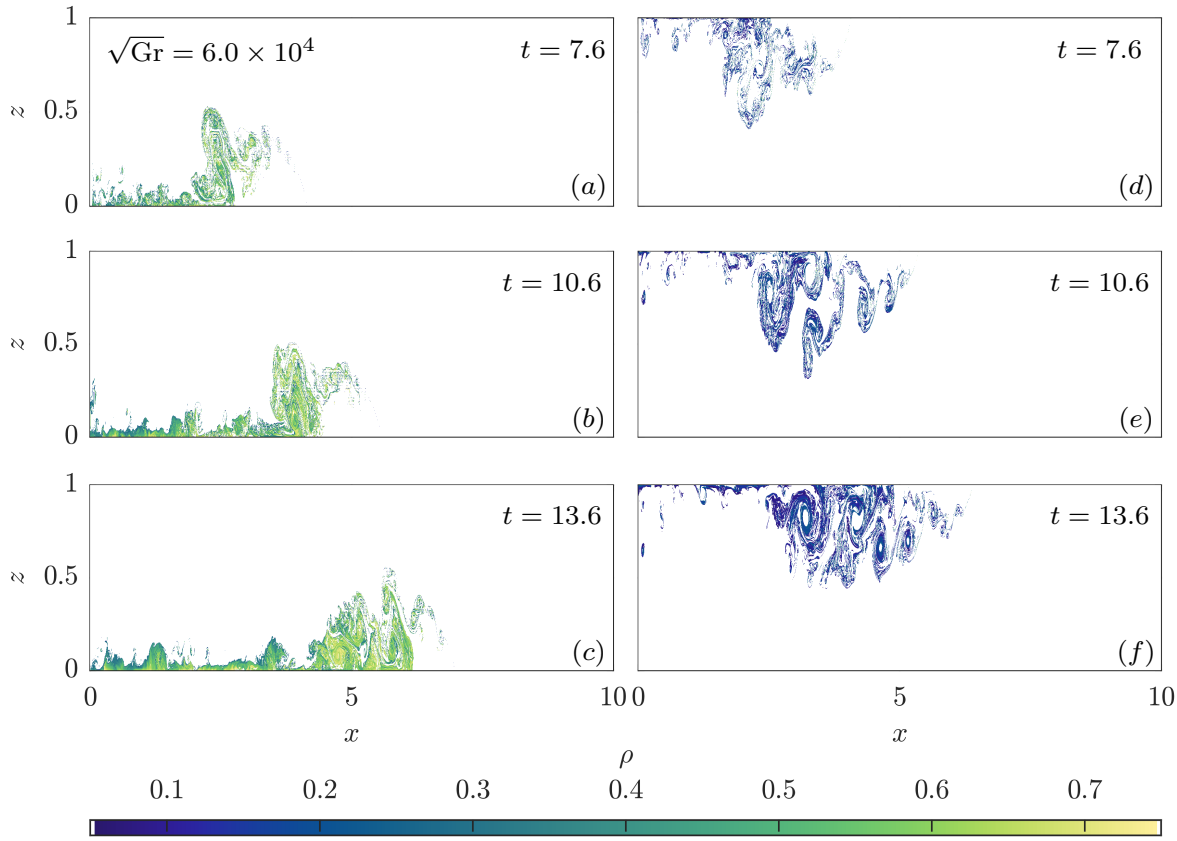

Figure 4.9: Regions of the gravity current where the non-dimensional density field varies between the values prescribed by $T = 0.15$ and $T = 0.5$. Case 1B is shown in panels (a)–(c), where the density values are between $\rho = 0.25$ and $\rho = 0.75$. Case 1T in shown in panels (d)–(f), where the density values are between $\rho = 0.05$ and $\rho = 0.25$. Times of the plots are on each panel.

the temperatures in that part of the distribution. The analogy is not exact because figure 4.3 is an idealization of the current temperature distribution, and ignores the ambient and intruding temperatures. However, as a simple model, it serves the purpose of explaining why there is a stark contrast between the densities fields of the evolving current.

An empirical formulation of the density of the current as a function of its temperature can be determined by defining the phenomenological current temperature, which summarizes the main findings above. Following Cantero et al. (2008), an indicator function is defined as

$$\chi = \begin{cases} 1 & T > T_c \\ 0 & T \leq T_c \end{cases} \tag{4.17}$$

The average temperature of the intrusion is denoted by

$$\Delta T_f = \frac{1}{V} \iint_V \chi T \mathrm{d}x\mathrm{d}z. \tag{4.18}$$

The average temperature of the intrusion is the average temperature of the region of the flow where the temperatures are greater than a cutoff temperature. The cutoff used here is $T_c = 0.01$, which corresponds to all temperatures to the right of the leftmost bin in all panels of figure 4.6. The critical temperature corresponds to $\tilde{T} = 1.525°\mathrm{C}$ for the T cases and $\tilde{T} = 3.975°\mathrm{C}$ for the B cases. These temperatures characterize the currents very well. The average density is defined in a similar way

$$\Delta \rho_f = \frac{1}{V} \iint_V \chi \rho \mathrm{d}x\mathrm{d}z. \tag{4.19}$$

Note that there is an important distinction to be made in this temperature regime. The average density is not equal to the density of the average temperature as it would be under a linear equation of state, so $\Delta\rho_f \neq \rho(\Delta T_f)$.

Plotted in figure 4.10(a) is the average temperature of the current. For all cases, the decrease in ΔT_f follows the same trend, but in cases 1B and 1T it appears to decrease slightly faster, due to the larger Gr. The basic result is that the temperature difference between the ambient and the intrusion does not significantly discriminate between the cool intrusion and warm intrusion across all values of Gr. Figure 4.10(b) shows the average density of the current. It is clear from this plot that the density difference is dependent on whether the intrusion is gaining heat or losing heat, as $\Delta\rho_f$ is smaller for the cool intrusion than for the warm intrusion for $t \gtrsim 6$. This is qualitatively consistent with the hypothesis discussed above (see figure 4.2(b) and related discussion). Shown in panel (c) is the average

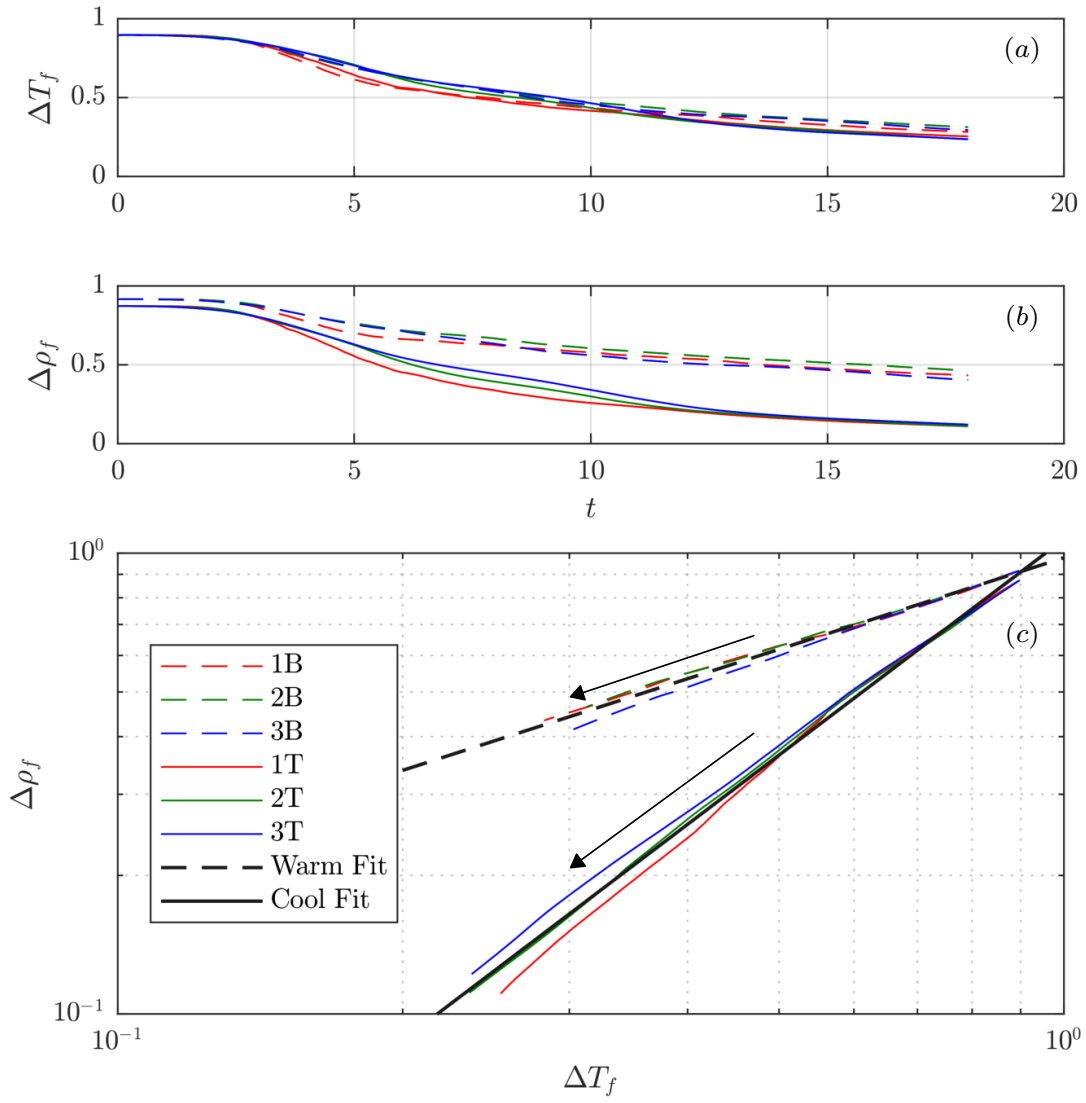

Figure 4.10: Panel (a) shows ΔT_f data for all cases. Panel (b) shows $\Delta \rho_f$ data for all cases. Panel (c) shows $\Delta \rho_f$ plotted against ΔT_f for all cases. Warm intrusions are given by dashed lines and the cool intrusions by solid lines. Fits for each set of currents (warm and cool) are included on the plot. The direction of time for each set of cases in panel (c) is indicated by the arrows.

temperature of the current plotted against the average density. An estimate of the average density of the current can be made by assuming a power law fit to the data

$$\Delta\rho_f \approx A\Delta T_f^{\gamma}. \tag{4.20}$$

For the cool intrusions, $A \approx 1.07$ and $\gamma \approx 1.57$, while for the warm intrusions $A \approx 0.97$ and $\gamma \approx 0.67$.

The constant γ describes the rate at which the average density of the current changes as its average temperature changes. Figure 4.10 demonstrates that the change in density is higher for a given temperature change for the T cases ($\gamma = 1.53$) than it is for the B cases ($\gamma = 0.67$). There is some spread in the data, especially when the temperature differences become small, however, this relationship characterizes the difference between the cool intrusions and warm intrusions well. It is sensible that the rate that the average density changes should be higher for the T cases relative to the B cases because the slope of the NLEOS near $\tilde{T}_i$ for the T cases is larger than near $\tilde{T}_i$ for B cases. Thus, as cool intrusions travel, the relative density change is higher for a given increase in temperature. Conversely, as warm intrusions travel, the relative density change is small as heat is removed from the current.

4.6 Discussion

4.6.1 Implications for gravity current evolution

This chapter presents numerical simulations of two categories of gravity currents in the cold water regime (temperatures less than $\tilde{T}_{md}$). Differences between the categories arise due to the way the fluid density changes as heat is transferred between the intruding and ambient fluids. Warm intrusions near at 4°C undergo a gradual change in density leading to structures more reminiscent of a traditional gravity current. Cool intrusions at 1.5°C undergo an initial rapid change in density, and exhibit more fluid being torn from the current resulting in a qualitatively different body shape and a much smaller head. It is important to note that gravity currents will behave in a similar way when temperatures are greater than $\tilde{T}_{md}$, but close enough that the equation of state is still non-linear.

A consistent feature demonstrated by the numerical experiments is a clear difference in the location of the head of the cool intrusions with respect to the warm intrusions after enough time has elapsed. The head locations for the B and T cases scale differently than each other, and different also to the control case that uses a linear equation of state. A

single power law for each set of cases is adequate to describe this difference. In none of the cases do the velocities exhibit a clear transition from the slumping regime to the inertial regime, as suggested by Huppert and Simpson (1980); Cantero et al. (2007, 2008), even though both the volume of intruding fluid and Grashof number were comparable to the cases of Härtel et al. (2000b), Cantero et al. (2008), and some of the experiments of Huppert and Simpson (1980). The closest approximation to the established scaling laws are the B cases and the control cases having scaling laws close to $\sim t^{6/7}$, which is what Huppert and Simpson (1980) found to characterize the slumping regime.

The lack of agreement between the head location of the control case with the established scaling laws could be a result of the slip boundaries used in this article. Härtel et al. (2000b) discusses effects of no-slip boundaries versus slip boundaries, but does not discuss in detail how the head location differs. Furthermore, the two-dimensional nature of the simulations presented in this chapter removes the ability for the system to fully develop turbulence (since vortex tilting and stretching cannot occur in two dimensions). Cantero et al. (2007) showed that fully developed turbulence enhances the front velocity of gravity currents, and Cantero et al. (2008) supplemented this by showing that two dimensional and three dimensional head speeds agreed only in the acceleration and slumping regimes, while the two-dimensional gravity current head speed was reduced relative to the three-dimensional simulations in the inertial regime (for the same Reynolds number). Cantero et al. (2008) postulated that large coherent vortices formed in the wake of a two-dimensional current which lowered the driving pressure gradient between the current and the ambient. Their claim was that these vortices were not as large and coherent in three-dimensional simulations (due to vortex tilting and stretching), so the driving pressure gradient was not as significantly reduced, leading to a larger head speed. Therefore, a clear avenue to extend the work presented in this thesis is to perform the same experiments in three dimensions to confirm that the results in this chapter are still valid.

The difference in the scaling laws occurs because the non-linear relationship between the driving density difference and the evolving temperature differences affects the evolution of the current in different ways. In the linear regime of the freshwater equation of state, the rate that the density of the current changes is independent of the exact temperatures of the current and the ambient, and is only dependent on their difference. However, in the nonlinear cold water regime, the temperatures of the ambient and the intrusion play a role in how the density will change as the fluids of different temperatures are mixed, depicted graphically in figure 4.2(b), and mathematically by the ambient temperature dependence of R_1, and R_2 (with the cubic equation of state, R_3 remains unchanged for both kinds of currents).

The simulation results above show that at high Grashof number, the temperature dis-

tributions of the two types of currents are initially broadly distributed and tend to sharpen as the current mixes in the tail region, resulting in similar temperature distributions for the 1B and 1T cases. The peak of the temperature distribution tends to be closer to the ambient temperature than intruding temperatures in both cases near the end of the simulations. Figure 4.3 suggests that when the temperature distribution is closer to the ambient temperature, currents that follow ρ_c (the T cases) will have sharper density distributions that tend to be close to the ambient density while currents that follow ρ_w (the B cases) will have flatter density distributions that tend to be closer to the intruding density. The general trend from the simulations agrees with this. For the T cases, as fluid rolls up on the interface between the current and the ambient, it mixes near the tail and attains a density close enough to the ambient that its motion nearly ceases. The net effect is a large tail reaching deep into the water column. Comparatively, the B cases look more like a traditional gravity current because as fluid rolls up and mixes, the density achieved is still far enough away from the ambient that there is still a significant downward buoyant force that returns it into the current.

4.6.2 Insights for cabbeling in shallow bodies of water

Density driven flows in this temperature regime have been previously shown to exhibit downward biases in the vertical exchange of fluids because of the non-linearity in the equation of state. For example, Olsthoorn et al. (2019) showed that downward growing plumes had larger length scales and grew faster than upward growing plumes in numerical simulations of finite thickness Rayleigh-Taylor instabilities. Ozgökmen and Esenkov (1998) demonstrated the same behaviour in the growth of salt fingers. This downward bias is related to the phenomenon known as cabbeling, and the results of this chapter provides insight into how cabbeling could impact the vertical dispersion of intruding fluid in the fresh cold water regime.

Traditionally, cabbeling refers to how two fluid parcels of equal density but different temperatures mix to create a parcel that is denser than both parents (McDougall, 1987). The cold water regime ($\tilde{T} < \tilde{T}_{md}$) precludes mixing between fluid parcels with equal density and different temperatures due to the monotonicity of the equation of state, so a more apt definition provided by Stewart et al. (2017) relates cabbeling to the process of mixing two water masses at different temperatures and forming a mass that is denser than the average of the source densities.

Where cabbeling traditionally generates downward fluxes of momentum and heat due to the formation of dense water (Thomas and Shakespeare, 2015; Shakespeare and Thomas,

2017), the net effect of cabbeling in the cold water regime, termed "weak cabbeling", is to enhance pre-existing downward fluxes of intruding fluid, and to weaken upward fluxes. The results in figure 4.4 demonstrate that for cool intrusions, fine filament structures reach far deeper into the water column, while for the warm intrusions, intruding fluid is confined closer to the bottom surface, unable to rise further up into the water column. This behaviour is in qualitative agreement with the results of both Olsthoorn et al. (2019) and Ozgökmen and Esenkov (1998).

The results of this chapter show that the subtle example of cabbeling created in the cold water regime can have clear impacts on the small scale non-hydrostatic dynamics of gravity currents. Weak cabbeling may even have implications for the vertical fluxes of material at the surface or bottom of a lake, especially near a river outflow, where masses of water are rapidly mixed.

The results presented in section 4.5 beg the question as to how noticeable differences between warm and cool intrusions are as $\Delta\tilde{T}$ (the initial difference in temperature between the ambient and intrusion) becomes small. For example, consider a surface current of 1°C flowing into an ambient of 1.1°C (called C1 for brevity) versus its comparable bottom current of 1.1°C flowing into an ambient of 1°C (called C2 for brevity). Using (4.14) and (4.15), we find $\Theta_1 \approx 10^{-3}$ and $\Theta_2 \approx 10^{-7}$ for both C1 and C2 indicating that the leading order form of (4.14) is $\rho = R_1 T$ (it can be shown that $R_1 \approx 0.11$ for C1 and $R_1 \approx 0.12$ for C2). This indicates that C1 and C2 will be dynamically equivalent (aside from the small variation in R_1 between cases). Generally speaking, we should expect that for small enough $|\Delta\tilde{T}|$, the dominant term in the NLEOS is linear for both surface flowing and bottom flowing currents.

Additionally, we can consider two comparable intrusions with equal $|\Delta\tilde{T}|$, but we can choose different temperature intervals. For example, 1°C flowing into 1.1°C (called C3 for brevity) compared to 3°C flowing into 2.9°C (called C4 for brevity). In can be shown using (4.14) and (4.15) that the dominant term in the NLEOS is linear for both C3 and C4, indicating the same dynamical equivalence discussed for C1 and C2. However it should be noted that as temperatures approach $\tilde{T}_{md}$, $|\Delta\tilde{T}|$ must become versy small since the quadratic term becomes very important in the NLEOS as R_1 becomes close to zero.

Chapter 5

Gravity Currents in the cabbeling regime

5.1 Author's Note

The material presented in this chapter is new and has not been published as of this writing.

5.2 Introduction and Overview

The following chapter aims to complete the tour through the three characteristic intervals of the NLEOS presented in figure 1.3. In the previous chapter, the temperature interval of the NLEOS under consideration had density as a strictly increasing, but non-linear function of temperature. This led to the notion of 'weak cabbeling', the result of which was noticeable differences in the vertical extent and horizontal head location of near-surface flowing gravity currents relative to near-bottom flowing currents for a given magnitude of the initial density difference. Weak cabbeling followed the definition of Stewart et al. (2017) where mixing of two parent parcels of differing density generated a child parcel whose density was greater than the average of the densities of two parent parcels. In the current chapter, the characteristic temperature interval is further extended so that the density of freshwater is non-monotonic. This means that two different water temperatures can have the same density, with the maximum density occurring at a temperature of $\tilde{T}_{md}$. As mentioned in section 1.2.1, the non-monotonic nature of the density leads to the more traditional form of cabbeling, where the mixing of two parent parcels leads to a child parcel

that is denser than both parents, and not simply greater than their average density. As a result, convection occurs and vertical currents are generated leading to a mechanism for downwelling. Refer to section 1.2.1 for some references and background on cabbeling, as well as the present state of its numerical modelling.

In this chapter, we present simulations of the evolution of gravity currents where temperatures of the intrusion and the ambient are on opposite sides of $\tilde{T}_{md}$, leading to cabbeling. The addition of the cabbeling mechanism in this context leads to some interesting and emergent dynamics. We will demonstrate that gravity currents initially flow near the top surface of the domain (called a hypopycnal current), undergo cabbeling induced by mixing, and develop coherent currents that flow near the bottom boundary (called a hyperpycnal current). We analyze the impact of the NLEOS parameter Θ and the non-dimensional depth of the system h (both to be defined below) on the development of the initial hypopycnal current, and its transition to the hyperpycnal current. We will demonstrate that these parameters play an important role in determining the characteristics of the secondary hyperpycnal current, and discuss the implications for the study of the secondary hyperpycnal currents.

The formation of a secondary hyperpycnal current in the context of cold water is not unlike that which occurs as a result of a process in the sediment-laden gravity current literature known as convective sedimentation. In nature, convective sedimentation occurs when a buoyant particle laden inflow (from a river, for example) mixes with denser saline reservoir (the coastal ocean, for instance). While the inflow is initially buoyant, a denser mixture composed of saline water and sediment forms between the fresh and saline layers. This mechanism was hypothesized by Maxworthy (1999). This denser layer generates an unstable stratification that induces convection, bringing the sediment laden layer and interstitial fluid to the bottom (Wells and Dorrell, 2021). Recent laboratory experiments have demonstrated this process in unstratified environments (Davarpanah Jazi and Wells, 2020; Sutherland et al., 2020) and in linearly stratified environments (Snow and Sutherland, 2014).

If the sediment laden layer is dense enough, a secondary hyperpycnal current flows along the bottom. Maxworthy (1999); Snow and Sutherland (2014); Davarpanah Jazi and Wells (2020) have provided laboratory examples where a coherent hyperpycnal current develops. These currents are often called turbidity currents, and they are significant for the transport of material along lake or ocean floors. Wells and Dorrell (2021) presents a modern review of turbulent processes within turbidity currents and discusses some of the geological features that they create and modify. Meiburg and Kneller (2010) discuss the fact that these currents could potentially act as a mechanism for long-distance transport of material from coastal regions to the deep ocean. They also mention that (among other things) the

sediment and material that turbidity currents have transported over the last 10^4 to 10^6 years have formed significant sediment deposits, and through years of compaction, have formed an important class of hydrocarbon reservoirs. Due to their inherently unpredictable initiation processes (earthquakes, landslides, etc), and logistical difficulties with regards to measurement, turbidity currents have been difficult to study in a nature, and much of what we know about them now is based on numerical simulations and laboratory experiments (Wells and Dorrell, 2021).

The analogy between sediment laden gravity currents and cabbeling gravity currents is highlighted because they share some basic characteristics. A schematic of a typical stratification of a sediment laden gravity current shortly after it begins flowing is given in Davarpanah Jazi and Wells (2020) (their figure 2(b)), and a comparable stratification in cold water is given in Hanson et al. (2021) (their figure 3(c)). A schematic of this basic stratification is reproduced in figure 5.1. Figure 5.1(a) shows the initial stratification at $t = 0$ of a typical sediment laden gravity current, and figure 5.1(b) shows the density profile some short time later. Figure 5.1(b) also represents the initial density profile for the cabbeling gravity currents present in this chapter. The key similarity in both of these systems is the maximum density generated at depth, which is surrounded by an otherwise stable stratification.

The key difference between the temporal evolution of these systems is the non-monotonic nature of the NLEOS, as expressed in the gravitational force. The results of Hanson et al. (2021) reveal that a system with a stratification like that in figure 5.1(b) evolves differently depending on whether or not cabbeling occurs. If the temperatures are in the cabbeling temperature regime, then as convection occurs and parcels mix, denser fluid is created which generates more convection and mixing. If temperatures are away from the cabbeling regime, then mixing generates intermediate densities thereby reducing the amount of available potential energy to be transformed to kinetic energy by the buoyancy flux (Winters et al., 1995). For cabbeling, instability led to the production of a dense mass of fluid (fluid within 10% of the initial density jump of the maximum density) that was seen near the bottom of their computational domain. For the non-cabbeling cases an insignificant mass of fluid near the bottom was seen, and this was due to the inefficient mixing.

5.3 Governing Equations and Model setup

This chapter presents an extension of the work of chapter 4 into the cabbeling regime, where the density of water can be non-monotonic (different values of temperature can correspond to the same density). In keeping with chapters 3 and 4, we use SPINS (Subich

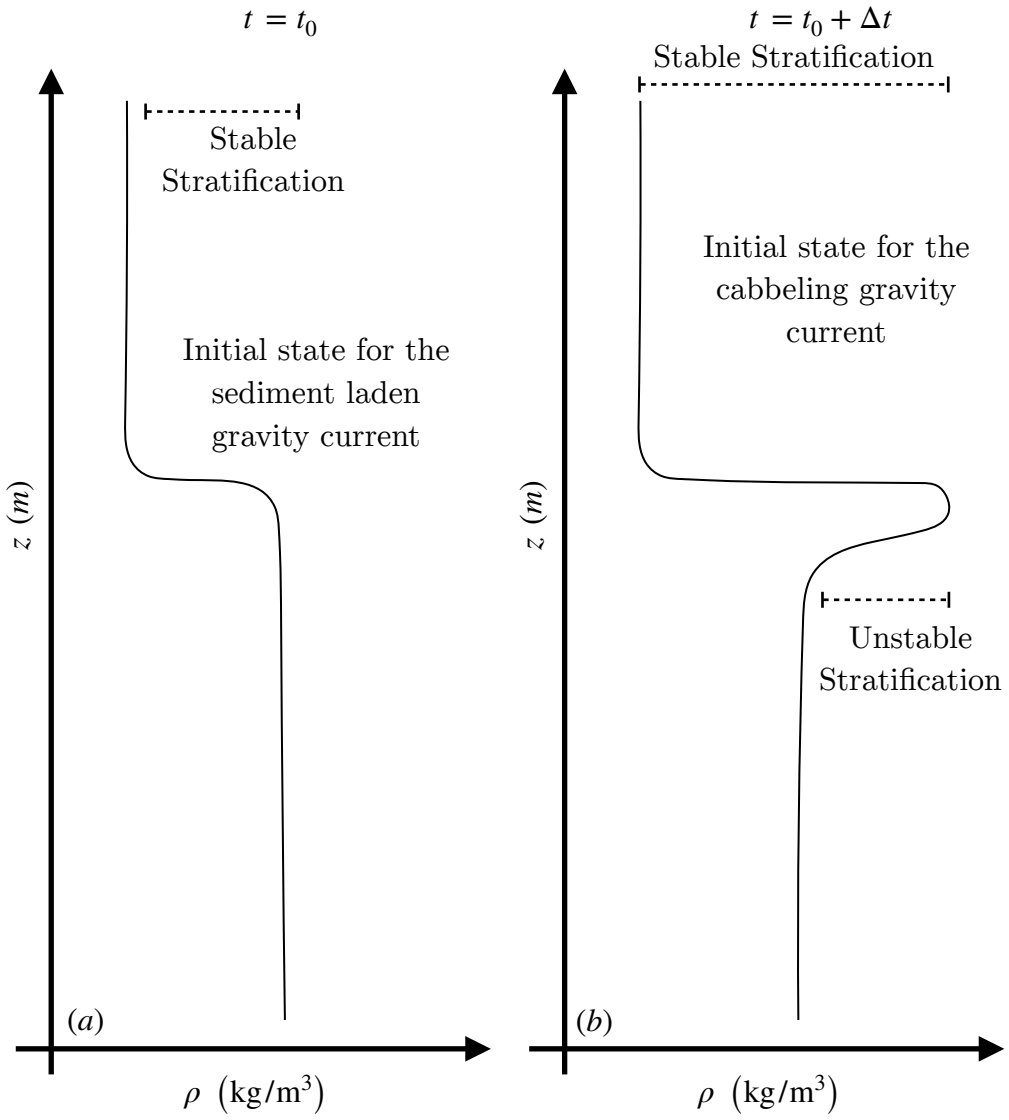

Figure 5.1: A prototypical stratification for sediment laden hypopycnal current with an interstitial layer, as well as for a cabbeling system.

et al., 2013) to simulate the evolution of gravity currents with a characteristic temperature and density of $\tilde{T}_i$ and $\rho(\tilde{T}_i)$ and initial hypopycnal current height of z_0 propagating into a motionless ambient of temperature and density $\tilde{T}_a$ and $\rho(\tilde{T}_a)$ in freshwater in two dimensions. We solve the system of equations in (2.25)-(2.28) (the exact form of (2.28) for this chapter will be discussed below), where we have ignored any external heat fluxes (i.e. $\boldsymbol{q}_{ext} = 0$). The boundary conditions along all surfaces are free-slip for velocity, and no-flux for temperature, and the model achieves spectral accuracy. The motivation of free-slip boundary conditions is twofold. First, in the laboratory experiments of convective sedimentation by Sutherland et al. (2018) and Davarpanah Jazi and Wells (2020), sediment laden gravity currents initially flowed along the free surface (on top of the saline ambient). Furthermore, we are not interested in effects by the boundary layer and are only interested in interior mixing. In this chapter the dimensional length of the domain is $L = 20\,\mathrm{m}$ (table 5.2), and the depth is kept constant at $H = 0.5\,\mathrm{m}$ (table 5.2). All simulations presented have 8192 uniformly spaced grid points in the horizontal dimension and 256 uniformly spaced grid points in the vertical direction, leading to a physical resolution of $(\Delta x, \Delta z) = (0.0024, 0.0020)\,\mathrm{m}$. A resolution sensitivity test was performed and the chosen resolution is adequate to represent the system. In this chapter, variables with a tilde are dimensional quantities.

In this chapter the departure of density from a reference state ρ_0 (table 5.2) is

$$\rho = -C(\tilde{T} - \tilde{T}_{md})^2. \tag{5.1}$$

This equation differs from the previous chapter where the NLEOS was cubic, given by (4.1). The choice to use the quadratic EOS is motivated by the fact it is simpler and has fewer dimensional parameters than (4.1). Note also that (5.1) is the same NLEOS used in chapter 3. As a reminder, (5.1) contains the temperature of maximum density $\tilde{T}_{md}$ and constant C (both found in table 5.2) as parameters. Also note that ρ in (5.1) is already dimensionless.

The temperature field is scaled similarly to that in chapter 4:

$$T = \frac{\tilde{T} - \tilde{T}_a}{\Delta\tilde{T}_1} \tag{5.2}$$

with $\Delta\tilde{T}_1 = \tilde{T}_i - \tilde{T}_a$. Thus, T varies between 0 and 1, and $T = 0$ corresponds to the ambient temperature while $T = 1$ corresponds to the intrusion temperature. We have included the subscript in the definition for $\Delta\tilde{T}_1$ because, as we shall see, this is not the only temperature scale that we must define. We can use the above non-dimensional temperature to non-dimensionalize the density

$$\rho = -C(\Delta\tilde{T}_1 T - (\tilde{T}_{md} - \tilde{T}_a))^2, \tag{5.3}$$

where we can define $\Delta\tilde{T}_2 = \tilde{T}_{md} - \tilde{T}_a$ and the NLEOS parameter as

$$\Theta = \frac{\Delta\tilde{T}_1}{\Delta\tilde{T}_2} = \frac{\tilde{T}_i - \tilde{T}_a}{\tilde{T}_{md} - \tilde{T}_a}. \tag{5.4}$$

Note that the non-dimensional temperature of maximum density is given by $\frac{1}{\Theta}$. Expanding the above quadratic, and noting that $\tilde{\rho}\left(\tilde{T}_a\right) = -C\left(\Delta\tilde{T}_2\right)^2$, we can write the non-dimensional NLEOS as

$$\rho = \rho\left(\tilde{T}_a\right) + 2C\Theta(\Delta\tilde{T}_2)^2 T\left(1 - \frac{\Theta}{2}T\right). \tag{5.5}$$

We can define the buoyancy velocity scale and timescale as

$$U_b = \sqrt{g' z_0}, \quad t_b = \sqrt{\frac{z_0}{g'}}, \tag{5.6}$$

where $g' = g|\rho(\tilde{T}_i) - \rho(\tilde{T}_a)|$ is the reduced gravity, and z_0 is the initial height of the intruding fluid (table 5.3). This differs from the non-dimensionalization from the previous chapter where the characteristic lengthscale was the total depth H. In general the lengthscale used to estimate the buoyancy driven velocity in the study of gravity currents is the initial height of the intrusion. In chapter 4, the initial height of the intrusion was coincident with the total depth H, whereas it is not for the current chapter. We can simplify the reduced gravity to

$$g|\rho(\tilde{T}_i) - \rho(\tilde{T}_a)| = Cg|\Theta(\Theta - 2)|(\Delta\tilde{T}_2)^2, \tag{5.7}$$

allowing us to write

$$U_b = \sqrt{Cg|\Theta(\Theta - 2)|(\Delta\tilde{T}_2)^2 z_0}. \tag{5.8}$$

Using these scales, we can non-dimensionalize the system as

$$(x, z) = \frac{(\tilde{x}, \tilde{z})}{z_0}, \quad (u, w) = \frac{(\tilde{u}, \tilde{w})}{U_b}, \quad t = \tilde{t}\sqrt{\frac{g'}{z_0}}, \quad p = \frac{\tilde{p}}{\rho_0 U_b^2}. \tag{5.9}$$

In this chapter, we have modified the form of initial condition to accommodate different values for height of the initial hypopycnal current z_0. In non-dimensional form, the initial condition for the system is

$$T(x, z, t = 0) = \frac{\mathcal{B}(z)}{2}\left(1 - \tanh\left(\frac{x - x_\ell}{\delta_x}\right)\right), \tag{5.10}$$

where $\mathcal{B}$ is defined as

$$\mathcal{B}(z) = \frac{1}{2}\left(1 + \beta \tanh\left(\frac{z-1}{\delta_z}\right)\right). \tag{5.11}$$

$\mathcal{B}$ allows us to select the initial height of the intruding fluid relative to the top surface ($\alpha = 1$) or the bottom surface ($\beta = -1$). The parameters δ_x, and δ_z are the dimensionless transition thicknesses, while x_ℓ (table 5.2) is the dimensionless lock length. Since all lengths in the problem are scales relative to z_0, the initial intrusion height sets the reference length scale. This is illustrated on figure 5.2. A schematic of the initial condition is provided in figure 5.2. The domain depth and length are also normalized by the intrusion height. They are $h = H/z_0$ and $l = L/z_0$ and their values are found in table 5.3.

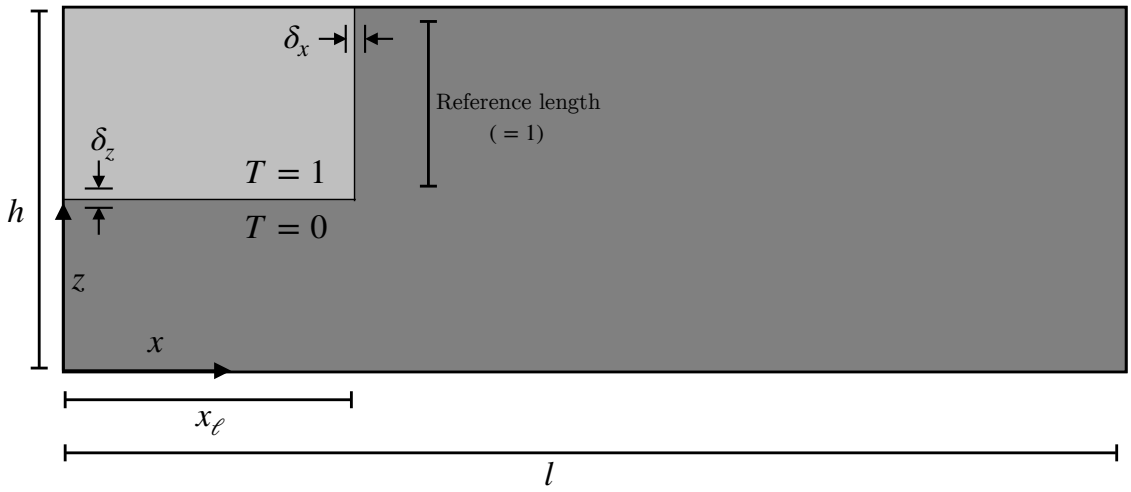

Figure 5.2: A schematic of the initial condition demonstrating the initial locations of the intrusion and ambient, which are defined to have temperatures of one and zero respectively. In all cases, the intrusion is initially located adjacent to the top left corner of the domain. The initial hypopycnal current depth is varied across cases. The lock length is given by x_ℓ, the tank length given by l, and the tank depth given by h. x is the horizontal coordinate, and z is the vertical coordinate, and gravity points in the negative z direction. Lengths are non-dimensionalized by z_0, so the initial intrusion height serves as the reference length.

We can define the Grashof number and the Prandtl number as per usual:

$$\mathrm{Gr} = \left(\frac{U_b z_0}{\nu}\right)^2, \quad \mathrm{Pr} = \frac{\nu}{\kappa}, \tag{5.12}$$

which give the equations of motion as

$$\frac{D\boldsymbol{u}}{Dt} = -\nabla p - \frac{2}{\Theta - 2} T \left(1 - \frac{\Theta}{2} T\right) \hat{\boldsymbol{k}} + \frac{1}{\sqrt{\mathrm{Gr}}} \nabla^2 \boldsymbol{u} \tag{5.13}$$

$$\frac{DT}{Dt} = \frac{1}{\sqrt{\mathrm{GrPr}^2}} \nabla^2 T \tag{5.14}$$

$$\nabla \cdot \boldsymbol{u} = 0. \tag{5.15}$$

Here we can see that Θ plays a similar functional role as the NLEOS parameter in chapter 3 (controlling the relative magnitude of the non-linear term in (5.13)), except in this case, if can attain a much larger range of values that are easily set by the initial conditions $\tilde{T}_i$ and $\tilde{T}_a$. Note that $\Theta = 2$ leads to the case where $U_b = 0$ and there is no longer a buoyancy velocity to scale by. $\Theta = 2$ is special case that must be discussed separately and is done so as a part of the following section.

5.3.1 Gravity Current Classification based on initial intruding and ambient temperatures

Assuming $\Delta\tilde{T}_1 > 0$ ($\tilde{T}_i > \tilde{T}_a$) we can build a framework for the classification of gravity currents based on their Θ value. Note that because of the symmetry of the NLEOS about $\tilde{T}_{md}$, a dynamically equivalent classification can be developed for the case where $\Delta\tilde{T}_1 < 0$ ($\tilde{T}_i < \tilde{T}_a$) using the map $\tilde{T}_i \to 2\tilde{T}_{md} - \tilde{T}_i$ and $\tilde{T}_a \to 2\tilde{T}_{md} - \tilde{T}_a$. Furthermore, an exact NLEOS is slightly asymmetric about $\tilde{T}_{md}$, so currents with $\Delta\tilde{T}_1 < 0$ will not evolve exactly as those with $\Delta\tilde{T}_1 > 0$. This is of no consequence for this thesis because the exact NLEOS is not used here, and differences are expected to be small.

In the following section, we will consider 8 different cases: $\Theta = 1$, $\Theta = -1$, $\Theta < -1$, $\Theta \in (-1, 0^-)$, $\Theta \in (0^+, 1)$, and $\Theta \in (1, 2)$, $\Theta = 2$, and $\Theta > 2$. With this information, we can determine the relative ordering of the intruding temperature, ambient temperature, and temperature of maximum density, and discuss the expected evolution characteristics. The following section goes through each case, but for readers simply interested in a summary, see figure 5.3 and table 5.1. As a reminder, the NLEOS parameter is defined as

$$\Theta = \frac{\Delta\tilde{T}_1}{\Delta\tilde{T}_2} = \frac{\tilde{T}_i - \tilde{T}_a}{\tilde{T}_{md} - \tilde{T}_a} \tag{5.16}$$

$\Theta < -1$

For the case where $\Theta < -1$, $\Delta\tilde{T}_1$ and $\Delta\tilde{T}_2$ must have opposite sign, so when $\Delta\tilde{T}_1 > 0$ and $\Delta\tilde{T}_2 < 0$, we find that

$$\tilde{T}_a < \frac{\tilde{T}_i + \tilde{T}_{md}}{2}, \tag{5.17}$$

and

$$\tilde{T}_i > \tilde{T}_a > \tilde{T}_{md}, \tag{5.18}$$

We can see that this interval of Θ implies that $\tilde{T}_a$ is always closer to $\tilde{T}_{md}$ than it is to the $\tilde{T}_i$. Therefore, as Θ gets more negative, $\tilde{T}_a$ approaches $\tilde{T}_{md}$. Note that this critical value was that which characterized the T cases in chapter 4. This regime is presented in figure 5.3(a).

$\Theta = -1$

In this case $\Delta\tilde{T}_1$ and $\Delta\tilde{T}_2$ must be equal in absolute value but opposite in sign. In this case

$$\tilde{T}_a = \frac{\tilde{T}_i + \tilde{T}_{md}}{2} \tag{5.19}$$

and

$$\tilde{T}_i > \tilde{T}_a > \tilde{T}_{md} \tag{5.20}$$

must be true. This indicates, that for $\Theta = -1$, $\tilde{T}_i$ and $\tilde{T}_a$ are both greater than $\tilde{T}_{md}$ and that $\tilde{T}_a$ must be the average of $\tilde{T}_i$ and $\tilde{T}_{md}$. This case is illustrated in figure 5.3(b). The average of $\tilde{T}_i$ and $\tilde{T}_{md}$ is highlighted by a dotted vertical line.

$\Theta \in (-1, 0^-)$

In the case $\Theta \in (-1, 0^-)$, $\Delta\tilde{T}_1$ and $\Delta\tilde{T}_2$ must have the opposite sign but $\Delta\tilde{T}_1$ must be smaller in absolute value than $\Delta\tilde{T}_2$. In this case

$$\tilde{T}_a > \frac{\tilde{T}_i + \tilde{T}_{md}}{2}. \tag{5.21}$$

Thus, $\tilde{T}_a$ must be greater than the average of $\tilde{T}_i$ and $\tilde{T}_{md}$. Additionally, since $\Delta\tilde{T}_1 > 0$ and $\Delta\tilde{T}_2 < 0$, we must have

$$\tilde{T}_i > \tilde{T}_a > \tilde{T}_{md}. \tag{5.22}$$

We can see that as $\tilde{T}_a$ becomes larger than $\frac{\tilde{T}_i+\tilde{T}_{md}}{2}$, the characteristic temperatures of the gravity current tend to move further away from the non-linearity of the NLEOS. Thus, as $\Theta \to 0^-$, one expects the non-linear term in the NLEOS to become smaller in magnitude relative to the linear term. This case is illustrated in figure 5.3(c).

$\Theta \in (0^+, 1)$

In the interval $\Theta \in (0^+, 1)$, $\Delta\tilde{T}_1$ and $\Delta\tilde{T}_2$ must have the same sign, but $\Delta\tilde{T}_1 < \Delta\tilde{T}_2$. It follows that

$$\tilde{T}_a < \tilde{T}_i < \tilde{T}_{md}. \tag{5.23}$$

Thus, for values $\Theta \in (0^+, 1)$ we have that the intruding temperature is between the temperature of maximum density and the ambient temperatures. In this case, the intrusion is denser than the ambient, so the current will sink. This case is illustrated in figure 5.3(d).

$\Theta = 1$

In this case, $\Delta\tilde{T}_1$ and $\Delta\tilde{T}_2$ must be equal. The only ordering that allows for this is to have $\tilde{T}_i = \tilde{T}_{md}$. Thus, for $\Theta = 1$, the only gravity current class that can exist is one where the intruding fluid is at the temperature of maximum density. In this case, the intrusion is maximally dense, so it sinks. Note that this critical value was that which characterized the B cases in chapter 4. This case is illustrated in figure 5.3(e).

$\Theta > 1$

For the case of $\Theta > 1$, $\Delta\tilde{T}_1$ and $\Delta\tilde{T}_2$ have to be of the same sign and $\Delta\tilde{T}_1 > \Delta\tilde{T}_2$. The ordering then becomes

$$\tilde{T}_i > \tilde{T}_{md} > \tilde{T}_a. \tag{5.24}$$

Thus, the ambient temperature must be less than the temperature of maximum density, while the intruding temperature must be higher. This regime is important because mixing of two parent parcels of fluid generates a parcel that is heavier and sinks. The results dynamics in this interval can be further subdivided into two sub-intervals $\Theta \in (1, 2)$ and $\Theta > 2$. For $\Theta \in (1, 2)$, the density of the intrusion is higher than the ambient, so the intrusion initially sinks. However, as the intrusion and the ambient mix, they form denser water, which in turn has a larger density difference relative to the ambient than the intrusion. Thus, as mixing occurs, a faster moving current may form. For Θ in this interval, it

can be shown that

$$\tilde{T}_{md} < \frac{\tilde{T}_i + \tilde{T}_a}{2}. \tag{5.25}$$

In-depth analysis of $\Theta \in (1, 2)$ is left for future work. This case is illustrated in figure 5.3(f).

If $\Theta = 2$, then the ambient and intruding densities are the same. In terms of $\tilde{T}_i$, $\tilde{T}_a$, and $\tilde{T}_{md}$, we must have

$$\tilde{T}_{md} = \frac{\tilde{T}_i + \tilde{T}_a}{2}. \tag{5.26}$$

In this case, there is no initial collapse and no horizontal intrusion is generated. There is mixing along the interface between the two masses of water that generate vertical currents. This observation is consistent with the scaling U_b, which showed that the current speed would be zero in the event of $\Theta = 2$. In this event, a different velocity scaling should be used. This case is illustrated in figure 5.3(g).

If $\Theta > 2$, then

$$\tilde{T}_{md} < \frac{\tilde{T}_i + \tilde{T}_a}{2} \tag{5.27}$$

In this case, the intruding density is initially lower than the ambient (save for a band of dense water surrounding the initial mass of water), thereby allowing the current to initially rise to the top boundary. As the intrusion propagates and mixes with the ambient water, dense water is created which sinks. The $\Theta > 2$ regime is fascinating and will be the focus of the rest of this chapter In the following sections, we will discuss the dynamics of the $\Theta > 2$ regime specifically highlighting the dynamics as Θ is increased beyond two. This case is illustrated in figure 5.3(h).

An interesting result occurs in the limit of large Θ. Using dimensionless variables now, we can re-write the buoyancy forcing term in (5.13) as

$$\rho = -\frac{2}{1 - \frac{2}{\Theta}} T \left(\frac{1}{\Theta} - \frac{T}{2} \right). \tag{5.28}$$

Letting $\epsilon = \frac{1}{\Theta}$, we arrive at

$$\rho = -\frac{2}{1 - 2\epsilon} T \left(\epsilon - \frac{T}{2} \right). \tag{5.29}$$

In the limit of large Θ (or small ϵ), we can expand the temperature as

$$T = T^{(0)} + \epsilon T^{(1)} + \mathcal{O}(\epsilon^2), \tag{5.30}$$

and substituting (5.30) into (5.29), we find that

$$\rho \approx (T^{(0)})^2 - 2\epsilon\left((T^{(0)})^2 - T^{(0)}\left(1 - T^{(1)}\right)\right) + \mathcal{O}(\epsilon^2). \tag{5.31}$$

Expressing the density as an expansion in ϵ as $\rho = \rho^{(0)} + \epsilon\rho^{(1)} + \mathcal{O}(\epsilon^2)$, we find that

$$\rho^{(0)} = (T^{(0)})^2, \tag{5.32}$$

$$\rho^{(1)} = 2(T^{(0)})^2 - 2T^{(0)}\left(1 - T^{(1)}\right), \tag{5.33}$$

meaning that $\rho^{(0)}$ is a monotonic function of $T^{(0)}$. Since the density is monotonic at leading order, cabbeling becomes a higher order effect (recall that cabbling occurs because of the non-montonic nature of the NLEOS). Ignoring terms of $\mathcal{O}(\epsilon^2)$ and higher, we are left with an equation of state that is quadratic (but monotonic) in $T^{(0)}$ and linear in $T^{(1)}$. Thus, for $\Theta > 2$ cabbeling occurs until $\epsilon = \frac{1}{\Theta}$ becomes small, at which point, cabbeling becomes a secondary effect and the leading order effect is to evolve under a monotonic NLEOS, specifically one that is purely quadratic in temperature. This means that gravity currents with large values of Θ evolve similarly to the near-surface currents discussed in chapter 4 (called the T cases) to leading order. See (4.16) in the limit of large Θ_1 (recall Θ_1 is one of the two NLEOS parameters defined in (4.15)). Figure 5.3 and table 5.1 are provided as visual summaries of the above discussion. In figure 5.3, it is assumed that $\Delta\tilde{T}_1 > 0$ for brevity. For cases where $\Delta\tilde{T}_1 < 0$ the locations of each marker on the diagram would be reflected about $\tilde{T}_{md}$.

5.3.2 Experimental Configuration

To discuss the physics of the $\Theta > 2$ regime, we will present two experiments. We must have $\frac{1}{2}\left(\tilde{T}_i + \tilde{T}_a\right) > \tilde{T}_{md}$ to ensure that $\Theta > 2$. In this chapter $\tilde{T}_a$ is either 2.5 °C or 5.5 °C. However of $\Delta\tilde{T}_2^2$ does not change between cases (see table 5.3 for details). In the first experiment, Θ is manipulated by varying the magnitude of $\Delta\tilde{T}_1$. In the second experiment, the relative intrusion depth is manipulated by varying the total depth of the domain h. By modifying h, we are modifying the amount of intruding fluid relative to the domain depth, which leads to variations in the head height of the initial hypopycnal current. For gravity currents under linear equations of state, the head height of the current is about half the height of the initial intrusion (for large enough Grashof number; for smaller Grashof numbers, viscosity plays a more prominent role in determining the characteristics of the resulting current). Cases are presented in table 5.3 and are named based on their values for Θ and h. See the caption of 5.3 for details.

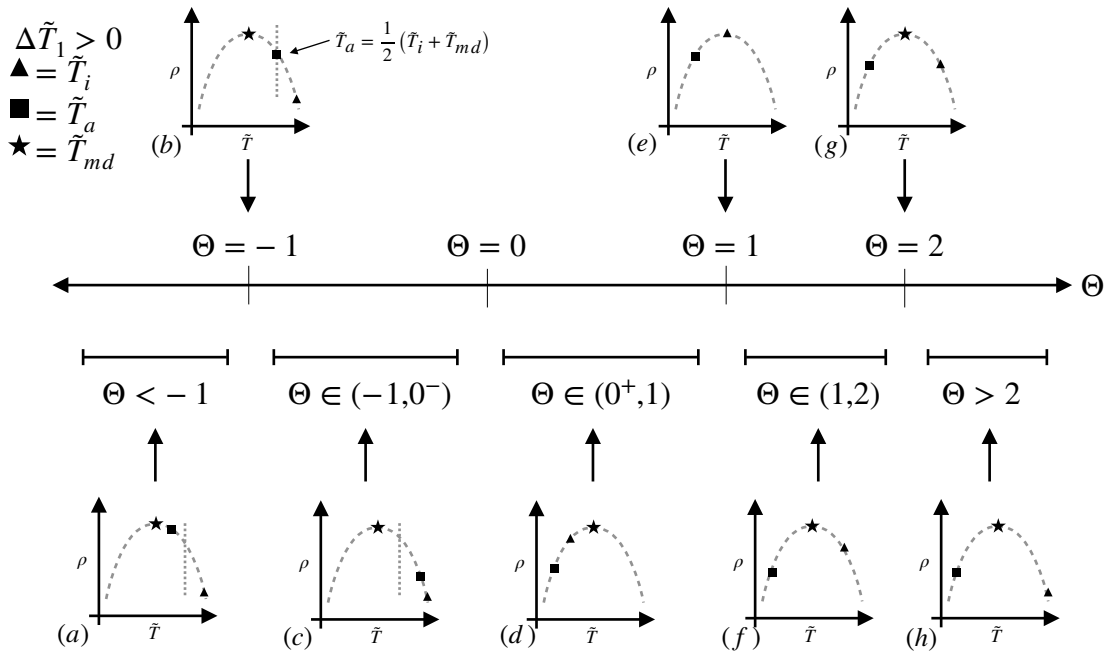

Figure 5.3: A schematic representation of different values and intervals of Θ and what they imply about the expected behaviour of the resulting gravity current. Each set of axes shows the quadratic equation of state and the markers represent the temperatures of the intruding fluid (triangles) and the ambient fluid (squares), as well as the temperature of maximum density (stars). In the above figure, it is assumed that $\Delta\tilde{T}_1 > 0$. For cases where $\Delta\tilde{T}_1 < 0$ is of equal magnitude and opposite sign, the location of the temperature markers are flipped across the line $\tilde{T} = \tilde{T}_{md}$. Dotted vertical lines represents the average of the intruding and ambient temperatures and are included only where necessary.

Case	Ordering of $\tilde{T}_i$, $\tilde{T}_a$, and $\tilde{T}_{md}$
$\Theta < -1$	$\tilde{T}_i > \tilde{T}_a > \tilde{T}_{md}$ and $\tilde{T}_a < \frac{1}{2}(\tilde{T}_i + \tilde{T}_{md})$
$\Theta = -1$	$\tilde{T}_i > \tilde{T}_a > \tilde{T}_{md}$ and $\tilde{T}_a = \frac{1}{2}(\tilde{T}_i + \tilde{T}_{md})$
$-1 < \Theta < 0$	$\tilde{T}_i > \tilde{T}_a > \tilde{T}_{md}$ and $\tilde{T}_a > \frac{1}{2}(\tilde{T}_i + \tilde{T}_{md})$
$1 > \Theta > 0$	$\tilde{T}_a < \tilde{T}_i < \tilde{T}_{md}$
$\Theta = 1$	$\tilde{T}_i = \tilde{T}_{md}$
$1 < \Theta < 2$	$\frac{1}{2}(\tilde{T}_i + \tilde{T}_a) < \tilde{T}_{md}$
$\Theta = 2$	$\frac{1}{2}(\tilde{T}_i + \tilde{T}_a) = \tilde{T}_{md}$
$\Theta > 2$	$\frac{1}{2}(\tilde{T}_i + \tilde{T}_a) > \tilde{T}_{md}$

Table 5.1: A representation of the ordering the intruding temperature, ambient temperature, and temperature of maximum density ($\tilde{T}_i$, $\tilde{T}_a$, and $\tilde{T}_{md}$ respectively) given different intervals of Θ for positive $\Delta\tilde{T}_1$. Θ is defined in (5.4) and $\Delta\tilde{T}_1 = \tilde{T}_i - \tilde{T}_a$.

Note that by changing Θ and h, we also change the Grashof number. This motivates the definition of another number called Gr_0. It is defined as

$$\mathrm{Gr}_0 = \frac{gC(\Delta\tilde{T}_2)^2 H^3}{\nu^2}. \tag{5.34}$$

Since the magnitude of $\Delta\tilde{T}_2$ is held constant in this chapter, Gr_0 invariant upon changing Θ or h. The Grashof number in table 5.3 is related to Gr_0 by

$$\mathrm{Gr} = \mathrm{Gr}_0 \frac{\Theta}{h^3}. \tag{5.35}$$

Gr_0 is held constant for all cases except VT5h4 and VT6h4 where is has been increased by a factor of four.

5.4 Results

5.4.1 Θ and h dependence of the development of the flow

In this subsection, the results of several numerical simulations in the $\Theta > 2$ regime will be shown. To discuss the basic dynamics, we can consider T3h2, which has $\Theta = 3$ and $h = 2$.

Parameter Symbol	Value	Dimensions	Description
g	9.81	m/s^2	Acceleration due to gravity
$\tilde{T}_{md}$	3.98	°C	Temperature of maximum density
ρ_0	999.974	kg/m^3	Constant reference density
C	7.6×10^{-6}	$°C^{-2}$	NLEOS constant (see (5.1))
H	2	m	Dimensional depth of domain
L	20	m	Dimensional length of domain
Pr	10	-	Prandtl Number (see (5.12))
x_ℓ	8	-	Dimensionless lock length

Table 5.2: The list of constant parameters used in this chapter, their values, dimensions, and a description.

Neither Θ nor h are extreme values considered in this chapter so cabbeling is still a leading order effect ($\epsilon = \frac{1}{\Theta}$ is not small compared to unity). Snapshots of the temperature and velocity fields at different times for T3h2 case are shown in figures 5.4 and 5.5 respectively. The dynamics of the other cases for each experiment are qualitatively similar, with only minor differences in the details.

Figure 5.4 shows that the initial hypopycnal current, which is lighter than the ambient (except for a thin band around the intrusion), flows from left to right along the top surface. Mixing in the body and tail of the current creates water of a higher density than both the intrusion and the surrounding ambient. The denser fluid sinks, as visible in panels (a)–(c). We can see that the initial intruding water mass quickly mixes due to this process. Once enough dense fluid gathers near the bottom surface, a new coherent hyperpycnal current is created. This current flows away from the left wall, visible in panels (d)–(f). Due to the propagation of the hyperpycnal current, a near surface reverse flow is induced which pushes the remains of the initial hypopycnal current back towards the left hand wall.

The hyperpycnal current has a new typical temperature, and is heavier than the ambient, thus allowing it to flow along the bottom. Qualitatively speaking, the volume of the hyperpycnal current is much larger than the initial hypopycnal current indicating that a significant volume of ambient water has been entrained over the course of the cabbeling process. Note the time jump between panels (c) and (d). Recall that the non-dimensional temperature of maximum density is given by $1/\Theta$ (approximately 1/3 in this case), and it is important to note that the temperature of the bottom current is lower than $1/\Theta$, indicating that the hyperpycnal current consists of fluid that is not simply the maximally dense fluid, but some other temperature whose value is an emergent quantity of the dynamical process. This is true for all cases discussed in this chapter, and a more detailed

Case –	Gr –	Θ –	$\tilde{T}_i$ (°C)	$\tilde{T}_a$ (°C)	$\nu \times 10^6$ (m^2/s)	
T2.2h4	1.43×10^5	2.2	2.156	5.5	1	$\delta_x = 0.8$, $\delta_z = 0.08$
T3h4	1.00×10^6	3.0	0.944	5.5	1	$h = 4$, $l = 160$
T4h4	2.68×10^6	4.0	8.5	2.5	1	
T5h4	4.82×10^6	5.0	9.9	2.5	1	
T6h4	7.71×10^6	6.0	11.38	2.5	1	
VT5h4	1.93×10^7	5.0	9.9	2.5	0.5	
VT6h4	3.08×10^7	6.0	11.38	2.5	0.5	
T7h4	1.12×10^7	7.0	12.86	2.5	1	
T8h4	1.59×10^7	8.0	14.5	2.5	1	
T2.2h2	1.14×10^6	2.2	2.156	5.5	1	$\delta_x = 0.4$, $\delta_z = 0.04$
T2.4h2	2.55×10^6	2.4	1.852	5.5	1	$h = 2$, $l = 80$
T2.63h2	4.44×10^6	2.63	1.500	5.5	1	
T2.8h2	6.00×10^6	2.8	1.244	5.5	1	
T3h2	8.03×10^6	3.0	0.944	5.5	1	
T3.5h2	1.56×10^7	3.5	0.018	5.5	1	
T4h2	2.14×10^7	4.0	8.5	2.5	1	
T5h2	3.86×10^7	5.0	9.9	2.5	1	
T6h2	6.17×10^7	6.0	11.38	2.5	1	
T7h2	9.00×10^7	7.0	12.86	2.5	1	
T8h2	1.27×10^8	8.0	14.5	2.5	1	
T3h1.82	1.07×10^7	3.0	0.944	5.5	1	$\delta_x = 0.365$, $\delta_z = 0.0364$
T4h1.82	2.86×10^7	4.0	8.5	2.5	1	$h = 1.82$, $l = 72.7$
T5h1.82	5.14×10^7	5.0	9.9	2.5	1	
T6h1.82	8.21×10^7	6.0	11.38	2.5	1	
T7h1.82	1.20×10^8	7.0	12.86	2.5	1	
T8h1.82	1.69×10^8	8.0	14.5	2.5	1	

Table 5.3: The cases presented in this chapter. Case names are denoted by the "Txxhyy", where xx and yy represent the value of Θ (the NLEOS parameter (5.4)) and h (the depth of the domain, found in the rightmost column) for the case. The exception to this are cases preceded by a "V". In those instances, the viscosity and thermal diffusivity have been reduced by 50%. Gr represents the Grashof number, (5.12), $\tilde{T}_i$ is the dimensional intruding temperature, and $\tilde{T}_a$ is the dimensional ambient temperature, ν is the kinematic viscosity. Parameters that remain unchanged in groups of cases are shown in the rightmost column. δ_x and δ_z are the transition thicknesses in the x and z directions respectively, and l is the tank length.

discussion on the temperatures of the bottom currents is presented below.

Figure 5.5 shows the dimensionless horizontal component of the velocity field. The initial hypopycnal current develops and flows along the top surface (panel (a)–(c)). The currents shown in panel (d) are very irregular, but this state is ultimately a transition between the hypopycnal and hyperpycnal currents. In panels (e) and (f), we can see the signature of the hyperpycnal as it propagates to the right, and the return flow moving to the left near the top surface. It is interesting to note that the head height of the bottom current is approximately half the depth of the domain, which is in qualitative agreement to that seen in the full-depth lock release simulations from both Härtel et al. (2000b) and Cantero et al. (2008) in the slumping regime. Furthermore, we can see that the velocities in the hyperpycnal current are weaker than those in the hypopycnal current. The transition from a characteristic dimensional length scale of z_0 to $H/2$, and the subsequent reduction in velocity is a consistent feature across all cases studied in this chapter. This indicates that the emergent current has no memory of the initial height of the intrusion.

It is interesting to note that the reduction in the velocities of the hyperpycnal current does not lead to a relative decrease in the kinetic energy of the system. To see this, we can can analyze the domain average kinetic energy ke of the system, defined as

$$ke = \frac{1}{2lh} \int_0^l \int_0^h u^2 + w^2 \, dxdz. \tag{5.36}$$

Figure 5.6 shows the ke for each case with $h = 2$ and different values of Θ. This figure is broken up into two categories for clarity; low Θ in panels (a) and (b), and high Θ in panels (c) and (d). The left column is the entire time history of the ke prior to the current colliding with the end-wall, whereas the right column is the same data with the axis values adjusted to highlight the early development. Also note the difference in vertical and horizontal scales in each panel. Broadly speaking the evolution of the ke takes place over several stages; an increase by the propagation of the initial hypopycnal current, and an increase in ke by the hyperpycnal current. It should be noted that cabbeling itself is not a source of kinetic energy, but instead increases the potential energy, which is then transformed into kinetic energy by a buoyancy flux. The low Θ cases (T2.2h2, T2.4h2,T2.63h2, T2.8h2, and T3h2) are shown in panels (a) and (b), and these cases are characterized by a short time increase of ke as the initial hypopycnal current propagates, but this is quickly swamped by a much larger increase from the hyperpycnal current. There is a transient period between these stages where the ke oscillates but does not significantly increase. As Θ becomes larger, the initial rate of growth of the ke slows, and the second stage occurs at a later time. Eventually, the total ke reaches a peak and then decreases before the gravity currents ultimately collide with the right hand wall (the time at which the curves terminate).

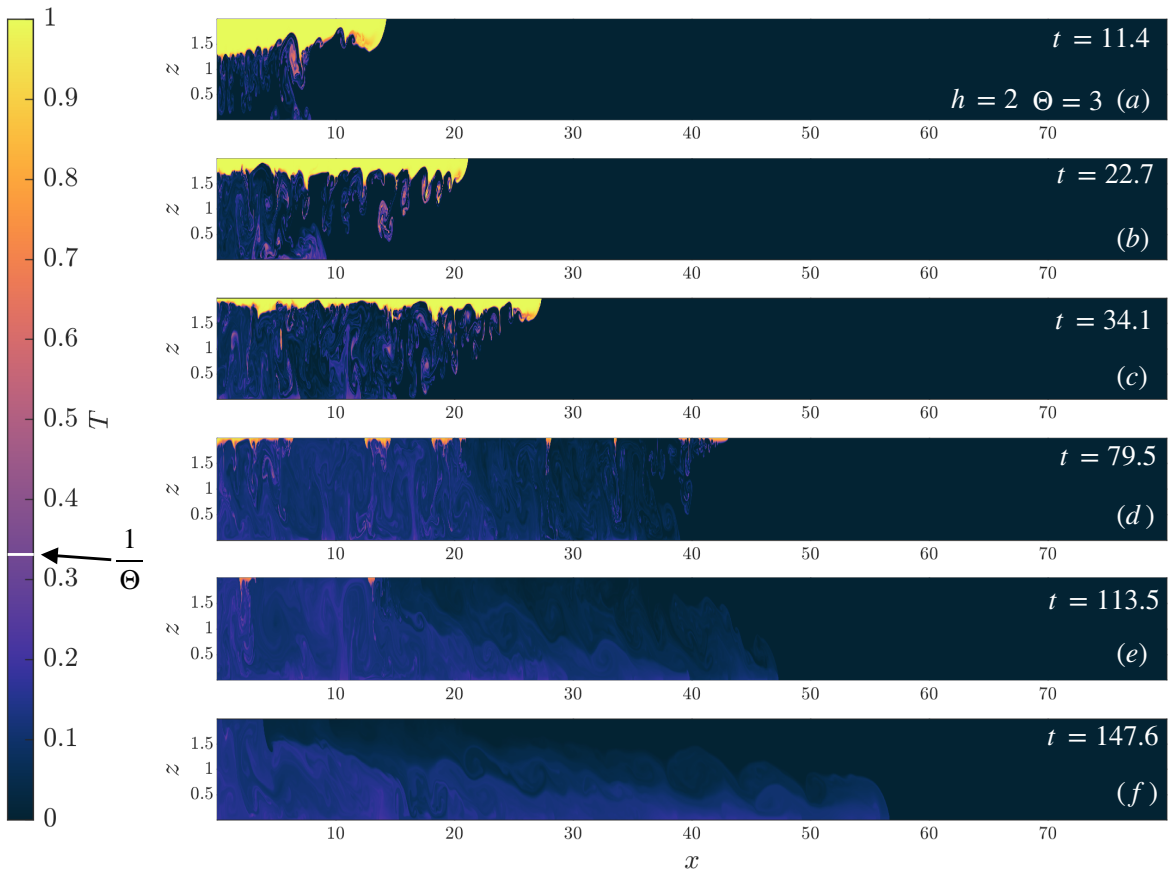

Figure 5.4: Temperature fields for T3h2, given by (5.2). The non-dimensional temperature of maximum density for T3h2 ($\frac{1}{\Theta}$) is marked on the colourbar. Times are located on each panel. Panels (a)–(c) show the general evolution of the hypopycnal (near-surface) current, panel (d) shows a transition time, and panels (e) and (f) show the hyperpycnal (near-bottom) current. Notice the increase in head height in panel (f) relative to panel (a). Notice also that the hyperpycnal current quickly outruns the hypopycnal current.

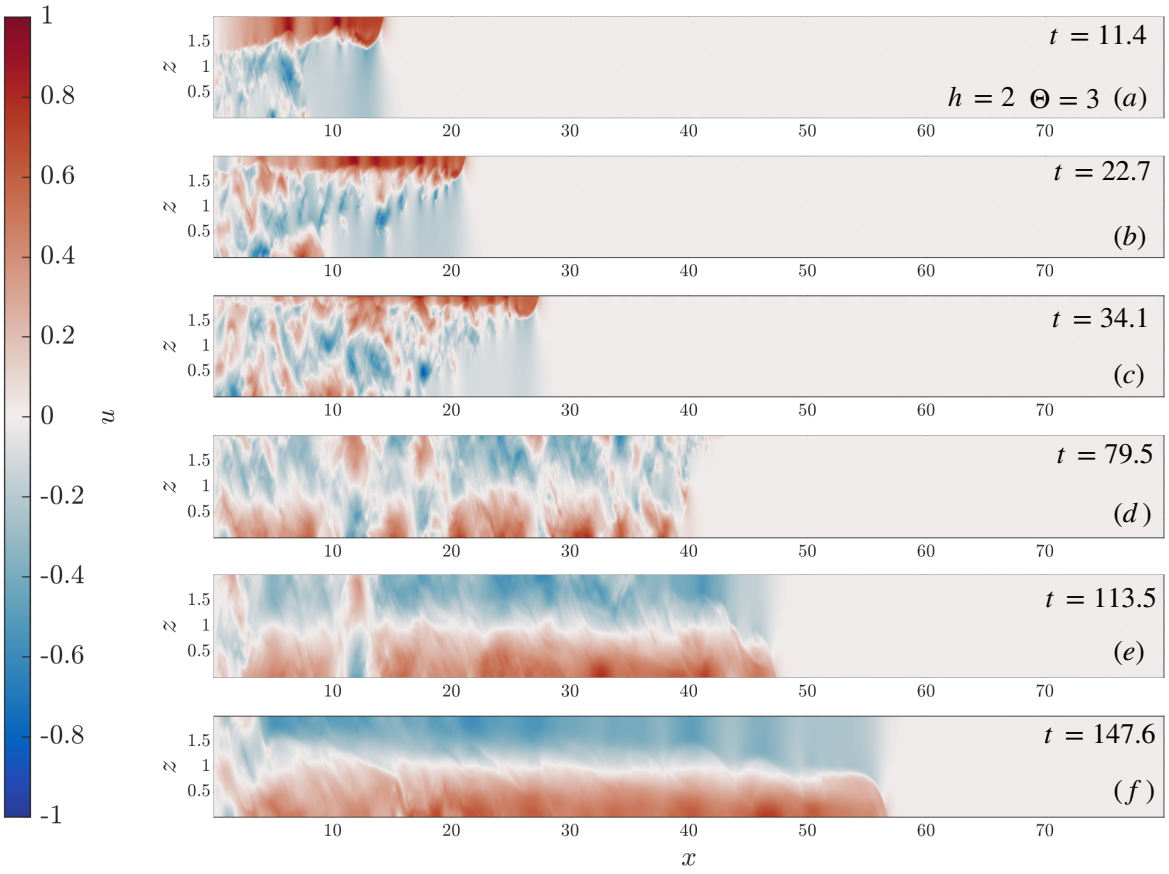

Figure 5.5: Horizontal component of non-dimensional flow velocity for T3h2. The times of each plot are the same as in figure 5.4. Notice the decrease in the velocity of the current in panel (f) relative to panel (a).

We can see in 5.6(c) and (d) that by further increasing Θ in the 3.5-8 range (T3.5h2,T4h2, T5h2, T6h2, T7h2, and T8h2), the first stage of growth by the propagation of the initial hypopycnal current is elongated resulting in a clear localized peak in the ke, before slowly decreasing as the hypopycnal current spreads. Following this, there is a more gradual increase due to the slumping of the hyperpycnal current. The general behaviour that can be gleaned from figure 5.6 is that for Θ near 2, the hypopycnal current does not complete its initial acceleration before cabbeling and the subsequent formation of the hyperpycnal current starts to dominate the kinetic energy history. Conversely, for larger values of Θ, the initial hypopycnal current is allowed to develop into a more mature current before cabbeling ultimately generates the hyperpycnal current.

In figure 5.7, we compare the total kinetic energy of two values of Θ (3 and 6) for three values of h. These Θ values were chosen chosen to best illustrate the sensitivity of the total kinetic energy based on the variation of Θ and h. Figures 5.7(a) and (b) show the total kinetic energy for the T3h4, T3h2, and T3h1.82 cases. It is clear that by making the domain shallower (or alternatively increasing the initial intrusion height), we get a more well-defined early evolution of the flow, indicated by the rapid rise and peak in kinetic energy. T3h4 shows a severe early and late reduction in total kinetic energy relative to the T3h2 and T3h1.83 cases, potentially indicating the impact of viscosity due to the relatively low value of Gr. It is interesting that in the interval $100 < t < 200$, the relative increase in the total kinetic energy is similar between T3h4, T3h2, and T3h1.82. This indicates that the development of the hyperpycnal current may be unaffected by the magnitude of Gr over this time interval. Figure 5.7(c) and (d) show the same quantity for cases T6h4, T6h2, and T6h1.82. We can see a more well defined initial acceleration of the current, and peak in the kinetic energy. Note that the hyperpycnal currents for T6h2 and T6h1.82 become large enough that they run into the wall at $x = l$ before they can fully develop, but T6h4 does not. This is interesting as the ke increase due to the hyperpycnal current results in a larger total ke than that of the initial peak.

Figures 5.8(a,b,c) show Hovmoeller plots of the temperature field at $0.95h$ for T3h4, T3h2, and T3h1.82 between $0 < x < 50$ and $0 < t < 100$. Figure 5.8(d,e,f) shows the same for T6h4, T6h2, and T6h1.82 between $0 < x < 70$ and $0 < t < 200$. These figures highlight the overall similarity in the time history of the near-surface temperature for each of the cases compared. For example, first consider panels (a,b,c) (the same discussion below can be applied to panels (d,e,f)). Note that while the broad features such as the propagation speed of the current (inferred by the slope in $x-t$ space of the front) and halting behaviour are similar between all three of these cases, T3h4 (shown in panel (a)) travels the shortest non-dimensional distance relative to T3h2 (panel (b)) and T3h1.82 (panel (c)), indicating the impact of the low value of Gr. Directly comparing panels (b) and (c) (where Gr has

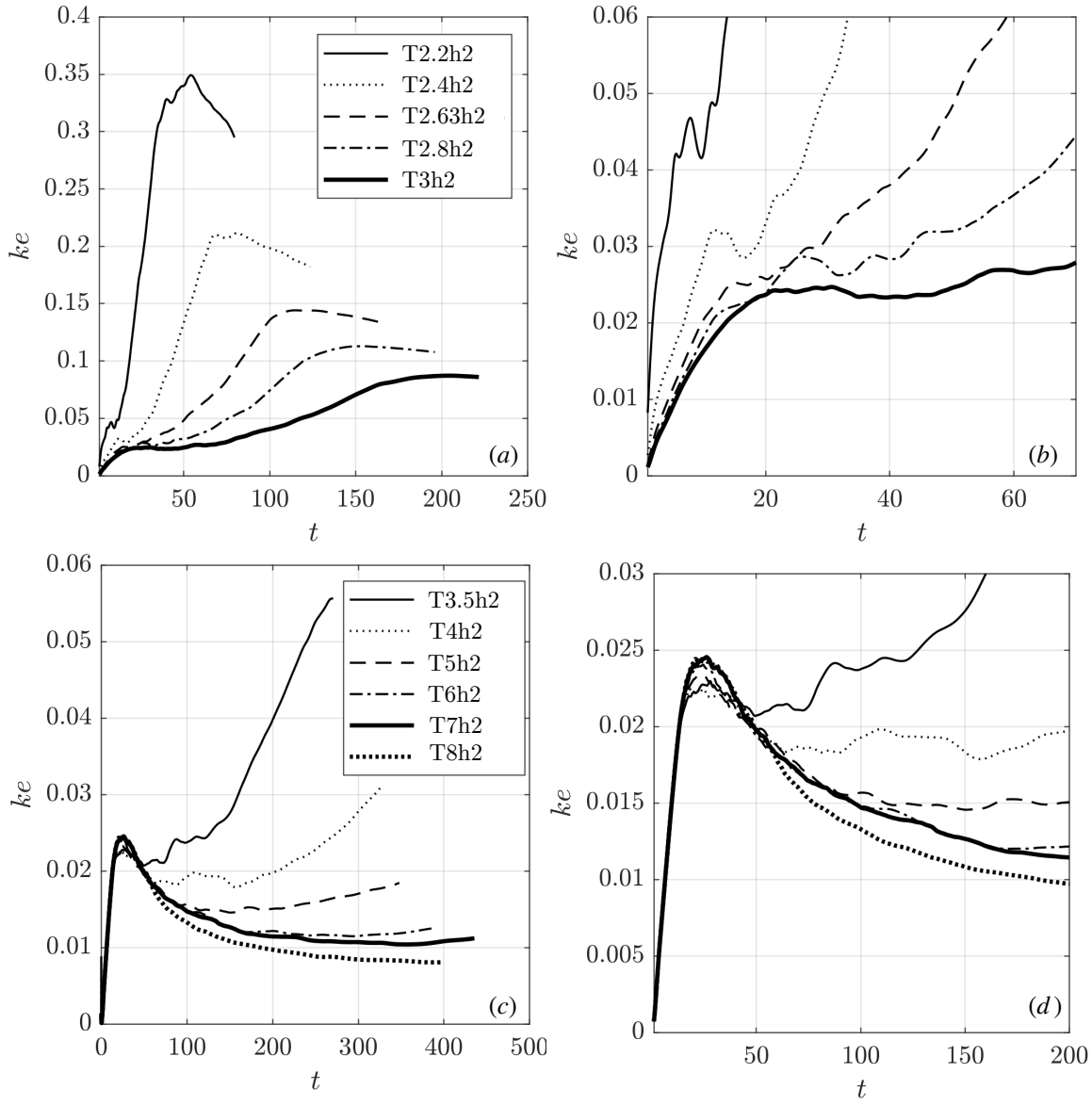

Figure 5.6: Time series of the total kinetic energy for all cases with $h = 2$. Panel (a) shows the total kinetic energy for cases with $2.2 \leq \Theta \leq 3$. Panel (c) shows the same quantity for cases with $3.5 \leq \Theta \leq 8$. Panels (b) and (d) are detailed views of the early evolution.

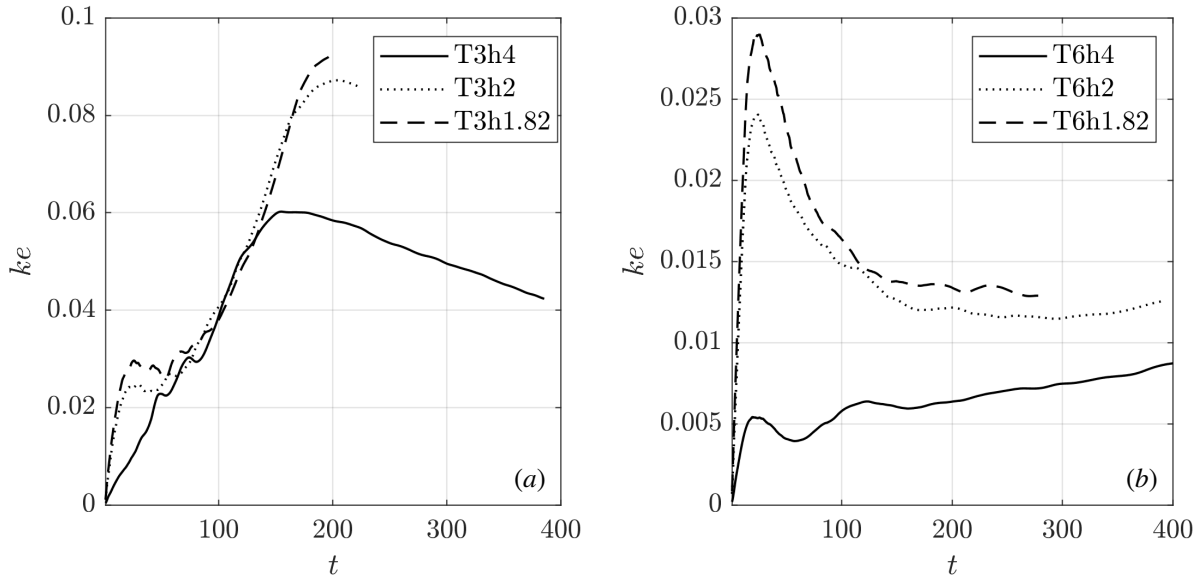

Figure 5.7: Time series of the total kinetic energy comparing between cases with varying h (Θ held constant in each panel). Panel (a) shows the cases with $\Theta = 3$, while panel (b) shows the cases with $\Theta = 6$.

been increased by decreasing h) reveals negligible differences between the distance travelled between these two cases. In other words, there are noticeable differences in the travelled distance between T3h4 and T3h1.82, but comparatively small differences in the travelled distances between T3h2 and T3h1.82. These results indicate that for low enough Grashof number, the quantitative current characteristics are modified relative to cases with higher values Gr. The implication then becomes that the large scale behaviour of the current may be relatively independent of Gr for large enough values. The exact regime where the gravity current evolution achieves Gr independence is beyond the scope of this thesis. Some discussion on this is provided in Härtel et al. (2000a) and Cantero et al. (2008). Recall that Gr independence in head location was noted in the results of figure 4.5(c) in chapter 4, where a larger value of Gr led to an increased discrepancy between the head locations of near-surface propagating currents versus near-bottom propagating currents, and by reducing Gr, these differences became smaller.

Additionally, late in the time history, we can see a near-surface reversal of the propagation direction. The prominence of this feature increases as $\Theta \to 2$ and was clearly visible in cases where $2 < \Theta < 3$. However, a key feature that these figures highlight is the variation in the maximum extent that the current achieves as Θ is increased for constant h. At low Θ, the current's near-surface forward motion ceases much earlier in the tank relative to a case with larger Θ, made apparent by comparing the horizontal axis across panels in the same column of figure 5.8. This is discussed in the next section.

5.4.2 The maximum extent of the current

Figure 5.8 highlights the propensity of the hypopycnal currents to progress down the length of the domain, and then halt. The maximum distance over which this occurs, denoted by $\mathcal{L}$, is an important parameter because it represents the length (in the x direction) of the rectangular region that characterizes the volume of fluid that makes up the emergent hyperpycnal current. For context, the maximum extent of gravity currents has been studied before, but in the context of sediment-laden gravity currents. Maxworthy (1999) used laboratory experiments to first identify the formation of a secondary current that flows along the bottom of the domain. He tracked the maximum extent as a function of the excess density ratio (the ratio of density differences due to salt versus that of sediment). Sutherland et al. (2018) went a step further and performed laboratory experiments of hypopycnal flows that underwent convective sedimentation with varying particle sizes. They measured the maximum distance of the hypopycnal current and found a semi-empirical relationship to the particle diameter. They found that as particles became larger, the maximum extent of the hypopycnal current increased. Davarpanah Jazi and Wells (2020) performed

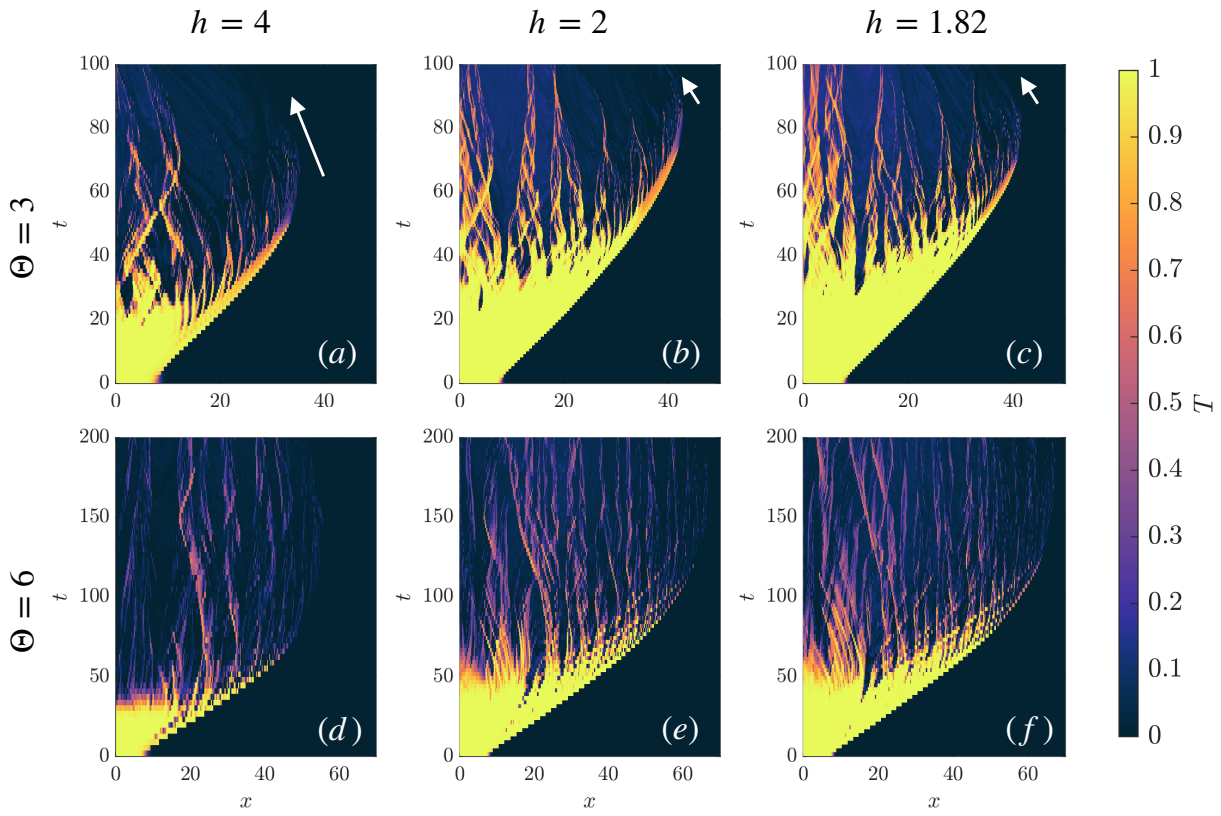

Figure 5.8: Hovmoller plots of the temperature at a height of $0.95h$ for the cases with varying Θ and h. Θ is constant along each row of panels, and h is constant along each column. Arrows are included in panels (a,b,c) to highlight the flow reversal.

experiments along a flat bottom tank and highlighted the expected maximum extent for different intervals of the density ratio. The point is that in these studies, the maximum extent of the current driven by convective sedimentation is important because it predicts the length scale of the deposition of sediment on the bottom of the tank. More on the significance of the maximum extent in this context can be found in the discussion section. In the simulations presented within this chapter, it is not necessarily sediment deposition that is of interest, but more the transport of heat (and perhaps dissolved gases in a field setting, for example).

For the following section, we will define

$$\mathcal{L} = f\left(\Theta, h, \mathrm{Gr}_0\right), \tag{5.37}$$

We calculate $\mathcal{L}$ (dimensionless and defined in (5.37)) by simply recording the location of the front of the gravity current at a height $0.95h$. In (5.37), f is some unknown function of Θ, h, and Gr_0. The location of the front of the gravity current at a given time is defined as the furthest distance from the left hand wall where $T = T_c$, where $T_c = 0.01$. The computed values for $\mathcal{L}$ are not strongly dependent on the choice of T_c until it is greater than about 0.5 (the estimate of the front location of the current is incorrect) or until it is less than about 0.0001 (small numerical variations in the flow start to give incorrect results). Note that T_c corresponds to a different dimensional temperature for each case.

$\mathcal{L}$ is plotted as a function of Θ in figure 5.9(a). Cases with $h = 4$ are represented by blue squares, cases with $h = 2$ are represented by red triangles, and cases with $h = 1.82$ are represented by black diamonds. VT5h4 and VT6h4 are represented by green circles. We can see that $\mathcal{L}$ generally increases with Θ, however, past $\Theta = 3$ the slope of increase is shallower. Furthermore, for large h (a relatively deep domain), we can see that the maximum extent is severely affected for Θ between 3 and 7, relative to the cases with smaller h. This was also apparent in the temperature Hovmoeller plot in figure 5.8(a). It is not until Θ is increased past about 6 where the maximum extent is more comparable to the cases with $h = 2$ and $h = 1.82$. The reason for this discrepancy is that the Grashof number is small enough that the hypopycnal current enters the viscous regime early in its development, leading to a decreased maximum horizontal extent. This is confirmed by re-running cases T5h4 and T6h4 but reducing the viscosity by a factor of two (recall that these cases are VT5h4 and VT6h4). Note that by increasing Gr_0 by a factor of four (reducing viscosity by a factor of two), we increase the maximum extent of those two cases. This led to $\mathcal{L}$ values more comparable to the cases with larger h (and equal Θ).

We can see that continuing to increase Θ increases the distance in which the hypopycnal current travels before it halts. As discussed previously, continually increasing Θ implies

that the leading order functional form of the buoyancy forcing is purely quadratic, which precludes cabbeling (and similar to the "T cases" presented in chapter 4). For this reason, we should expect $\mathcal{L}$ to continue increasing with Θ but at a slower rate at larger Θ.

The maximum horizontal extent $\mathcal{L}$ is an important parameter because it helps characterize the approximate area of the hyperpycnal current, which consists of mixed ambient and intruding fluid. For each hyperpycnal current, we estimate the area by assuming that the mixing of the hypopycnal current and ambient occurs over a rectangular region of length $\mathcal{L} + x_\ell$, and the depth h. This can be thought of as the "initial area" for the hyperpycnal flow, and for brevity, this region will be called the "entrainment zone". The full depth is chosen as the vertical length scale since the mixing takes place over the entire depth of the domain. Mathematically, area of the entrainment zone is given by

$$\mathcal{A} = (\mathcal{L} + x_\ell)h. \tag{5.38}$$

The area of the current calculated from the simulation data at a given time is

$$A = \int_0^l \int_0^h \chi dx dz, \tag{5.39}$$

where the indicator function χ is

$$\chi = \begin{cases} 1 & T > T_c \\ 0 & T \leq T_c \end{cases}. \tag{5.40}$$

Recall $T_c = 0.01$ is the critical temperature, which was found to adequately represent the area of the current. The computed area of the current is sensitive to the choice of T_c, and values of T_c greater than about 0.05 tend to underestimate the area of the current. Figure 5.9(b) shows the area of the hyperpycnal current A normalized by $\mathcal{A}$. The times were chosen so that the initial hypopycnal current has ceased flowing and significant mixing between the hyperpycnal current and remaining ambient had not occurred. We can see that for larger Θ, $A/\mathcal{A}$ approaches unity, meaning that $\mathcal{L} + x_\ell$ is a good representation of the lock length of the hyperpycnal current. Conversely, it is apparent that for low Θ, $\mathcal{A}$ underestimates the initial fluid area of the hyperpycnal current. The reason for this lies in the near surface reverse flow mechanism discussed earlier. For low Θ, cabbeling occurs very quickly relative to the propagation of the gravity current, so the bottom current forms and quickly outruns the initial hypopycnal current. The near surface reverse flow of equal magnitude (but opposite direction) to the bottom current pushes the initial hypopycnal current back towards the left hand wall. Thus, cabbeling and subsequent mixing takes place in a very narrow region near the left hand wall, resulting in a relatively small estimate of $\mathcal{L}$, and therefore $\mathcal{A}$.

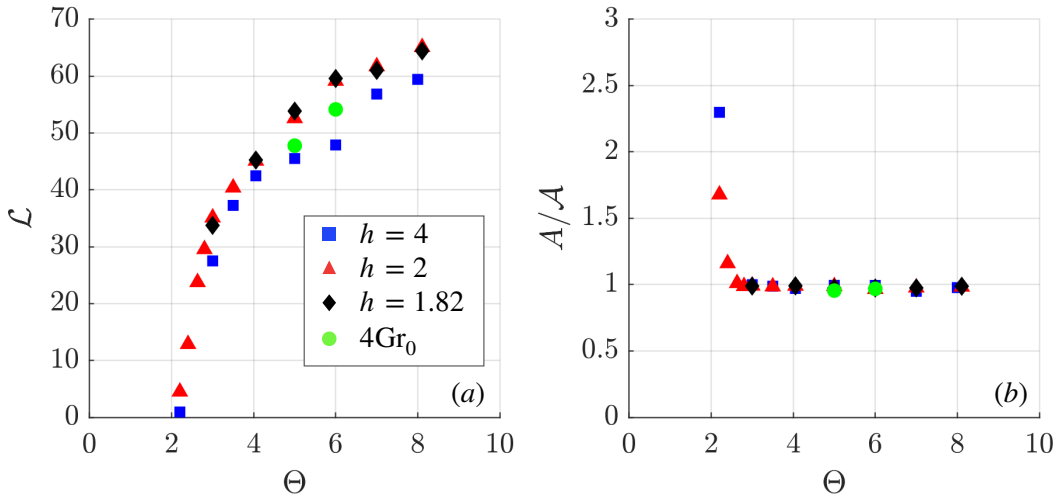

Figure 5.9: Panel (a) shows the variation of $\mathcal{L}$ for the large intrusion cases (⧫), the medium intrusion cases (▲), and the small intrusion cases (■). Panel (b) shows the area of the hyperpycnal current normalized by the area of the entrainment zone $\mathcal{A}$ after the cabbeling is quenched. VT5h4 and VT6h4 are also included and denoted by a green •.

5.4.3 Early hyperpycnal current characteristics

The size of the entrainment zone also affects the temperature distribution of the bottom current. Larger entrainment zones lead to mixing with more ambient fluid, so temperatures will be closer to $T = 0$. We can assess the qualitative properties of the gravity current as Θ varies by comparing the current's spatial structure at a late time when the hypopycnal current has been mixed out. A comparison is presented in figure 5.10 (a)–(d). In this figure the density field is multiplied by 2Θ. This re-scaling puts the maximum density at 1 and the density of the ambient at 0. This facilitates an easy comparison between cases. The times were chosen such that the dimensional temperature in every location of the domain falls between the ambient temperature and $\tilde{T}_{md}$. By increasing Θ, we can see that the volume of the current is larger, in qualitative agreement with the difference in entrainment zone size, and we can also see that the density distribution within each current is qualitatively different. This is especially noticeable in the body and tail of the current for the T2.2h2 (figure 5.10(a)) case when compared to T3.5h2 (figure 5.10(d)).

Furthermore, the density distribution in the head is clearly different. For lower Θ, the density in the head is much closer to the maximum density (indicated by brighter colours), and increasing Θ tends to decrease the head's density. Along the bottom of the T2.2h2

case, we can see a layer of fluid that is very close to the maximum density, whereas in the T3h2 case, the densities are all less than the maximum density. Since the T3h2 case actually starts with a wider range of temperatures (the largest $\Delta\tilde{T}_1$), it is interesting to note that the temperatures are relatively closer to the ambient. The density fields for the cases with $\Theta > 3.5$ are not shown simply because the tank is not long enough for the hyperpycnal current to develop. In these cases, maximum extent of the hypopycnal current is nearly the entire length of the tank, so the hyperpycnal current simply has no room to develop and propagate.

Figures 5.10(e)–(g) provide a measure of the distribution of temperatures within the current for T2.2h2, T2.63h2, T3h2, and T3.5h2. These plots highlight the form of the distribution of temperatures within the current. The fluid within the current is defined by any parcel that has $T > T_c$. The upper and lower bounds of the blue box indicate the spread between the 25th percentile and 75th percentile of the data, while the upper and lower whiskers show the spread between the lower (upper) extreme and lower (upper) quartile. The horizontal red line represents the median and the filled diamond represents the mean. Figure 5.10(e) shows the data, as well as the non-dimensional temperature of maximum density $\frac{1}{\Theta}$, for the four cases, figure 5.10(f) shows the data on an axis normalized by the temperature of maximum density, and figure 5.10(g) shows the non-dimensional density normalized by the maximum density. These plots highlight the fact that by increasing Θ, the distribution of temperatures within the hyperpycnal current become systematically narrower, with the distribution of temperatures grouped around the median. Furthermore, the temperatures become closer to the ambient ($T = 0$). This is further evidence of the general hypothesis that currents with larger Θ mix with a larger volume of ambient fluid, leading to a narrower temperature distribution.

On the other hand, the wider distribution in T2.2h2 is a result of the early evolution of the current. Recall that the formation of the hyperpycnal current occurs relatively early, and this induces the near surface reverse flow. Thus, the hypopycnal current, which is the source of the cabbling, reverses direction and is trapped near the left hand wall, forcing cabbeling only to act in this region. Since the hyperpycnal current continues propagating, dense fluid is fed only to its tail, leading to a wider range of temperature.

An interesting point that is made clear by figure 5.10 concerns the variation of the head location of the currents. We can see that the head location for T3.5h2 is actually the furthest down the length of the tank. The explanation is that the times shown were chosen to best highlight the state of the current after it has begun to flow, and not necessarily to facilitate a comparison in head location. However, this brings up an interesting question about long term evolution of the hyperpycnal currents. As Θ is increased, the head speed of the initial hypopycnal current increases, meaning more distance is covered in the first

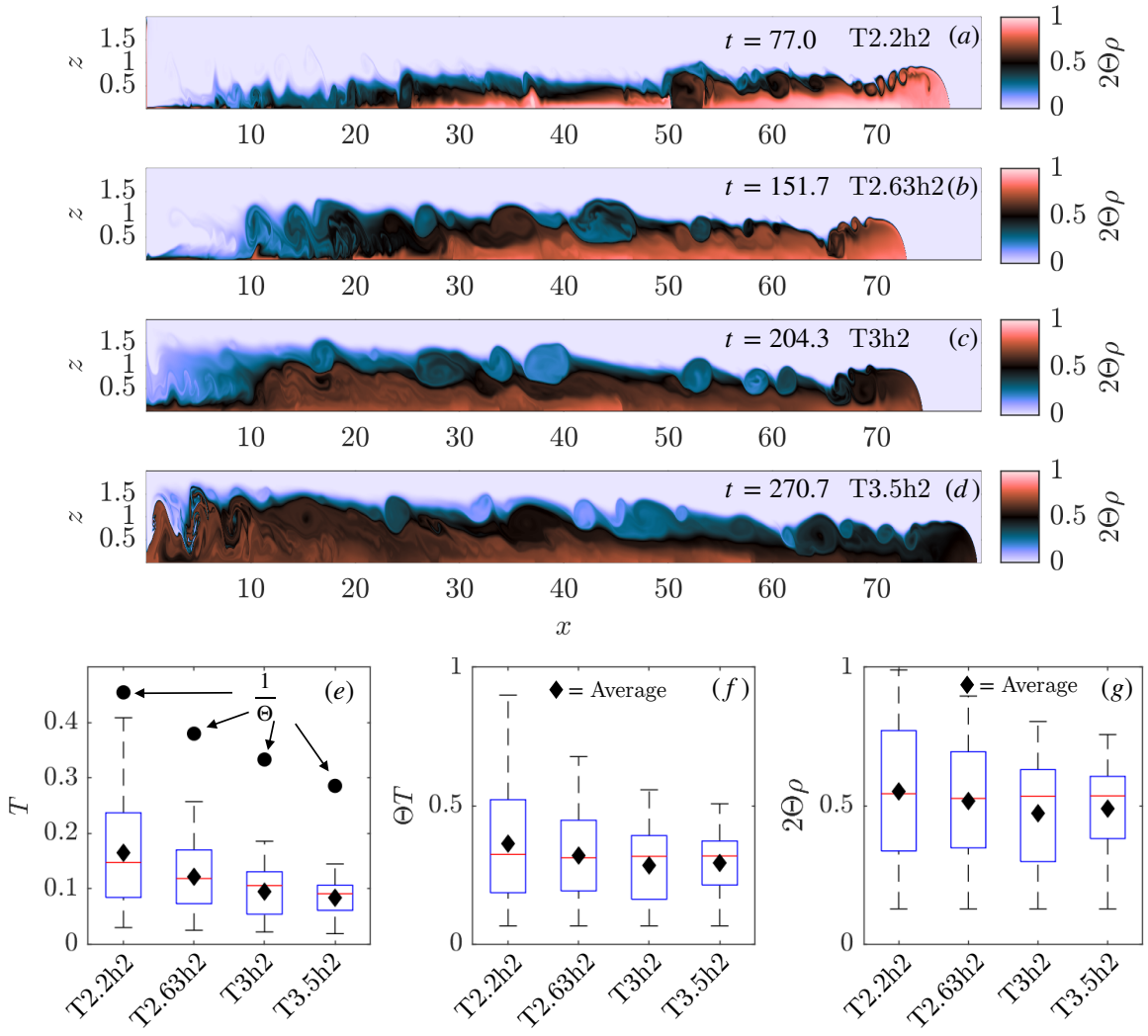

Figure 5.10: Panels (a)–(d) show the re-scaled density field for several cases. Case names and times are located on the plots. A density of 0 corresponds to the ambient density while a density of 1 corresponds to the maximum density. Panel (e) shows box and whisker plots of the temperature distribution within the current. Panel (f) and (g) show the same data on re-scaled axes where 1 corresponds to a temperature $T = \frac{1}{\Theta}$ (the non-dimensional temperature of maximum density) and 0 is the ambient temperature. The interquartile range is denoted by the blue boxes and the median temperature is denoted by the red line. The mean temperature of the current is indicated by ♦ and $\frac{1}{\Theta}$ is indicated by •.

phase of its evolution over a given time interval. However, for large enough Θ, the area of ambient fluid that is entrained is larger leading to a much smaller density difference between the head of the hyperpycncal current and the remaining ambient, evidenced by figures 5.10(e)–(g). Thus, while these currents may initially attain larger distances, it is reasonable to think that the hyperpycnal currents from lower Θ cases may eventually catch up due to their larger driving density difference.

5.5 Summary and Discussion

In this chapter, we performed numerical simulations of gravity currents in the cabbeling regime. We highlighted the general evolution of a specific class of gravity currents where ambient and intruding temperatures were on different sides of the temperature of maximum density and $\Theta > 2$, indicating that the density of the ambient is initially closer to the maximum density relative to the intrusion thus allowing the intrusion to initially rise. Cabbeling is an important driver of the dynamics in this chapter. Cabbeling occurs when two masses of water with different temperatures and equal density mix and a denser mass of water is generated.

In the present chapter, both Θ and h (the non-dimensional depth) were varied to build an understanding of the general behaviour of these currents in (Θ, h) space. In general, we found that currents initially slumped to the top surface and propagated while mixing along the body and tail of the current generated dense water due to cabbeling. Sinking of the dense water continually occurs as the initial hypopycnal current flows and eventually a hyperpycnal current forms along the bottom surface of the domain that quickly outruns the initial hypopycnal current. A consistent feature across all cases was that the head height of the hyperpycnal current was about half the depth of the domain, regardless of the initial height of the intrusion.

To further categorize the behaviour of these currents, we considered the *ke* and found that as Θ was increased, the timescale of the development of the gravity current increased before the onset of cabbeling. This agrees with the perturbation analysis that cabbeling is a higher order mechanism in the limit of large Θ. The total kinetic energy also showed that decreasing the height of the initial water mass led to a relatively small increase in kinetic energy due to cabbeling at constant Θ.

By using the near surface temperature in the along-tank direction, the maximum horizontal extent of each current was also tracked and compared. We showed that as Θ increases, the maximum extent of the hypopycnal current increased as well, but the slope

decreased as Θ became larger. Increasing h led to a reduction in horizontal extent at constant Θ. The Grashof number for the high h cases was small enough that viscous effects played a significant role early on. This was evident for T3h4, T4h4 and T5h4, as $\mathcal{L}$ clearly scales differently than the cases with $h = 2$ and $h = 1.82$. Two simulations were performed where the Grashof number was modified by changing viscosity (VT5h4 and VT6h4). By changing the value of viscosity, we can change the value of the Grashof number but keep Θ and h unchanged. In these cases the viscosity was reduced by 50% leading to an increase in the Grashof number by a factor of four. This led to larger maximum extents relative to the comparable cases T5h4 and T6h4. Similar behaviour was seen in experiments by Gladstone et al. (2004), as well chapter 4 of this thesis.

We used the maximum extent of the current as well as the total depth to define a rectangular region called the entrainment zone. This region acts as the reservoir of fluid that makes up the hyperpycnal current. It was shown that the entrainment zone is a good indicator of the area of fluid that makes up the hyperpycnal current except for Θ near two. In this regime, the calculated entrainment zone under-estimated the volume of the hyperpycnal current. For Θ close to two, the timescale for cabbeling was found to be shorter than the timescale of initial propagation of the current, so cabbeling occurred quickly and the hyperpycnal current formed before the initial hypopycnal current propagated a significant distance.

The distribution of density and temperature of the hyperpycnal current was also shown. The key observation is that increasing Θ makes the distribution of temperatures narrower about the median temperature. As Θ was increased, the hypopycnal current mixed with a larger region of ambient fluid, leading to an average temperature of the mixture closer to the temperature of the ambient. Alternatively, by reducing Θ to be close to two, the distribution was found to be wider, with more locations within the flow being close to $\frac{1}{\Theta}$ (the non-dimensional temperature of maximum density). Thus, hyperpycnal currents with Θ close to two generally exhibited more regions of dense fluid than currents with larger Θ.

The results of this chapter highlight an important characteristic about gravity currents. For a sufficiently large Reynolds number, gravity currents go through several self-similar phases of evolution as they progress, each corresponding to a different dominant momentum balance within the current. These phases are called the acceleration phase, the slumping phase, the inertial phase, and the viscous phase. In the acceleration, slumping and inertial phases, the dominant balance is between the driving pressure gradient generated by density differences, and the inertial term in the momentum equations. In the viscous phase, the dominant balance is instead between the inertial term and the viscous term. Each of these four phases manifest themselves as (among other things) a different scaling law for the head speed of the current. Cantero et al. (2008) discusses each of the four phases and provides

evidence for the dominant balance within each phase. They also provide quantitative relationships between the head speed, time, and the normalized lock-release volume V_0. For example, in the slumping phase, the gravity current head speed is approximately independent of time, and the time the current spends in this regime is simply proportional to V_0. In this regime, density changes within the head, as well as head height changes are negligible. It is not until the inertial regime, where the head speed scales as $V_0^{1/3}$ that gravity currents experience more significant head height and density changes.

How might we apply these regimes to the hypo- and hyperpycnal currents presented in this chapter? We expect that the only circumstance in which the currents may progress through these phases is at the high Θ limit. A primary assumption of the theory of each phase is that the volume of the current does not deviate strongly from its initial value (Huppert and Simpson, 1980), and since the initial hypopycnal currents with low Θ are immediately disrupted by cabbeling, this assumption is not satisfied. However, in the high Θ limit, we saw that the leading order behaviour was that of a non-cabbeling gravity current, so there is potential that currents in this limit may progress through each phase before cabbeling can completely extract the intruding fluid. More work is necessary to fully characterize these currents. Furthermore, as we saw in chapter 4 in figure 4.5(a), the head speed does not necessarily scale with time in the same way under a non-linear equation of state.

The more pertinent question is regarding the hyperpycnal current. As we saw, varying Θ increased the size of the entrainment zone, and the resulting hyperpycnal current. In principle, one can expect that increasing Θ indirectly increases the time interval of each of these regimes for the hyperpycnal current by increasing the nominal lock length, and therefore the V_0. What complicates this is the fact that by increasing Θ, we increase the initial volume of entrained ambient fluid, which reduces the characteristic density difference between hyperpycnal current and the remaining ambient. This is evident by the smaller mean and median temperatures and densities shown in figure 5.10(b). This density difference affects the buoyancy velocity and therefore the non-dimensional timescales on which the gravity current flows. A point of future work could be to make a more comprehensive characterization of the hyperpycnal current characteristics, such as a quantifying whether the phenomenological lock length can compensate for the reduced timescales created by the mixing, resulting in a net increase in the horizontal transport of heat and material with increasing Θ.

There are several additional future directions to take this research. The first is to identify if the relationship between $\mathcal{L}$, Θ, and h is substantially different if the boundary conditions are changed to no-slip. In the high Gr limit, we should expect that the boundary layers are significantly thinner relative to the length scales of the interior flow, so the

interior should evolve similar to the results presented here. However, it is unclear on if no-slip boundary conditions are even the "correct" boundary conditions. One could think that a density driven flow might be flowing beneath ice, so the boundary conditions have a certain variable roughness associated with them, as well as thermal boundary layers, melting (especially for high Θ), and entrainment of melt water. Another potential avenue is to discuss how the three dimensional development of the current may play a role. The convection currents associated with cabbeling in three dimensions will undergo vortex tilting and stretching as the dense fluid sinks. This may be more prevalent for the low Θ limit, as the mixing dynamics are limited by the small temperature differences, so an added mixing mechanism may have a more profound effect on the dynamics.

Chapter 6

Concluding Remarks

In thesis, we have presented a series of numerical process studies with the goal of capturing, understanding, and describing characteristic dynamics of different temperature intervals of the freshwater non-linear equation of state (NLEOS).

In chapter 3, we presented a series of process studies that represented the evolution of a fresh water system in the late winter. In this setup, a volumetric heating source (representing incident solar radiation) preferentially added heat near the surface. The heating induced small temperature and density changes within the flow, and since the temperature of the flow was below $\tilde{T}_{md}$ everywhere, convective plumes were generated near the surface. We investigated how these plumes developed in the presence of an otherwise stable background shear current. We showed that for a sufficiently strong background current, cores of the convective plumes were aligned in the direction of the current. It was hypothesized that this led to a systematic vertical flux of streamwise momentum by the convective plumes which triggered vortex tilting and stretching, and the result was a turbulent-like state. It was noted that common mixed layer parameterizations (the KPP was specifically mentioned in that chapter) calculate vertical heat fluxes by assuming a fully turbulent water column, which implicitly assumes a sufficiently large Reynolds number. However, the results of this chapter demonstrate that in spite of the very low Reynolds number of the simulations (and therefore a traditionally non-turbulent flow), the vortex tilting and stretching are important mechanisms in the degeneration of the water column and subsequent mixing. This could potentially pose a problem for the accurate parameterization of convection driven by solar radiation beneath ice. More on this can be found in section 6.1.

In chapter 4, we presented a series of simulations of gravity currents in a monotoni-

cally increasing but non-linear interval of the NLEOS. The core of the series of numerical experiments was a comparison between two classes of gravity currents with temperature differences (and density differences) of equal magnitudes. The first class was a series of surface currents flowing into a denser ambient, while the second class was a series of dense currents flowing into a lighter ambient. We saw that the lighter currents that flowed along the top surface experienced a decrease in the head speed and head location relative to denser currents that flowed along the bottom surface. We also demonstrated that currents flowing along the top surface had a larger vertical extent in the tail region and that their head heights decreased more rapidly when compared to current flowing along the bottom surface. Additionally, we identified key differences in the density and temperature distributions of the currents due to mixing in the body and tail of the currents. We closed this chapter with a discussion on how the results presented within may related to what we term "weak cabbeling" (the density of a mixed parcel of fluid is denser than the average density of the parent parcels of fluid) in fresh bodies of water.

Finally, in chapter 5 we presented a series of simulations of gravity currents where ambient and intruding temperatures were on opposite side of $\tilde{T}_{md}$. We used this interval to describe how cabbeling (the density of a mixed parcel of fluid is denser than the density of either parent parcel of fluid) affects the evolution of gravity currents. Temperatures were chosen so that currents initially flowed along the surface of the domain (called hypopycnal currents in that chapter). We found that while the hypopycnal currents propagated down the tank, cabbeling occurred in the tail and body of the current. Once enough fluid was extracted, the current ceased its propagation. The mixed fluid settled on the bottom and a coherent bottom flowing current formed (called a hyperpycnal current in that chapter). The dependence of the maximum extent of the hypopycnal current on Θ (the definition can be found in (5.4)) and h (the depth of the domain) were probed and discussed. It was shown as Θ was increased, cabbeling became a secondary effect allowing the currents to travel a greater distance. Furthermore, deeper domains led to a shorter maximum extent due to the relatively small value of the Grashof number. We also discussed some of the characteristics of the hyperpycnal currents such as their density and temperature distribution. We found that once the hyperpycnal current formed, larger values of Θ led to larger current area but narrower distributions of density and temperature about their mean values.

6.1 Future Work

There are several direct extensions of this work that could be considered. Specific extensions to each of the projects have been highlighted in their respective chapters, but here we will suggest several broad directions that work described in this thesis as a whole could take in the future.

Throughout this entire work, it has been assumed that greatest contribution to density variation is from the temperature. However, due to the smallness of the density differences in the cold water regime due to variations in temperature (in the neighborhood of 0.005%) it is clear that comparable density variations can come from slight variations in salinity (for example, Cortés and MacIntyre (2020) saw examples of column-wide variations in density due to salinity on the order of 0.001% in a small arctic lake) as well as variations in the hydrostatic pressure. As an example, let us specifically consider the pressure effects.

We can perform a Taylor expansion of the density about the temperature of maximum density $\tilde{T}_{md}$ and a reference pressure P_0 (this could be the surface pressure). Note that since we are expanding the density about $\tilde{T}_{md}$, the first term in the expansion of temperature is zero since $\alpha = 0$ at $\tilde{T}_{md}$. This leaves:

$$\rho(T,p) = \rho_0 \left(1 + \frac{1}{\rho_0}\left(\frac{\partial \rho}{\partial p}\right)_T (p - P_0) + \frac{1}{2\rho_0}\left(\frac{\partial^2 \rho}{\partial T^2}\right)_p (T - \tilde{T}_{md})^2 + ...\right), \tag{6.1}$$

where $\rho_0 = \rho(T_0, P_0)$ and we have omitted higher order terms including cross terms. We can express the scaled perturbation about the reference state as

$$\frac{\rho'}{\rho_0} = K\,(p - P_0) + \frac{1}{2}C(T - \tilde{T}_{md})^2 + ... \tag{6.2}$$

where the isothermal compressibility and the temperature derivative of the isobaric thermal expansivity are given by

$$K = \frac{1}{\rho_0}\left(\frac{\partial \rho}{\partial p}\right)_T, \quad C = \frac{1}{\rho_0}\left(\frac{\partial^2 \rho}{\partial T^2}\right)_p. \tag{6.3}$$

respectively. We can replace $p - P_0$ with $p^H + p'$ using (2.15) (recall that $p^H = P_0 + \rho_0 g z$). We can assume that perturbations to the pressure field by motion are much smaller in magnitude than p^H so that $p^H \gg p'$. This allows us to write the normalized perturbation ρ'/ρ_0 as

$$\frac{\rho'}{\rho_0} = K\rho_0 g z + \frac{1}{2}C(T - \tilde{T}_{md})^2 + ... \tag{6.4}$$

We are interested in the relative importance of the pressure dependency of the density fluctuation (the first term on the right of (6.4)) versus the temperature dependency of the density fluctuation (the second term on the right of (6.4)). Thus, for changes in ρ'/ρ_0 due to pressure variations over a depth z to be comparable to those due to temperature variations, those temperature variations about $\tilde{T}_{md}$ must be

$$T - \tilde{T}_{md} \sim \sqrt{\frac{K\rho_0 g z}{C}}. \tag{6.5}$$

Over the temperature range that this thesis is concerned with, K does not deviate strongly about $5 \times 10^{-5}\,\mathrm{atm}^{-1}$ (Millero et al., 1980), we can assume that $C \approx 10^{-6}\,^{\circ}\mathrm{C}^{-2}$ (see the constant C in table 5.2 for an estimate), $g \sim 10\,\mathrm{m/s^2}$ and $\rho_0 = 1000\,\mathrm{kg/m^3}$. Since the domain depths presented in this thesis are all on the scale of about one metre, density changes due to pressure will need to be accounted for if the deviations of temperature about $\tilde{T}_{md}$ are smaller than about $0.3\,^{\circ}\mathrm{C}$. Of course, depths in the field are much larger than one metre, so variations in density due to pressure variations are comparable to much larger temperature deviations about $\tilde{T}_{md}$. This is specifically relevant to the process study described in chapter 3. For initial temperatures near $\tilde{T}_{md}$, the temperature of the flow becomes closer to $\tilde{T}_{md}$ due to incident the solar radiation. As we showed in chapter 3, the solar radiation generates an unstable density gradient, and instabilities occur. However, the resultant density differences generated by the heating may be small enough such that they are comparable to the stable density stratification caused by the hydrostatic pressure variation. This means that a hydrostatic background state creates a stable background stratification that the instabilities must overcome to grow to finite amplitude.

The results of chapter 3 also bring up questions about the applicability of mixed layer models in cold waters. The K-Profile Paramerization (KPP), was mentioned as an example, and more information can be found in Large et al. (1994) and Van Roekel et al. (2018). The KPP (while useful in many contexts) uses Monin-Obhukov (M-O) stability functions to assess whether or not the water column is stable. If it is unstable, non-local mixing occurs and heat is instantaneously redistributed throughout the domain. M-O theory assumes a fully developed turbulent state to calculate the M-O length scale, which in turn determines the stability of the water column. The results of chapter 3 have a flow Reynolds number that is too small to properly develop an inertial sub-range, so the assumption of a fully turbulent mixed layer is not necessarily satisfied. More generally, it is not clear that the water column beneath ice in the field is fully turbulent such that it has an inertial sub-range (this was briefly touched on in section 3.5.2). Thus, for flows beneath ice where turbulence is weak, the turbulent fluxes of heat may not be properly estimated. Thus, the efficacy of mixed layer models in cold water beneath ice should be studied directly.

Furthermore, Van Roekel et al. (2018) highlights that non-local transport of horizontal momentum is absent in most KPP implementations, but it is clear from these results of chapter 3 that there is evidence of coupling of the momentum from the background current to the plume structures that arise from the destabilizing thermal forcing. Thus, it should be determined whether or not this coupling is well represented by a non-local term, or should be parameterized by something completely different.

For readers more interested in turbulent structures, the simulations presented in chapters 4 and 5 could be re-run in three dimensions at large Gr (see (4.9)). By assuming that the flow evolves in only two dimensions (as we have done in those chapters), the potential for turbulence generation by vortex tilting and stretching is removed. It has been shown that turbulent structures in the tail of a gravity current have some impact on the head location and head speed of the current late in its evolution. Cantero et al. (2008) and references within discussed this impact and found that when simulating gravity currents in two dimensions, two-dimensional coherent vortical structures in the tail of the current led to a reduction in the driving pressure gradient of the flow. They compared these results to three dimensional cases at the same Reynolds number and found that the pressure reduction within the tail was weaker for the three dimensional cases. This led to a larger head speed in the inertial and viscous regimes for the three dimensional cases compared to the two dimensional cases.

The results presented in chapter 4 suggest noticeable differences in the head speed and location for the surface flowing and bottom flowing currents; currents that are denser than the ambient (they flow along the bottom surface) travel a greater distance in a given time than a current that is lighter than the ambient. If the gravity currents presented in chapter 4 are allowed to evolve in three dimensions, would we see a similar manifestation of the reduced pressure gradient discussed in Cantero et al. (2008)? Would this minimize the differences between each class of current, or would the effects of the reduced pressure gradient appear after each class of current were allowed to separate?

Furthermore, are the results of chapter 5 significantly affected by three-dimensionality? Vortex tilting and stretching may enhance the rate of mixing when compared to two-dimensional simulations. Could this affect the rate that the hypopycnal currents mix with the ambient? If mixing occurs more rapidly over the course of hypopycnal current evolution, there may be implications for the rate of formation and the characteristics of the hyperpycnal current. If mixing happens more rapidly and more efficiently, the hyperpycnal current temperature distributions may be narrower and their mean temperature may be further from the ambient, due to there being a smaller volume of entrained ambient fluid. This could allow a three-dimensional hyperpyncal current to travel further than a comparable two-dimensional case.

Finally, for those more interested in laboratory work, the studies presented within this thesis should be performed in a laboratory to validate some of the results. For example, it is common practice in laboratory studies of gravity currents to track the head location and infer the head speed of the currents. For example, the results of figures 4.5, could be directly compared to laboratory data. As another example, the maximum extent of hypopycnal currents could be tracked to determine the accuracy of figure 5.9.

References

Akula, B., Andrews, M. J., and Ranjan, D. (2013). Effect of shear on Rayleigh-Taylor mixing at small Atwood number. *Physical Review E - Statistical, Nonlinear, and Soft Matter Physics*, 87(3):1–14.

Alwin, T., Baker, D., Chaffin, J., Charlton, M., Chruscicki, J., Ciborowski, J., Cooke, S., Depinto, J., Dudley, D., Evans, M. A., George, S., Hesse, G., Hiriart-Baer, V., Horvatin, P., Howell, T., Kreis, R., Reutter, J., Scavia, D., Stow, C., Stumpf, R., and Yerubandi, R. (2015). Recommended Phosphorus Loading Targets for Lake Erie. Technical report, Annex 4 Objectives and Targets Task Team Final Report to the Nutrients Annex Subcommittee.

Andrews, M. J. and Dalziel, S. B. (2010). Small Atwood number Rayleigh-Taylor experiments. *Philosophical Transactions of the Royal Society A: Mathematical, Physical and Engineering Sciences*, 368(1916):1663–1679.

Anonymous (2018). NTC thermistor sensor performance.

Batchelor, G. K. (2000). *An Introduction to Fluid Dynamics*. Cambridge University Press, Cambridge.

Beall, B. F., Twiss, M. R., Smith, D. E., Oyserman, B. O., Rozmarynowycz, M. J., Binding, C. E., Bourbonniere, R. A., Bullerjahn, G. S., Palmer, M. E., Reavie, E. D., Waters, L. M., Woityra, L. W., and McKay, R. M. (2016). Ice cover extent drives phytoplankton and bacterial community structure in a large north-temperate lake: implications for a warming climate. *Environmental microbiology*, 18(6):1704–1719.

Benilov, E. S., Naulin, V., and Rasmussen, J. J. (2002). Does a sheared flow stabilize inversely stratified fluid? *Physics of Fluids*, 14(5):1674–1680.

Bird, L. A., Moyer, A. N., Moore, R. D., and Koppes, M. N. (2022). Hydrology and thermal regime of an ice-contact proglacial lake: Implications for stream temperature and lake evaporation. *Hydrological Processes*, 36(4):1–20.

Boehrer, B., Fukuyama, R., and Chikita, K. (2008). Stratification of very deep, thermally stratified lakes. *Geophysical Research Letters*, 35(16):8–12.

Boehrer, B. and Schultze, M. (2008). Stratification of lakes. *Reviews of Geophysics*, 46(2):1–27.

Boffetta, G., Mazzino, A., Musacchio, S., and Vozella, L. (2009). Kolmogorov scaling and intermittency in Rayleigh-Taylor turbulence. *Physical Review E - Statistical, Nonlinear, and Soft Matter Physics*, 79(6):1–4.

Boffetta, G., Mazzino, A., Musacchio, S., and Vozella, L. (2010). Statistics of mixing in three-dimensional Rayleigh-Taylor turbulence at low Atwood number and Prandtl number one. *Physics of Fluids*, 22(3):1–8.

Bouffard, D. and Wüest, A. (2019). Convection in Lakes. *Annual Review of Fluid Mechanics*, 51:189–215.

Bouffard, D., Zdorovennova, G., Bogdanov, S., Efremova, T., Lavanchy, S., Palshin, N., Terzhevik, A., Vinnå, L. R., Volkov, S., Wüest, A., Zdorovennov, R., and Ulloa, H. N. (2019). Under-ice convection dynamics in a boreal lake. *Inland Waters*, 9(2):142–161.

Bouillaut, V., Lepot, S., Aumaître, S., and Gallet, B. (2019). Transition to the ultimate regime in a radiatively driven convection experiment. *Journal of Fluid Mechanics*, 861:1–12.

Bruce, J. P. and Higgins, P. M. (2012). Great Lakes Water Quality Agreement. In *Eighth International Conference on Water Pollution Research*, pages 13–31. Elsevier.

Brydon, D., Sun, S., and Bleck, R. (1999). A new approximation of the equation of state for seawater, suitable for numerical ocean models. *Journal of Geophysical Research*, 104(1):1537–1540.

Burchard, Hans and Bolding, Karsten and Umlauf, L. (2011). *General Estuarine Transport Model (GETM)*.

Campin, J.-M., Heimbach, P., Losch, M., Forget, G., Adcroft, A., Menemenlis, D., Hill, C., Jahn, O., Scott, J., Mazloff, M., Doddridge, E., Fenty, I., Bates, M., Martin, T.,

Abernathey, R., Smith, T., Lauderdale, J., Deremble, B., Dussin, R., Bourgault, P., and McRae, A. T. T. (2019). *MITgcm User Manual*.

Cantero, M., Balachandar, S., García, M. H., and Bock, D. (2008). Turbulent structures in planar gravity currents and their influence on the flow dynamics. *Journal of Geophysical Research: Oceans*, 113(8):1–22.

Cantero, M. I., Lee, J. R., Balachandar, S., and Garcia, M. H. (2007). On the front velocity of gravity currents. *Journal of Fluid Mechanics*, 586:1–39.

Carmack, E. (1979). Combined influence of inflow and lake temperatures of spring circulation in a riverine lake. *Journal of Physical Oceanography*, 9:422–439.

Carrivick, J. L. and Tweed, F. S. (2013). Proglacial lakes: character, behaviour and geological importance. *Quaternary Science Reviews*, 78:34–52.

Caulfield, C. P. (2021). Mixing in turbulent stratified flows. *Annual Review of Fluid Mechanics*, 53:113–145.

Cortés, A. and MacIntyre, S. (2020). Mixing processes in small arctic lakes during spring. *Limnology and Oceanography*, 65(2):260–288.

Davarpanah Jazi, S. and Wells, M. G. (2020). Dynamics of settling-driven convection beneath a sediment-laden buoyant overflow: Implications for the length-scale of deposition in lakes and the coastal ocean. *Sedimentology*, 67(1):699–720.

Deepwell, D. (2018). *High resolution simulations of mode-2 internal waves : transport, shoaling, and the influence of rotation*. PhD thesis, University of Waterloo.

Deepwell, D., Clarry, C., Subich, C., and Stastna, M. (2021). Vortex generation due to internal solitary wave propagation past a sidewall constriction. *Journal of Fluid Mechanics*, 913:1–26.

Deepwell, D. and Stastna, M. (2016). Mass transport by mode-2 internal solitary-like waves. *Physics of Fluids*, 28(5).

Deepwell, D., Stastna, M., Carr, M., and Davies, P. A. (2017). Interaction of a mode-2 internal solitary wave with narrow isolated topography. *Physics of Fluids*, 29(7).

Deepwell, D., Stastna, M., Carr, M., and Davies, P. A. (2019). Wave generation through the interaction of a mode-2 internal solitary wave and a broad, isolated ridge. *Physical Review Fluids*, 4(9):94802.

Dinçer, Î. and Zamfirescu, C. (2016). *Drying phenomena: theory and applications*. John Wiley & Sons.

Djoumna, G., Lamb, K. G., and Rao, Y. R. (2014). Sensitivity of the parameterizations of vertical mixing and radiative heat fluxes on the seasonal evolution of the thermal structure of Lake Erie. *Atmosphere - Ocean*, 52(4):294–313.

Faulkner, A., Bulgin, C. E., and Merchant, C. J. (2021). Characterising industrial thermal plumes in coastal regions using 3-d numerical simulations. *Environmental Research Communications*, 3(4).

Flato, G. M. (2011). Earth system models: an overview. *Wiley Interdisciplinary Reviews: Climate Change*, 2(6):783–800.

Frigo, M. and Johnson, S. G. (2005). The design and implementation of FFTW3. *Proceedings of the IEEE*, 93(2):216–231.

Fujisaki, A., Wang, J., Bai, X., Leshkevich, G., and Lofgren, B. (2013). Model-simulated interannual variability of Lake Erie ice cover, circulation, and thermal structure in response to atmospheric forcing, 2003-2012. *Journal of Geophysical Research: Oceans*, 118(9):4286–4304.

Fyke, J., Sergienko, O., Löfverström, M., Price, S., and Lenaerts, J. T. (2018). An overview of interactions and feedbacks between ice sheets and the Earth system. *Reviews of Geophysics*, 56(2):361–408.

Gebhart, B., Jaluria, Y., Mahajan, R. L., and Sammakia, B. (1988). *Buoyancy-induced flows and transport*. New York, NY (USA); Hemisphere Publishing.

Gladstone, C., Ritchie, L. J., Sparks, R. S., and Woods, A. W. (2004). An experimental investigation of density-stratified inertial gravity currents. *Sedimentology*, 51(4):767–789.

Grace, A., Stastna, M., and Poulin, F. J. (2019). Numerical simulations of the shear instability and subsequent degeneration of basin scale internal standing waves. *Physical Review Fluids*, 4(1):14802.

Grace, A. P., Stastna, M., Lamb, K. G., and Scott, K. A. (2021). Asymmetries in gravity currents attributed to the nonlinear equation of state. *Journal of Fluid Mechanics*, 915:1–18.

Grace, A. P., Stastna, M., Lamb, K. G., and Scott, K. A. (2022). Numerical simulations of the three-dimensionalization of a shear flow in radiatively forced cold water below the density maximum. *Physical Review Fluids*, 7(2):1–24.

Grossmann, S. and Lohse, D. (2000). Scaling in thermal convection: a unifying theory. *Journal of Fluid Mechanics*, 407:27–56.

Hanson, T., Stastna, M., and Coutino, A. (2021). Stratified shear instability in the cabbeling regime. *Physical Review Fluids*, 6(8):84802.

Harnanan, S., Soontiens, N., and Stastna, M. (2015). Internal wave boundary layer interaction: a novel instability over broad topography. *Physics of Fluids*, 27(1).

Harnanan, S., Stastna, M., and Soontiens, N. (2017). The effects of near-bottom stratification on internal wave induced instabilities in the boundary layer. *Physics of Fluids*, 29(1).

Härtel, C., Carlsson, F., and Thunblom, M. (2000a). Analysis and direct numerical simulation of the flow at a gravity-current head. Part 2. The lobe-and-cleft instability. *Journal of Fluid Mechanics*, 418:213–229.

Härtel, C., Meiburg, E. H., and Necker, F. (2000b). Analysis and direct numerical simulation of the flow at a gravity-current head. Part 1. Flow topology and front speed for slip and no-slip boundaries. *Journal of Fluid Mechanics*, 418:189–212.

Hodges, B. and Dallimore, C. (2006). Estuary, Lake and Coastal Ocean Model : ELCOM v2. 2 Science Manual. *Water*, page 62.

Holland, P. R. and Kay, A. (2003). A review of the physics and ecological implications of the thermal bar circulation. *Limnologica*, 33(3):153–162.

Holland, P. R., Kay, A., and Botte, V. (2001). A Numerical Study of the Dynamics of the Riverine Thermal Bar in a Deep Lake. *Environmental Fluid Mechanics*, 1(3):311–332.

Huppert, H. and Simpson, J. E. (1980). The slumping of gravity currents. *Journal of Fluid Mechanics*, 99(4):785–799.

Huppert, H. E. (2006). Gravity currents: a personal perspective. *Journal of Fluid Mechanics*, 554:299–322.

Imberger, J. and Hamblin, P. F. (1982). Dynamics of lakes, reservoirs, and cooling ponds. *Annual Review of Fluid Mechanics*, 14:153–187.

Jackett, D. R. and McDougall, T. J. (1995). Minimal adjustment of hydrographic profiles to achieve static stability. *Journal of Atmospheric and Oceanic Technology*, 12(2):381–389.

Jansen, J., MacIntyre, S., Barrett, D. C., Chin, Y., Cortés, A., Forrest, A. L., Hrycik, A. R., Martin, R., McMeans, B. C., Rautio, M., and Schwefel, R. (2021). Winter limnology: how do hydrodynamics and biogeochemistry shape ecosystems under ice? *Journal of Geophysical Research: Biogeosciences*, 126(6):1–29.

Jenkins, A., Dutrieux, P., Jacobs, S., McPhail, S. D., Perrett, J. R., Webb, A., and White, D. (2010). Observations beneath Pine Island Glacier in West-Antarctica and implications for its retreat. *Nature Geoscience*, 3(7):468–472.

Jerlov, N. (1976). *Marine Optics*. Elsevier.

Jonas, T., Stips, A., Eugster, W., and Wüest, A. (2003). Observations of a quasi shear-free lacustrine convective boundary layer: Stratification and its implications on turbulence. *Journal of Geophysical Research: Oceans*, 108(10):1–15.

Kantha, L. H. and Clayson, C. A. (2000). Surface exchange processes. In *Small scale processes in geophysical fluid flows*, chapter 4, pages 418–507. Elsevier Ltd.

Kasper, J. L. and Weingartner, T. J. (2015). The spreading of a buoyant plume beneath a landfast ice cover. *Journal of Physical Oceanography*, 45(2):478–494.

Keisuke, F., Masamoto, N., and Hiromasa, U. (1991). Coherent structure of turbulent longitudinal vortices in unstably-stratified turbulent flow. *International Journal of Heat and Mass Transfer*, 34(9):2373–2385.

Kirillin, G., Leppäranta, M., Terzhevik, A., Granin, N., Bernhardt, J., Engelhardt, C., Efremova, T., Golosov, S., Palshin, N., Sherstyankin, P., Zdorovennova, G., and Zdorovennov, R. (2012). Physics of seasonally ice-covered lakes: a review. *Aquatic Sciences*, 74(4):659–682.

Kundu, P. K. (1990). *Fluid Mechanics*. Academic Press, 1st edition.

Kuo, H. L. (1963). Perturbations of plane Couette flow in stratified fluid and origin of cloud streets. *Physics of Fluids*, 6(2):195–211.

Large, W. G., McWilliams, J. C., and Doney, S. C. (1994). Oceanic vertical mixing: a review and a model with a nonlocal boundary layer parameterization. *Reviews of Geophysics*, 32(4):363–403.

Legare, S., Grace, A., and Stastna, M. (2021). Double-diffusive instability in a thin vertical channel. *Physics of Fluids*, 33(11).

Lemons, D. (2009). *Mere Thermodynamics*. JHU Press, Baltimore.

Leon, L. F., Smith, R. E., Hipsey, M. R., Bocaniov, S. A., Higgins, S. N., Hecky, R. E., Antenucci, J. P., Imberger, J. A., and Guildford, S. J. (2011). Application of a 3D hydrodynamic-biological model for seasonal and spatial dynamics of water quality and phytoplankton in Lake Erie. *Journal of Great Lakes Research*, 37(1):41–53.

Lepot, S., Aumaître, S., and Gallet, B. (2018). Radiative heating achieves the ultimate regime of thermal convection. *Proceedings of the National Academy of Sciences of the United States of America*, 115(36):8937–8941.

Malm, J., Bengtsson, L., Terzhevik, A., Boyarinov, P., Glinsky, A., Palshin, N., and Petrov, M. (1998). Field study on currents in a shallow, ice-covered lake. *Limnology and Oceanography*, 43(7):1669–1679.

Mashayek, A. and Peltier, W. R. (2012). The zoo of secondary instabilities precursory to stratified shear flow transition. Part 2 the influence of stratification. *Journal of Fluid Mechanics*, 708:45–70.

Maxworthy, T. (1999). The dynamics of sedimenting surface gravity currents. *Journal of Fluid Mechanics*, 392:27–44.

McDougall, T. J. (1987). Thermobaricity, cabbeling, and water-mass conversion. *Journal of Geophysical Research: Oceans*, 92:5448–5464.

McDougall, T. J., Jackett, D. R., Wright, D. G., and Feistel, R. (2003). Accurate and computationally efficient algorithms for potential temperature and density of seawater. *Journal of Atmospheric and Oceanic Technology*, 20(5):730–741.

Meiburg, E. and Kneller, B. (2010). Turbidity currents and their deposits. *Annual Review of Fluid Mechanics*, 42:135–156.

Mikhailenko, V. S., Scime, E. E., and Mikhailenko, V. V. (2005). Stability of stratified flow with inhomogeneous shear. *Physical Review E - Statistical, Nonlinear, and Soft Matter Physics*, 71(2).

Millero, F., Chen, C., Bradshaw, A., and Schleicher, K. (1980). A new high pressure equation of state for seawater. *Deep Sea Research Part A. Oceanographic Research Papers*, 27(1):255–264.

Notaro, M., Holman, K., Zarrin, A., Fluck, E., Vavrus, S., and Bennington, V. (2013). Influence of the laurentian great lakes on regional climate. *Journal of Climate*, 26(3):789–804.

Olsthoorn, J. and Stastna, M. (2014). Numerical investigation of internal wave-induced sediment motion: Resuspension versus entrainment. *Geophysical Research Letters*, 41(8):2876–2882.

Olsthoorn, J., Tedford, E. W., and Lawrence, G. A. (2019). Diffused-interface Rayleigh-Taylor instability with a nonlinear equation of state. *Physical Review Fluids*, 4(9):1–23.

Osadchiev, A., Barymova, A., Sedakov, R., Zhiba, R., and Dbar, R. (2020). Spatial structure, short-temporal variability, and dynamical features of small river plumes as observed by aerial drones: Case study of the Kodor and Bzyp river plumes. *Remote Sensing*, 12(18).

Ouillon, R., Meiburg, E., and Sutherland, B. R. (2019). Turbidity currents propagating down a slope into a stratified saline ambient fluid. *Environmental Fluid Mechanics*, 19(5):1143–1166.

Oveisy, A., Rao, Y. R., Leon, L. F., and Bocaniov, S. A. (2014). Three-dimensional winter modeling and the effects of ice cover on hydrodynamics, thermal structure and water quality in Lake Erie. *Journal of Great Lakes Research*, 40(S3):19–28.

Ozersky, T., Bramburger, A. J., Elgin, A. K., Vanderploeg, H. A., Wang, J., Austin, J. A., Carrick, H. J., Chavarie, L., Depew, D. C., Fisk, A. T., Hampton, S. E., Hinchey, E. K., North, R. L., Wells, M. G., Xenopoulos, M. A., Coleman, M. L., Duhaime, M. B., Fujisaki-Manome, A., McKay, R. M., Meadows, G. A., Rowe, M. D., Sharma, S., Twiss, M. R., and Zastepa, A. (2021). The changing face of winter: lessons and questions from the Laurentian Great Lakes. *Journal of Geophysical Research: Biogeosciences*, 126(6).

Ozgökmen, T. M. and Esenkov, O. E. (1998). Asymmetric salt fingers induced by a nonlinear equation of state. *Physics of Fluids*, 10(8):1882–1890.

Penney, J. and Stastna, M. (2016). Direct numerical simulation of double-diffusive gravity currents. *Physics of Fluids*, 28(8).

Pirozzoli, S., Bernardini, M., Verzicco, R., and Orlandi, P. (2017). Mixed convection in turbulent channels with unstable stratification. *Journal of Fluid Mechanics*, 821:482–516.

Pope, S. (2000). *Turbulent Flows*. Cambridge University Press.

Powers, S. M. and Hampton, S. E. (2016). Winter limnology as a new frontier. *Limnology and Oceanography Bulletin*, 25(4):103–108.

Ramón, C. L., Ulloa, H. N., Doda, T., Winters, K. B., and Bouffard, D. (2021). Bathymetry and latitude modify lake warming under ice. *Hydrology and Earth System Sciences*, 25(4):1813–1825.

Reavie, E. D., Cai, M., Twiss, M. R., Carrick, H. J., Davis, T. W., Johengen, T. H., Gossiaux, D., Smith, D. E., Palladino, D., Burtner, A., and Sgro, G. V. (2016). Winter-spring diatom production in Lake Erie is an important driver of summer hypoxia. *Journal of Great Lakes Research*, 42(3):608–618.

Rizk, W., Kirillin, G., and Leppäranta, M. (2014). Basin-scale circulation and heat fluxes in ice-covered lakes. *Limnology and Oceanography*, 59(2):445–464.

Schmid, M., Budnev, N. M., Granin, N. G., Sturm, M., Schurter, M., and Wüest, A. (2008). Lake Baikal deepwater renewal mystery solved. *Geophysical Research Letters*, 35(9):1–5.

Schoof, C. (2010). Glaciology: beneath a floating ice shelf. *Nature Geoscience*, 3(7):450–451.

Shakespeare, C. J. and Thomas, L. N. (2017). A new mechanism for mode water formation involving cabbeling and frontogenetic strain at thermohaline fronts. Part II: numerical simulations. *Journal of Physical Oceanography*, 47(7):1755–1773.

Shimaraev, M. N., Granin, N. G., and Zhdanov, A. A. (1993). Deep ventilation of Lake Baikal waters due to spring thermal bars. *Limnology and Oceanography*, 38(5):1068–1072.

Simpson, J. E. (1982). Gravity currents in the laboratory, atmosphere, and ocean. *Annual Review of Fluid Mechanics*, 14(1):213—-234.

Simpson, J. E. (1999). *Gravity currents: In the environment and the laboratory*. Cambridge University Press, 2 edition.

Simpson, J. J. and Dickey, T. (1981a). The relationship between downward irradiance and upper ocean structure. *Journal of Physical Oceanography*, 11(March):309–323.

Simpson, J. J. and Dickey, T. D. (1981b). Alternative parameterizations of downward irradiance and their dynamical significance. *Journal of Physical Oceanography*, 11(June):876–882.

Smyth, W. D., Moum, J. N., and Nash, J. D. (2011). Narrowband oscillations in the upper equatorial ocean. Part II: properties of Shear instabilities. *Journal of Physical Oceanography*, 41(3):412–428.

Snow, K. and Sutherland, B. R. (2014). Particle-laden flow down a slope in uniform stratification. *Journal of Fluid Mechanics*, 755:251–273.

Stevens, B. (2005). Atmospheric moist convection. *Annual Review of Earth and Planetary Sciences*, 33:605–643.

Stewart, K. D., Haine, T. W. N., McC. Hogg, A., and Roquet, F. (2017). On cabbeling and thermobaricity in the surface mixed layer. *Journal of Physical Oceanography*, 47(7):1775–1787.

Subich, C. J., Lamb, K. G., and Stastna, M. (2013). Simulation of the Navier-Stokes equations in three dimensions with a spectral collocation method. *International Journal for Numerical Methods in Fluids*, 73(2):103–129.

Sutherland, B. R., Gingras, M. K., Knudson, C., Steverango, L., and Surma, C. (2018). Particle-bearing currents in uniform density and two-layer fluids. *Physical Review Fluids*, 3(2):1–15.

Sutherland, B. R., Rosevear, M. G., and Cenedese, C. (2020). Laboratory experiments modeling the transport and deposition of sediments by glacial plumes rising under an ice shelf. *Physical Review Fluids*, 5(1):13802.

Szopa, S., Naik, V., Adhikary, B., Artaxo, P., Berntsen, T., Collins, W., Fuzzi, S., Gallardo, L., Kiendler Scharr, A., Klimont, Z., Liao, H., Unger, N., and Zanis, P. (2021). *Short-Lived Climate Forcers In Climate Change 2021: The Physical Science Basis. Contribution of Working Group I to the Sixth Assessment Report of the Intergovernmental Panel on Climate Change*.

Tapiador, F. J., Navarro, A., Moreno, R., Sánchez, J. L., and García-Ortega, E. (2020). Regional climate models: 30 years of dynamical downscaling. *Atmospheric Research*, 235(October 2019):104785.

Thomas, L. N. and Shakespeare, C. J. (2015). A new mechanism for mode water formation involving cabbeling and frontogenetic strain at thermohaline fronts. *Journal of Physical Oceanography*, 45(9):2444–2456.

Tsydenov, B. O., Kay, A., and Starchenko, A. V. (2016). Numerical modeling of the spring thermal bar and pollutant transport in a large lake. *Ocean Modelling*, 104:73–83.

Twiss, M. R., McKay, R. M., Bourbonniere, R. A., Bullerjahn, G. S., Carrick, H. J., Smith, R. E., Winter, J. G., D'souza, N. A., Furey, P. C., Lashaway, A. R., Saxton, M. A., and Wilhelm, S. W. (2012). Diatoms abound in ice-covered Lake Erie: an investigation of offshore winter limnology in Lake Erie over the period 2007 to 2010. *Journal of Great Lakes Research*, 38(1):18–30.

Ulloa, H. N., Winters, K. B., Wüest, A., and Bouffard, D. (2019). Differential heating drives downslope flows that accelerate mixed-layer warming in ice-covered waters. *Geophysical Research Letters*, 46(23):13872–13882.

Vallis, G. K. (2006). *Atmospheric and Oceanic Fluid Dynamics*. Cambridge University Press.

Van Roekel, L., Adcroft, A. J., Danabasoglu, G., Griffies, S. M., Kauffman, B., Large, W., Levy, M., Reichl, B. G., Ringler, T., and Schmidt, M. (2018). The KPP boundary layer scheme for the ocean: revisiting its formulation and benchmarking one-dimensional simulations relative to LES. *Journal of Advances in Modeling Earth Systems*, 10(11):2647–2685.

Vitousek, S. and Fringer, O. B. (2011). Physical vs. numerical dispersion in nonhydrostatic ocean modeling. *Ocean Modelling*, 40(1):72–86.

Vreugdenhil, C. A. and Gayen, B. (2021). Ocean convection. *Fluids*, 6(10):1–20.

Walker, D. P., Brandon, M. A., Jenkins, A., Allen, J. T., Dowdeswell, J. A., and Evans, J. (2007). Oceanic heat transport onto the Amundsen Sea shelf through a submarine glacial trough. *Geophysical Research Letters*, 34(2):2–5.

Weingartner, T. J., Danielson, S. L., Potter, R. A., Trefry, J. H., Mahoney, A., Savoie, M., Irvine, C., and Sousa, L. (2017). Circulation and water properties in the landfast ice zone of the Alaskan Beaufort Sea. *Continental Shelf Research*, 148(September):185–198.

Wells, M. G. and Dorrell, R. M. (2021). Turbulence processes within turbidity currents. *Annual Review of Fluid Mechanics*, 53:59–83.

Wilcox, D. C. (1988). Reassessment of the scale-determining equation for advanced turbulence models. *AIAA*, 26(11):1299–1310.

Winters, K. B., Lombard, P. N., Riley, J. J., and D'Asaro, E. A. (1995). Available potential energy and mixing in density-stratified fluids. *Journal of Fluid Mechanics*, 289:115–128.

Wüest, A. and Lorke, A. (2003). Small scale hydrodynamics in lakes. *Annual Review of Fluid Mechanics*, 35(1):373–412.

Xu, C. and Stastna, M. (2018). On the interaction of short linear internal waves with internal solitary waves. *Nonlinear Processes in Geophysics*, 25(1):1–17.

Xu, C. and Stastna, M. (2019). Internal waves in a shear background current: transition from solitary-wave regime to dispersive-wave regime. *Physical Review Fluids*, 4(9):1–26.

Xu, C. and Stastna, M. (2020). Instability and cross-boundary-layer transport by shoaling internal waves over realistic slopes. *Journal of Fluid Mechanics*, 895:1–12.

Xu, C., Stastna, M., and Deepwell, D. (2019). Spontaneous instability in internal solitary-like waves. *Physical Review Fluids*, 4(1):1–21.

Xu, C., Subich, C., and Stastna, M. (2016). Numerical simulations of shoaling internal solitary waves of elevation. *Physics of Fluids*, 28(7).

Yang, B., Wells, M. G., Li, J., and Young, J. (2020). Mixing, stratification, and plankton under lake-ice during winter in a large lake: implications for spring dissolved oxygen levels. *Limnology and Oceanography*, 65(11):2713–2729.

Yang, B., Young, J., Brown, L., and Wells, M. (2017). High-frequency observations of temperature and dissolved oxygen reveal under-ice convection in a large lake. *Geophysical Research Letters*, 44(24):12,218–12,226.

Zhou, Y., Michalak, A. M., Beletsky, D., Rao, Y. R., and Richards, R. P. (2015). Record-breaking Lake Erie hypoxia during 2012 drought. *Environmental Science and Technology*, 49(2):800–807.

Appendix

The derivation for the Viscous Taylor Goldstein Equations can be found in Smyth et al. (2011), and only the equations are presented below. k is the streamwise wavenumber, l is the spanwise wavenumber, and $\sigma = \sigma_r + i\sigma_i$ is the complex growth rate. Perturbations that have $\sigma_i > 0$ are unstable modes and grow without bound, and the growth rates of these modes are of general interest in this problem. The perturbation with the largest σ_i will grow the fastest, and the wavenumber of that mode sets the length scale of the instability that we see in the system. The equations are derived by substituting $\boldsymbol{u} = (U + u', v', w')$ and $\rho = \bar{\rho} + \rho'$ into the system of equations (3.2) - (3.4). Then, substitute the wave ansatz

$$(u', v', w', p', \rho') = (\hat{u}(z), \hat{v}(z), \hat{w}(z), \hat{p}(z), \hat{\rho}(z))e^{i(kx+ly-\sigma t)}. \tag{6}$$

into the linearized system. Following this, define

$$\tilde{k} = \sqrt{k^2 + l^2}, \quad \tilde{\nabla}^2 = \frac{d^2}{dz^2} - \tilde{k}^2, \quad \tilde{U} = \frac{Uk}{\tilde{k}} \tag{7}$$

and simplify. Then we get the following system of equations which govern the growth of perturbations to the system.

$$\sigma\tilde{\nabla}^2\hat{w} = -i\tilde{k}\tilde{U}\tilde{\nabla}^2\hat{w} + i\tilde{k}\tilde{U}_{zz}\hat{w} + \nu\tilde{\nabla}^4\hat{w} - \frac{g}{\rho_0}\tilde{k}^2\hat{\rho}, \tag{8}$$

$$\sigma\hat{\rho} = -\hat{w}\bar{\rho}_z - i\tilde{k}\tilde{U}\hat{\rho} + \kappa\tilde{\nabla}^2\hat{\rho}. \tag{9}$$